NORTHWESTERN UNIVERSITY

Synthesis and Property Engineering of the 2D Oxides and Chalcogenides

A DISSERTATION

SUBMITTED TO THE GRADUATE SCHOOL

IN PARTIAL FULFILLMENT OF THE REQUIREMENTS

for the degree

DOCTOR OF PHILOSOPHY

Field of Materials Science and Engineering

By

Eve Dorthea Townsend Hanson

EVANSTON, ILLINOIS

March 2018

ABSTRACT

Synthesis and Property Engineering of the 2D Oxides and Chalcogenides

Eve Dorthea Townsend Hanson

Two-dimensional materials' "all-surface" architecture presents a new paradigm for investigations into electron confinement effects and surface phenomena. However, synthesizing, characterizing, and ultimately engineering the properties of 2D materials represents a formidable challenge. This thesis presents several cases of isolating novel 2D materials via vapor-based syntheses. Vapor-based syntheses allow for reproducible growth of monolayer and few-layer materials with electronic-grade quality. I and my colleagues focus on the group VI oxides and chalcogenides, a materials class with many synthetically-accessible layered compounds and a plethora of materials properties. Specifically, we apply an evaporative thinning technique to $Bi_2Se_{3-x}Te_x$ to produce a single monolayer. We show the rapid stoichiometry changes that can take place during evaporative thinning, to produce bismuth-rich, heteroanion compounds. For the MoO_3 system, we present a physical vapor deposition technique to produce few-layer, electronic-grade nanosheets of MoO_3.

The development of crystal doping techniques, allowing for precise electronic property engineering of Ge and Si crystals, contributed to the Nobel Prize-winning discovery of

solid-state transistors at Bell Labs. For 2D chalcogenides and oxides to be integrated into devices, taking advantage of their unique physics, similar property engineering control is required. This thesis presents several property engineering techniques to control doping levels in 2D materials. For MoO_3, we demonstrate an electron beam dose technique to precisely introduce oxygen vacancies into the MoO_{3-x} structure, thereby n-type doping the MoO_{3-x} sheet. Chapters 4-6 focus on engineering the properties of the transition metal dichalcogenides (TMDs). First, we introduce a platform chemical vapor deposition synthesis for both monolayer and heterostructure compounds. Building on this platform, we present a lithium-intercalation technique to n-type dope and engineer the on-chip monolayer phase of $MoSe_2$. However, we also show challenges with this technique, due to the instability of the intercalated structure and the resulting lack of reliability for device applications. As such, we direct the field to more fruitful paths. Based on these results, we present an alternative property engineering technique, using the charge transfer dopant $AuCl_3$ to p-type dope MoS_2. We provide structural and chemical insights into the doping process and outline a polymer pen lithography (PPL) technique to pattern the $AuCl_3$ dopant and resulting Au nanoparticles.

This thesis concludes with perspectives on future research to advance the field. Finally, the appendix focuses on broader impacts. With the decline of materials research in corporate labs such as Bell Labs, universities have a greater responsibility to understand and apply the commercialization process to materials discoveries. The appendix examines the advanced materials commercialization process with a focus on battery materials.

Acknowledgements

First, I would like to express my utmost gratitude to my advisor, Professor Vinayak P. Dravid. He has been an outstanding research mentor, pushing me to be an independently-minded scientist. I also thank him for his unwavering support of all of my varying professional interests and pursuits.

I would like to thank my committee, Professor Wolverton, Professor Huang, and Professor Kanatzidis. I am inspired by the research that you lead in your groups, and your input on my research direction and projects has been instrumental. I thank you for generously giving your time to serve on my PhD committee.

I also thank my undergraduate research advisor, Professor Robert Cava, for being an instrumental mentor, advisor, and supporter of my path into research.

I would like to thank the entire VPD group. I have greatly appreciated being a member of this talented cohort of scientists. In particular, I would like to highlight the 2D subgroup, members past and present, for serving as my frequent collaborators, colleagues, and mentors, throughout my research career at Northwestern.

I have been similarly lucky to find incredible collaborators both inside and outside the Northwestern community. Many of my most productive and enjoyable research discussions have been with collaborators from different fields. In particular, I would like to highlight Laura Lilley (Meade group), Edgar Palacios (Aydin group), Teodor Stanev (Stern group), Lintao Peng (Grayson group), Jingshan Du (Dravid and Mirkin group),

Luc Lajaunie (Arenal group), Thomas Chasapis (Kanatzidis group), and Shiqiang Hao (Wolverton group) for their contributions and intellectual insights. I also thank Samir Mayekar for his partnership in exploring commercialization topics.

Excellent research is enabled by excellent resources and staff. I greatly thank the NUANCE/EPIC/SPID/KECK/NUFAB staff for their frequent and skilled guidance and collaboration on my research projects.

I have been lucky to have incredible support throughout graduate school. I thank my parents, Camille Townsend and Ward Hanson, for their unwavering commitment to my education. I would not be here without the educational opportunities that you both made possible. I would like to thank the rest of my family and friends who have cheered me on, from near and far. Finally, I thank my husband, Dean de la Peña, for standing with me through this entire journey.

Table of Contents

List of Figures

CHAPTER 1

Introduction

"I would like to start by emphasizing the importance of surfaces. It is at a surface where many of our most interesting and useful phenomena occur. We live for example on the surface of a planet. It is at a surface where the catalysis of chemical reactions occur. It is essentially at a surface of a plant that sunlight is converted to a sugar. In electronics, most if not all active circuit elements involve non-equilibrium phenomena occurring at surfaces. Much of biology is concerned with reactions at a surface. If surfaces are so important, what do we know about them? What is a surface! What properties does a surface have that a physicist can measure?"

– Walter H. Brattain Nobel Lecture, "Surface Properties of Semiconductors", December 11, 1956 [1]

Brattain won the Nobel Prize in 1956 for his work providing the fundamental underpinnings of the transistor, p-n junction, and resulting modern electronics industry. In his Nobel lecture, he highlighted the importance of surfaces on providing key insights to make those advances possible. For this thesis, surfaces will be considered from a new vantage point: from the perspective of fundamental nanoscale architectures. Two-dimensional materials, or materials that are comprised of a single or few-layers of atomic planes, can be considered all surface. In these materials, electron confinement within the 2D plane can lead to fundamentally different quantum mechanically-driven electronic behavior.

This thesis presents several cases in isolating these "all-surface" 2D materials via new vapor-based synthetic methods. In so doing, I attempt to address Brattain's question from 60 years ago: "What properties does a surface have that a [materials scientist] can measure?" I also venture one step further: attempting to precisely engineer the properties

of these newly created 2D materials. These ventures will be described in the following chapters.

The following introduction gives a broad overview of the 2D materials field, with a particular emphasis on the 2D oxides and chalcogenides. The introduction outlines the layered materials that are conducive to 2D confinement, emergent properties under confinement, and vapor-based syntheses that currently make studying these fascinating materials possible. Finally, it outlines the current chemistry-based techniques to engineer the surface-driven properties of 2D materials. Together, these are intended to provide useful context on the state-of-the-art in the 2D field to the reader.

1.1. 2D Materials

Sections have been adapted with permission from Jeffrey Cain, Eve D. Hanson, Fengyuan Shi, and Vinayak P. Dravid, Emerging Opportunities in the Two-Dimensional Chalcogenide Systems and Architecture, Current Opinion in Solid State and Materials Science 20, 374-387, 2016.[2]

The scientific community has been captivated by the emergent physics and properties of materials under extreme dimensional confinement (0D, 1D, 2D) for the last thirty years. The discovery of graphene's extraordinary electron mobility and linear dispersion relationship by Novoselov and Geim in 2004 founded the field of two-dimensional (2D) materials.[3] The 2D field is rooted in quantum mechanics; the experimental discovery of graphene showed that for materials confined to a single atomic plane, the quantum confinement of the electron wave can fundamentally change the physics of the confined material with extraordinary results. These emergent properties under dimensional constraint can have broad advanced technological applications. Quantum dots (0D material) have found widespread adoption in electronic display technologies while carbon nanotubes

(1D material) have been adopted as a valuable composite material and are currently being heavily engineered by electronics leaders as a post-silicon material to extend Moore's law.[4] Recently, a number of companies have explored graphene as a core component of polymer composites and next-generation Li-ion battery electrode materials. Figure 1.1 shows a few of these technological successes from 0D, 1D, and 2D materials. These technological successes highlight the critical value of fundamental science to explore and characterize a full library of materials under extreme dimensional constraint. 2D materials represent the emerging frontier of these studies.

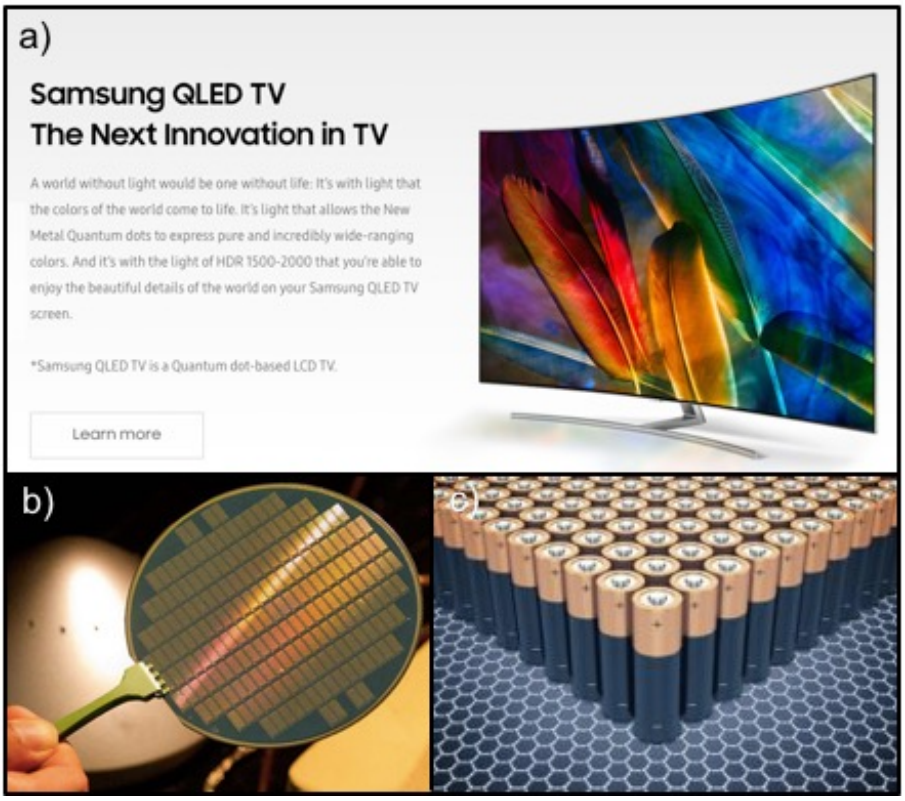

Figure 1.1. a) Samsung advertisement for quantum dot based display TV, b) image of wafer-scale carbon nanotube computer, c) schematic of graphene structure with batteries representing the growing battery market for graphene technologies. Images from [4–6].

Graphene is only one color in the broad palette of potential 2D materials. The research community has taken the mantle over the last 13 years to expand the library of 2D materials to complement and supplement graphene. Layered materials are most amenable to 2D confinement and are ubiquitous in nature. Layered structures are comprised of strong bonding within the plane with weak inter-plane or inter-layer bonding. The strong in-plane bonding stabilizes monolayer or few-layer forms of these structures, while the weak interlayer Van der Waals bonds can be cleaved or broken to isolate the 2D form. Among the known layered materials, the chalcogenides and oxides form the largest variety of layered materials conducive to 2D confinement.

1.2. The layered chalcogenides and oxides

The group VI compounds, chalcogenides and oxides, comprise an astonishing variety of physical and chemical properties. These widely divergent compounds may be categorized by their chemistry and stoichiometry (AB, AB_2, AO_x, etc.), as shown in figure 1.2.

The chalcogens of interest comprise S, Se, and Te. Across the layered chalcogenides there are common bonding trends. For a particular cation and structure motif, the bonding strength decreases with increasing chalcogen atomic number (atomic number S < Se < Te). For example, for the Mo-based TMDs, with increasing atomic number the bond length increases and there is less charge transfer from the chalcogen to the cation, leading to a less stable compound and lower melting point.[9]

The layered oxides also represent a wide variety of compounds and structure types. A few examples of these structure types include the Ruddleson-Popper, Aurivillius and

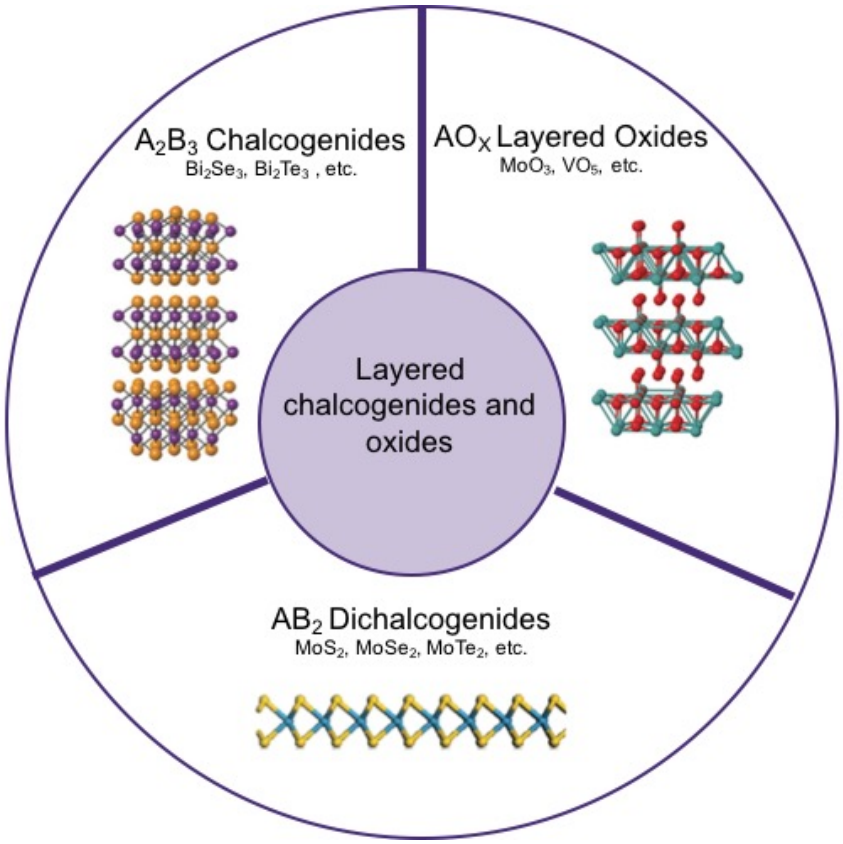

Figure 1.2. The layered chalcogenides and oxides comprise a wide variety of structure motifs.[7, 8]

Dion-Jacobson phases. However, few are amenable to vapor-phased synthesis. The current introduction will focus on the binary layered oxides, such as MoO_3 and V_2O_5.

1.2.1. A_2B_3 Group V Chalcogenides

The group V chalcogenides, with a group V element (Bi, Sb) coordinated to chalcogen atoms, tend to form a quintuple layered slab with the form B-A-B-A-B in the c-axis direction. These layered materials (e.g. Bi_2Se_3, or Sb_2Te_3) have been reported in monolayer forms. These structures tend to have small bandgaps, and due to the strong spin-splitting of the high-atomic number cation, represent a variety of interesting spin physics.[10] In

particular, these materials have experienced a lot of interest in the solid-state physics community due to their topological insulating and thermoelectric properties.[11]

1.2.2. AB_2 Transition Metal Dichalcogenides

The transition metal dichalcogenides (TMDs) represent a wide variety of compounds and properties. The compounds are comprised of a transition metal (A = Mo, W, Hf, Ta, Nb, Ti, Ta) and a chalcogen anion (B = S, Se, Te). The TMDs can form three distinct polymorphs in monolayer form, the 2H trigonal prismatic phase, the 1T octahedral phase, and the 1T' distorted octahedral phase. The three TMD phases are shown in figure 1.3. All three phases are comprised of a B-A-B stacking arrangement, with the transition metal sandwiched between the chalcogen atoms. As these monolayers are chalcogen terminated, there are possibilities of utilizing chalcogen-focused chemistry, such as thiol chemistry, to tailor their surface functionalization.

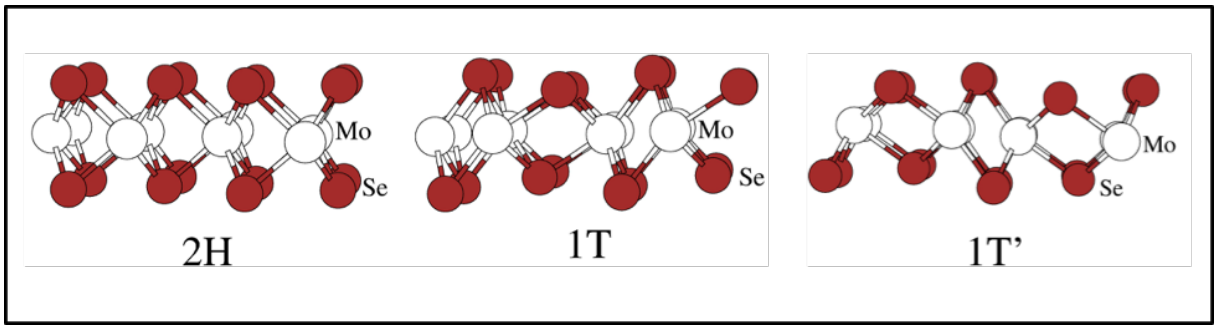

Figure 1.3. Schematic representations of $MoSe_2$ phases, with the 2H trigonal prismatic phase, 1T octahedral phase, and 1T$'$ distorted octahedral phase.

The different bonding motifs can have distinct electronic properties; for some commonly studied TMDs (MoS_2, $MoSe_2$, WS_2, WSe_2) the 2H phase corresponds to the most thermodynamically stable semiconducting phase while the 1T phase corresponds to a

metallic phase and the 1T′ phase shows a negligible band gap leading to near-metallic measured electronic properties. Phase transformation from the 2H to the 1T phase takes place via a gliding of the atomic planes.[12] The 2H semiconductor Fermi level lies between the filled d_{z^2} and empty $d_{x^2-y^2}$,d_{xy} bands while the 1T phase is metallic with the Fermi level lying in the middle of the degenerate d_{xy}, d_{yz}, d_{xz} band.[13] Doping to fill the d orbital leads to the 1T phase being stabilized. Further studies of these phase transformations are described in a later chapter for the $MoSe_2$ system.

1.2.3. AO_X Transition Metal Oxides

There are a variety of orthorhombic transition metal oxides (V_2O_5, MoO_3). These consist of a transition metal in a high oxidation state forming distinct layered units with the oxide anion. The layered transition metal oxides are susceptible to oxygen vacancy defects, leading to substoichiometry. This can be used to tailor the electronic properties of the layered material. Mono and few-layer transition metal oxides have been reported for MoO_3 and V_2O_5.[14, 15]

1.3. Emergent properties under 2D confinement

2D confinement can lead to a variety of dramatic electrical and optical property effects, as compared to the bulk counterparts. These changes in properties may be predicted by Density Functional Theory (DFT) calculations, and then are confirmed via experimental fabrication and characterization. 2D confinement leads to a widening or emergence of a band gap in many materials; this is due to standard particle in a box confinement physics, in which the energies of electronic states increase with decreasing size. As part

of these electronic structure changes, many TMDs show an indirect bandgap to direct bandgap change as a function of monolayer confinement. Figure 1.4 shows the changes in MoS_2 bandgap structure as a function of bulk to monolayer confinement. These bandgap changes may be characterized via both electrical and optical techniques. The direct band of monolayer TMDs leads to photoluminescence yields several orders of magnitude more intense than their bulk counterparts.

In 2D TMDs, first principles calculations indicate heavy effective carrier masses and van Hove singularities in the density of states just above the direct band gap, corresponding to strong interband transition peaks in the absorption spectra. Further, the monolayer TMDs often exhibit band nesting, where the conduction and valence bands lie parallel to each other. In this band nesting region in k-space, excitons spontaneously separate and relax with the same velocity towards band extrema via fast intraband transitions (hundreds of femtoseconds) and can enhance excitonic emissions.[18, 19] These band structure characteristics lead to observable changes in optical measurements such as photoluminescence and absorption spectroscopy.

Further insights into the unique optical properties of the TMDs have been investigated in the burgeoning field of valleytronics, which searches for active control of the valley degree of freedom (conduction band minima position in k space) to encode information. In most materials electrons cannot be selectively populated into a particular valley in the band structure. In contrast, monolayer TMDs have broken inversion crystal symmetry, allowing for valley selectivity. In these materials, the spin and valley numbers of valence electrons are coupled. This allows for selective population of the K and K$'$ valleys

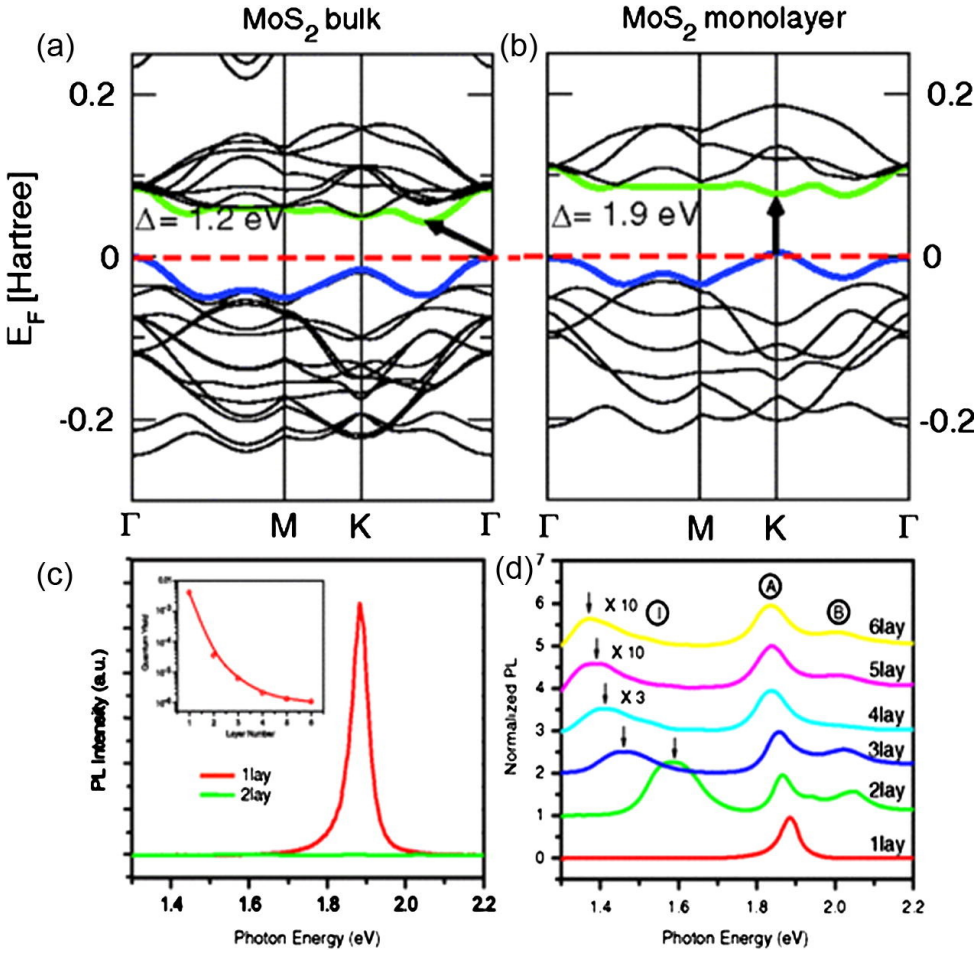

Figure 1.4. Calculated band structures of a) bulk MoS_2 (indirect band gap) and b) monolayer MoS_2 (direct band gap)[16] c) Strong PL emission from monolayer MoS_2 as compared to bilayer MoS_2. Inset: emission intensity as a function of layer number. d) Evolution of PL spectra as a function of layer number.[17] Reproduced with permission from [2].

with oppositely polarized light.[20] These unique polarization features can potentially be harnessed for new types of optical devices.

1.3.1. Electronic transport properties of the 2D chalcogenides and oxides

Rapid progress has also been made in probing and harnessing many of the 2D chalcogenides' semiconducting properties, piggybacking off the expansive graphene literature. Analogous to traditional Si-based electronics, the inherent electronic structure in conjunction with defect states determine 2D transport properties. For example, the most studied TMD, MoS_2, typically exhibits n-type transport due to sulfur vacancies incurring free valence electrons from the surrounding Mo atoms serving as electron donors.[21] Sulfur vacancies also result in Fermi level pinning near the conduction band edge, limiting contact-controlled Fermi level tuning. Various approaches have attempted to either mitigate these sulfur vacancies or use graphene contacts to more precisely control the contact Fermi level.[22] With varied contacting and gating approaches, the dominant carrier type can be switched and carrier concentration tuned.[21–23] For the W-based chalcogenides the Fermi level is pinned near the middle of the band gap, which allows for ambipolar transport and greater transport tunability. The dominant carrier type can be sensitive to growth conditions, with groups reporting n-type, p-type and ambipolar transport, all for $MoTe_2$ with the same Ti/Au contacts.[24–26] As mentioned before, the TMDs show promise for new valley and spin-based physics and device logic paradigms. Further, superconductivity has recently been reported in high-conductivity forms of the TMDs.[27–29] The groups III, IV (AX), and V (B_2X_3) chalcogenides have also received study as the active material in FETs.[30, 31] Bi_2Se_3 and Bi_2Te_3 show weak anti-localization, characteristic of exotic surface states in the few-layer regime.[32] However, The Group III and IV chalcogenides have proven to be more difficult for monolayer electrical characterization

due to oxidation and stability issues analogous to those that plague black phosphorus.[33] Encapsulation schemes could potentially mitigate these issues.

The 2D oxides have also shown promising electronic properties. Initial studies of few-layer MoO_{3-x} have shown ultra-high mobility (>1100 $cm^2\ V^{-1}\ s^{-1}$) due to high-dielectric constant Coulomb scattering suppression.[14, 34] Nanoscale MoO_{3-x} -based photodetectors have shown broadband response with high photoresponsivity.[35]

1.4. Introduction to vapor-based synthesis techniques

The ability to study the 2D chalcogenides and oxides and their emergent properties relies on the ability to produce these materials. This study was initially enabled by the micromechanical exfoliation (the scotch tape method), which while effective, is extremely low-yield.[3] Chemical exfoliation soon followed. The chemical exfoliation of single layer TMDs in fact pre-dates the emergence of the 2D materials field.[36] It was only after the discovery of graphene that care was taken to explore the emergent properties present in mono and few-layer chalcogenide materials. While chemical exfoliation has been able to produce large yield of mono to few-layer chalcogenide and oxide structures, the quality of the resultant flakes is generally poor and not electronic-grade. As a result, a variety of vapor-based techniques have been developed to produce high-quality, electronic-grade 2D chalcogenides and oxides at reasonably high yields.

Figure 1.5 compares three different vapor-based synthesis techniques, Chemical Vapor Deposition (CVD), Physical Vapor Deposition (PVD) and Evaporative Thinning (ET).

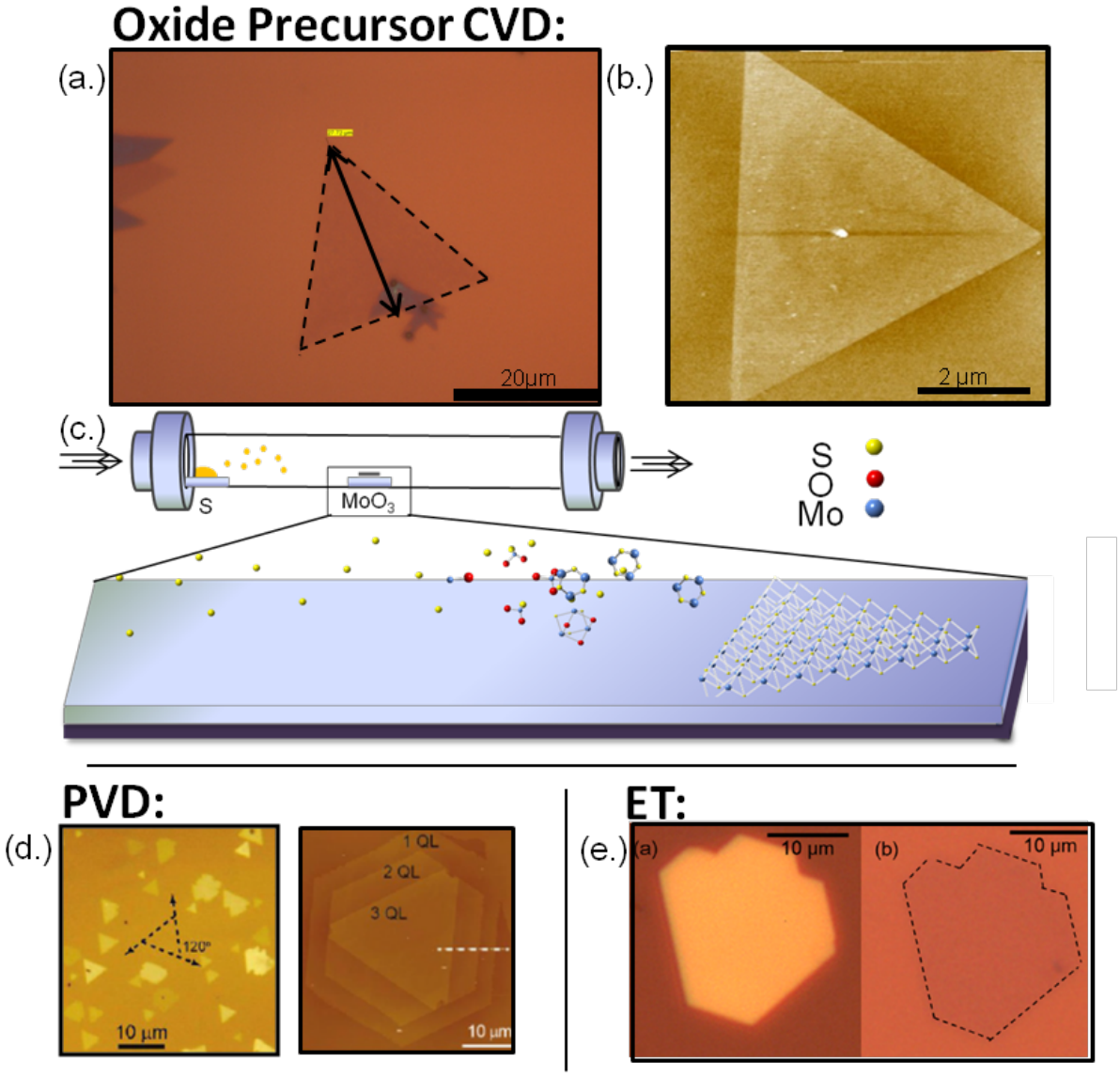

Figure 1.5. Growth methods for monolayer chalcogenides. a) Optical (Cain, Dravid) and b) AFM images of CVD grown monolayer MoS_2 c) Schematic of oxide precursor growth of MoS_2. d) Grown Bi_2Se_3 nanoplates on graphene[37] e) Bi_2Se_3 monolayers made via evaporative thinning.[38] Reproduced with permission from [2].

1.4.1. Physical vapor deposition

Physical vapor deposition is a technique by which a target compound is evaporated, carried by an inert carrier gas, and deposited downstream to form a variety of mono or few-layer samples. Figure 1.5d shows example physical vapor deposition products, specifically of Bi_2Se_3 quintuple layers on graphene.[37] Physical vapor deposition typically produces single crystal materials suitable for electronic characterization, and has been particularly successful for chalcogenides difficult to access via other synthesis techniques, such as the groups IV and V chalcogenides.[39–42] PVD growths for 2D materials have generally been catalyst-free, meaning the growths are more dependent on the exact experimental conditions and deposition substrate than for catalyst-based nanomaterials growths (such as carbon nanotube growths).[43] Some drawbacks to PVD are that it produces a distribution of nanomaterial thicknesses, commonly on the order of monolayer-tens of nanometers thick. As such, the yield of monolayer materials tends to be lower than for CVD-based growths. The lateral extent is also limited and tends to be on the order of 10-30 μm.

1.4.2. Chemical vapor deposition

Chemical vapor deposition (CVD) is a commonly used synthesis technique that involves powder-based precursors that are heated to react in the vapor phase, and are carried by an inert carrier gas to deposit on the target substrate. Metal oxide precursor-based CVD has been used to form monolayer, relatively large-area (100s of μm) growth across the semiconductor Mo and W-based transition metal dichalcogenides. The typical synthesis is as follows: a metal oxide precursor (e.g. MoO_3, WO_3) is placed in the high-temperature region inside a tube furnace while the chalcogen of interest (S, Se) is placed upstream

in a lower temperature zone. An inert gas, N_2 or Ar, is flowed through to create an inert atmosphere and to act as a carrier gas. By carefully controlling the furnace time-temperature profile, the reaction can be engineered so that the chalcogen and transition-metal oxide are present in the vapor phase at the same time, and can react to form the TMD of interest and deposit downstream on a target substrate. Figure 1.5c shows a schematic of this CVD growth process. For the sulfur-based TMDs the sulfur is a strong enough reductant to directly reduce the transition metal oxide. For the Se-based TMDs, H_2 can also be flowed through with the carrier gas to serve as an additional reducing agent. Target substrates have included SiO_2/Si substrates (to enable direct back-gated device fabrication), sapphire, and mica.[44–46] CVD growths can occur both at low pressure similar to PVD (LPCVD) or at atmospheric pressure (APCVD). Figure 1.5a shows an optical image of a monolayer MoS_2 material fabricated via CVD while figure 1.5b shows the resultant AFM height image, confirming the monolayer thickness of the resultant MoS_2.

The ease of the metal oxide based CVD TMD synthesis has largely democratized the growth and characterization of the monolayer materials, greatly increasing the interest and accessibility of these materials. That has enabled an explosion in characterization, understanding and engineering of this particular class of 2D materials. This helps highlight the importance of developing robust, high-quality syntheses to enable the next generation of 2D materials research.

1.4.3. Metal organic chemical vapor deposition

Metal organic chemical vapor deposition (MOCVD) is a related technique that uses purely gas-phase reactants to react in the vapor phase and deposit on a target substrate. The reaction's characteristics can be tailored based on the partial pressures of the input gas reactants (e.g. $Mo(CO)_6$, $W(CO)_6$, $(C_2H_5)_2S$ and H_2). Recent reports have shown success using MOCVD to produce wafer-scale TMDs with high crystal quality.[47] This technique requires a large dedicated reactor set-up, with has limited its adoption.

1.4.4. Evaporative thinning

Beyond PVD and CVD, other vapor-based techniques have been developed. One such technique, evaporative thinning, combines PVD with a top-down method and has been successful in producing monolayer samples of the A_2B_3 binary and ternary alloys. In this technique, the chalcogenide or oxide is deposited downstream to ~1 μm thicknesses. The sample is then annealed under vacuum to remove excess material down to a single monolayer thickness. 2D sheets are produced of materials otherwise inaccessible to vapor-based techniques, and with high crystalline quality.[38] Further, preferential evaporative thinning may be used to control the stoichiometry of the target 2D material.[48] Figure 1.5 shows a sample before and after evaporative thinning; the optical image shows that the monolayer material retains the same shape as the original flake and shows the contrast of a monolayer thickness.

1.4.5. Comparison of vapor-based 2D synthesis techniques

The various vapor-based syntheses have benefits and drawbacks across the 2D chalcogenide and oxide materials. A table is included below that compares the current state-of-the-art in the vapor-based syntheses.

Technique	**Materials**	**Precursors**	**Flake Size**	**Thickness**	**Crystal Quality**
CVD	MoS_2, WS_2, $MoSe_2$, WSe_2	Metal oxide	> 100 μm	1 ML	Moderate
PVD	TMD, AB, A_2B_3	material of interest	1-30 μm	1 ML to to> 10 nm	High
ET	TMD, AB, A_2B_3	material of interest	>10 μm	1-2 nm	Moderate
Metal organic CVD	MoS_2, WS_2	$Mo(CO)_6$, $W(CO)_6$, $(C_2H_5)_2S$	Wafer scale	1 ML	High

Across the materials described in this thesis, evaporative thinning was the technique of choice for the A_2B_3 group V chalcogenides, PVD was utilized for the MoO_3 synthesis while CVD was employed for the TMD work.

1.5. Introduction to chemistry-based property engineering techniques

While the 2D chalcogenides and oxides present a broad library of materials, to fully take advantage of their properties additional levels of control are required. Technological applications require the ability to rationally tune the optoelectronic properties of the

target material. A number of approaches have been developed to engineer and tailor the optical, physical, and electronic properties of 2D chalcogenides and oxides. These techniques utilize a variety of chemistries to tailor the 2D sheets at will. This gives access to a broader array of potential physics, devices, and applications.

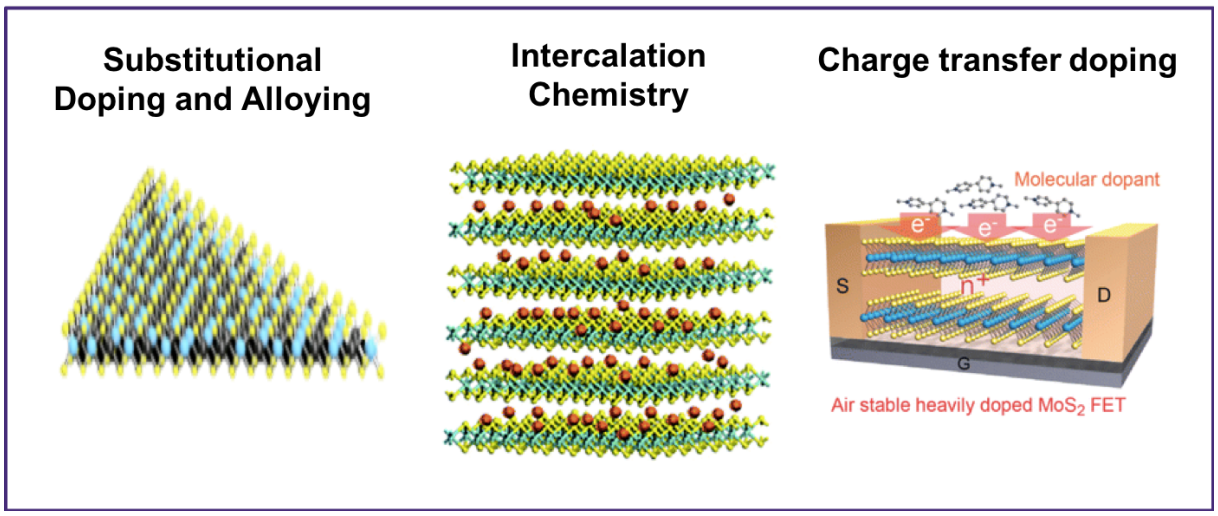

Figure 1.6. A variety of techniques can be used to engineer the 2D chalcogenides, such as substitutional doping, intercalation chemistry and charge transfer doping. Images are from [49–51]

1.5.1. Substitutional Doping and Alloying

The 2D chalcogenides and oxides have been engineered via doping and alloying approaches. For the TMDs, both mixed cation and mixed anion compounds have been demonstrated via CVD synthesis alloying techniques. By incorporating multiple precursors in the CVD process, ternary compounds can be produced.[52, 53] These ternary alloys show PL emission properties characteristic of their intermediate composition and can be precisely tuned with stoichiometry from one compound's properties to the others. For example, the bandgap can be precisely turned from the MoS_2 1.85 eV to the $MoSe_2$

1.55 eV with the MoS_xSe_{2-x} ternary system.[52] Intermediate compounds have also been shown for the group V chalcogenides with improved anti-localization behavior compared to the end compounds.[54] However, given the similarities in electronic structure between sibling TMDs (heteroanion or heterocation), it is rare to change majority carrier type via alloying techniques.

Some limited success has been reported via substitutional doping techniques. There have been a few reports of Nb doping of the TMDs, showing a majority n-type to p-type carrier type change, but generally via chemical-vapor-transport methods (as opposed to direct CVD doping).[55] Other reports have included small amounts of manganese doping in MoS_2, with limited transport effects.[56] In general, the level of substitutional dopant incorporation is difficult to control via direct CVD growth, giving limited precision over the level of doping and exact carrier concentration.

1.5.2. Ion intercalation doping techniques

Ion intercalation has been used to significantly alter the electronic properties of the 2D host. Lithium intercalation has been used extensively in the 2D TMDs as a chemical exfoliation technique to separate the layers to create monolayer TMDs.[57] Lithium intercalation in the TMDs donates electrons, stabilizing the degenerate d_{xy}, d_{yz}, d_{xz} orbitals, leading to a 1T, then 1T' transformation and metallic-like transport.[13] Similar results can be achieved via Na^+ intercalation into the 2D chalcogenides lattice.[58] These intercalation chemistries are broadly studied by the electrochemical storage community for

potential battery applications. Recent work has focused on using Li intercalation to engineer the TMD phase and directly modify the electronic properties.[59–61] This approach is explored for the $MoSe_2$ system in chapter 5.

Among the layered oxides, H^+ ion intercalation has been used to introduce n-type doping and substoichiometry into few-layer MoO_3. The intercalated few-layer MoO_3 has shown broadband photodetector performance and plasmonic resonances in the visible regime.[14, 62]

1.5.3. Charge transfer doping techniques

A variety of electron donating or accepting species have been utilized to alter the doping levels of the 2D chalcogenides. This can range from Lewis acid-Lewis base chemistry (involving a covalent bond formation) to reduction-oxidation reactions that interact via surface charge transfer.

1.5.3.1. Lewis acid-Lewis base chemistry. Lewis acid-Lewis base chemistry takes advantage of the surface chalcogen to use the chalcogen as a Lewis base to pair with an external electron acceptor, or Lewis acid. This has been reported to incur a majority n-type to p-type transition in 2D InSe, as well as a slight p-type doping in MoS_2 and WS_2.[63] However, attempts at experimental reproduction of these results in our lab suggested that the Lewis acid treatments can cause damage to the underlying monolayer, limiting the effectiveness of this approach.

Other approaches have taken advantage of the terminating chalcogen to utilize well-developed thiol chemistry to functionalize the TMD and alter its electronic properties. For example, Chou et al. directly control the 1T' to 2H transition of chemically-exfoliated

MoS_2 and WS_2 via ligand conjugation.[64] This thiol chemistry can also be used to create biologically-active sensors.[65, 66]

1.5.3.2. Reduction-oxidation charge transfer doping. Utilizing reduction-oxidation charge transfer doping to achieve controllable doping of the TMDs has recently emerged as a promising approach to engineering 2D chalcogenide properties.[67] As 2D materials are all surface, they are particularly susceptible to surface charge transfer techniques. Surface doping techniques also generally have mild temperatures and experimental conditions, with the potential for high tunability and spatial selectivity. A prototypical system is the strong oxidation agent $AuCl_3$. $AuCl_3$ is a strong oxidizing agent, and has previously been shown to act as an electron acceptor on both carbon nanotubes and graphene.[68–70] Preliminary reports have shown that $AuCl_3$ can be used to achieve majority p-type doping in the MoS_2 system, and can be exposed to create p-n junctions with enhanced rectification behavior and precisely tunable doping levels.[71–73] I further extend this doping approach to MoS_2 monolayers in chapter 6.

Other charge transfer dopants have been reported to controllably n and p-type dope the TMDs to small degrees (not changing majority carrier type). For example, Matsuda et al. report using Tetrafluorotetracyanoquinodimethane (F_4–TCNQ) as a p-type dopant to incur small changes in the MoS_2 photoluminescence spectra.[74] They also report using nicotinamide adenine dinucleotide (NADH) as an n-type dopant, with resulting shifts in the photoluminescence spectra.[74] Vogel et al. report a variety of organic electron donors and acceptors that give measurable shifts in the MoS_2 transport properties.[75] Benzyl viologen has been used as an effective n-type surface charge transfer donor, leading to degenerate n-type doping in MoS_2 and reduced contact resistance.[51] Charge transfer

dopants (F4-TCNQ, MoO_3, MnPc) have also been applied to the A_2B_3 chalcogenides in order to engineer their topological surface state properties.[76–78] Across doping techniques, the challenge is modifying the monolayer electronic structure without damaging the fragile monolayer structure.

1.5.4. Introduction to future chapters

Based on these foundations, there are a number of key questions that emerge. The first theme of inquiry is synthesis: are there new materials that we can bring into the library of 2D materials via vapor-phase synthesis techniques? This question will be addressed both in Chapter 2, applying evaporative thinning to fabricate new 2D bismuth-rich ternary compounds, as well as in Chapter 3 applying physical vapor deposition to synthesis few-layer sheets of the high-k dielectric MoO_3.

The next thematic question is how can we better engineer the properties of 2D chalcogenides and oxides? In chapter 3, we describe explorations in the 2D MoO_{3-x} system and show exquisite tunability from the insulating MoO_3 state to the semiconducting MoO_{3-x} state as a function of oxygen stoichiometry. Chapters 4-6 explore ways to introduce n-type and p-type electronic tunability into the rapidly emerging class of TMDs and point the way to local optoelectronic property control.

CHAPTER 2

2D Bi-rich nanosheets via evaporative thinning of Se-doped Bi_2Te_3

Adapted with permission from Eve D. Hanson, Fengyuan Shi, Thomas C. Chasapis, Mercouri G. Kanatzidis, and Vinayak P. Dravid, Two-dimensional bismuth-rich nanosheets through the evaporative thinning of Se-doped Bi_2Te_3, Journal of Crystal Growth 436, 138-144, 2016.[48]

2.1. Introduction and Motivation

Doping strategies have long relied on solid solutions for precise control of properties. Intermediate solid solution compositions may have enhanced electronic properties that are inaccessible from the constituent materials. We explored these strategies within the Bi-Te-Se solid solution system, aiming to create intermediate compositions with balanced electron and hole concentrations to form a bulk insulator. Instead, we found a novel preferential evaporative thinning mechanism that produces bismuth-rich nanosheets that potentially have rich transport phenomena.

Bismuth selenide (Bi_2Se_3) and bismuth telluride (Bi_2Te_3) have been studied for decades for their thermoelectric properties. They have received a recent renewal in scientific attention as they were some of the first 3D topological insulators to be theoretically predicted and experimentally realized.[79, 80] Topological insulators can be described as a novel form of matter: they are insulators in the bulk with metallic surface states that are topologically protected against scattering by time-reversal symmetry.[81] However, both

Bi_2Se_3 and Bi_2Te_3 have intrinsic high bulk carrier densities, obscuring the metallic surface state conduction and stymying efforts to properly study the surface transport properties. These high carrier densities are due to the small formation energy of native defects.[82] Appropriate alloying of Bi_2Se_3 and Bi_2Te_3 to form intermediate compositions can result in bulk insulating behavior, leading to more measurable topological surface states.[83]

Additionally, nanostructuring reduces sample size and increases the surface-to-volume ratio, which can also enable more readily measurable surface states. Nanostructuring has been shown to enhance both the thermoelectric performance and show more readily measurably topologically-protected surface states in Bi_2Se_3 and Bi_2Te_3 and some intermediates.[54, 84–86] However, current methods for producing Bi_2Se_3-Bi_2Te_3 compound nanosheets suffer from either very low growth rates or poor quality.[87–89] Our lab developed an evaporative thinning technique that produces high-quality and large-area monolayer Bi_2Se_3 and Sb_2Te_3 sheets.[38] This evaporative thinning approach has been extended to a ternary system for the first time, which due to vapor pressure differences of the constituent elements lead to a final bismuth-rich phase. The observed compositional shifts are well explained through a thermodynamic vapor pressure driven mechanism.

The large interest in this class of 2D materials strongly demands the understanding of the underlying mechanisms dictating the final composition and thus the final properties. Therefore, our in-depth structural and compositional analyses of a phase never before reported in 2D form serves as a case study in the field of nanoscale compounds synthesized via vapor pressure or CVD means. With their predominantly bismuth character, the final nanosheets could be further explored for exotic electronic properties.[90, 91]

2.2. Results and Discussion

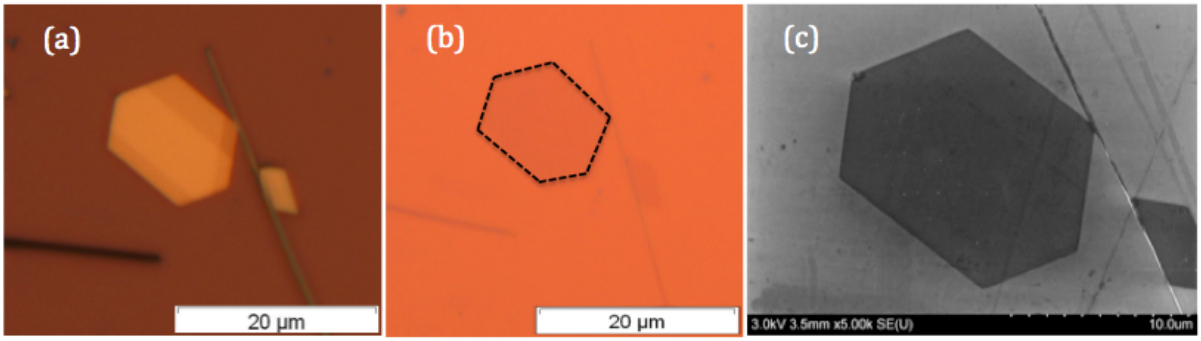

Figure 2.1. a) Optical image of $Bi_2Te_{2.9}Se_{0.1}$ sheet before thinning, b) Optical image of the same sheet after evaporative thinning with reduced contrast due to nm-scale thickness, c) SEM image of Bi-rich nanosheet after evaporative thinning. Reproduced with permission from [48].

Evaporative thinning comprises two steps: first, a catalyst-free physical vapor deposition that deposits micron-thick flakes, and second, an annealing step that evaporatively thins off material, leaving behind a single or bilayer 2D nanosheet. Evaporative thinning of the deposited flakes produces high-quality, ultra-thin nanosheets of the ternary compound. Figure 2.1 contains low magnification optical images of one such sheet pre (a) and post (b) evaporative thinning on a 300 nm SiO_2/Si substrate. The contrast between the nanosheet and the substrate decreases as the sheet height is reduced to nanometer scale. Figure 2.1c shows an SEM image of the same sheet. Both the optical and SEM images show that the sheet has retained its lateral dimensions, without any lateral shrinking during the evaporative thinning. Figure 2.2 is comprised of the corresponding AFM image and profile of the thinned nanosheet. The AFM image and profile show that the nanosheet is 1.2 nm in thickness with slight variation. Both the AFM and SEM images indicate that the wide-area (15 micron) sheets are smooth and continuous, without holes

or tears. However, the key question is how the composition of these large area nanosheets compares to their deposited, thick counterparts.

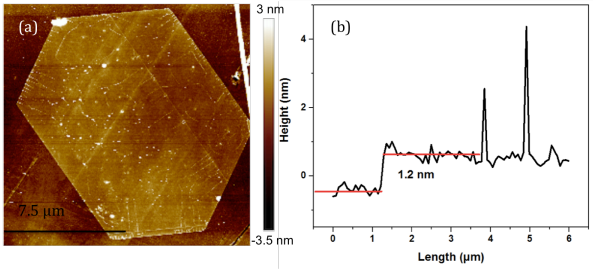

Figure 2.2. a) AFM image of thinned Bi-rich nanosheet, b) AFM height profile after thinning.Reproduced with permission from [48].

To probe this question, scanning transmission electron microscopy energy-dispersive x-ray spectroscopy (STEM EDS) maps were taken on $Bi_2Te_{2.9}Se_{0.1}$ nominal composition flakes before and after evaporative thinning. Figure 2.3 shows the STEM high-angle annular dark-field (HAADF) image, as well as EDS mapping of the Bi L edge, Te K edge, and Se K edge of $Bi_2Te_{2.9}Se_{0.1}$ after initial deposition, in their thick, bulk-like state. Bi, Te, and Se signals are all consistent throughout the flake, suggesting homogeneous distribution of the elements without phase segregation. The EDS spectrum extracted from the mapping shows Bi, Te and Se peaks, and quantification from the spectrum shows stoichiometry close to the nominal composition as shown in Figure 2.5. The edges for quantification were chosen based on carefully calibrated k-factors of Bi_2Se_3 and Bi_2Te_3. These results show that after the initial deposition, the chemical composition aligns between the nominal and experimentally determined stoichiometries.

Similar STEM EDS maps were taken from the same flakes after evaporative thinning. In order to examine the flake composition's evolution, a partially thinned flake was obtained by carefully controlling the time and temperature. Figure 2.4a shows the STEM

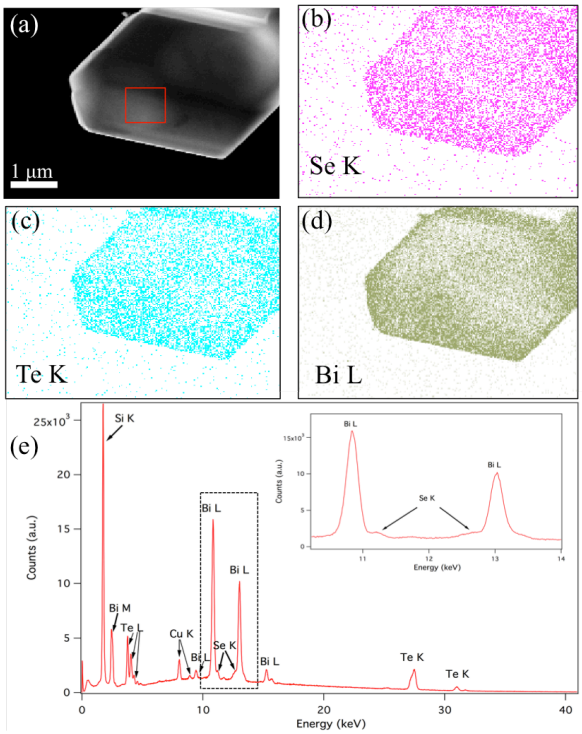

Figure 2.3. STEM EDS mapping of $Bi_2Te_{2.9}Se_{0.1}$ flake before thinning. a) HAADF image of the flake. b) to d) are the mappings of Se K, Te K and Bi L edges, respectively. e) is a spectrum from the area indicated by the red square box in a). The Cu peaks arise from the brass sample holder. The inset of e) is a zoomed-in spectrum of the Bi L and Se K edges. Reproduced with permission from [48].

secondary electron image of the thinned flake, while Figure 2.4b-d shows the STEM EDS mapping of the thinned flake. The thick part of the flake continues to show consistent mixing of the three elements as shown in Figure 2.4b-d. Due to the ultra-thin nature of the thinned region, the EDS mapping does not show obvious Bi, Te, or Se signal. However, with longer collection times the EDS spectra from the thin region have better signal to noise ratios. The EDS spectrum in Figure 2.4e from the thinned region shows all elements are present. Quantification from these EDS spectra shows that the evaporative thinning corresponds to significant changes in stoichiometry in the ternary compound, as

indicated in Figure 2.5. Figure 2.5 includes a table of the ratios of the highest-intensity relevant x-ray peaks, and the corresponding estimated atomic percentage quantifications. The thinned flake is now predominately bismuth, as calculated from the STEM-EDS spectra. Further, the atomic percentage ratio of Se/Te has increased by more than 10x. This methodology was employed across many samples with similar Bi-rich nanosheet outcomes.

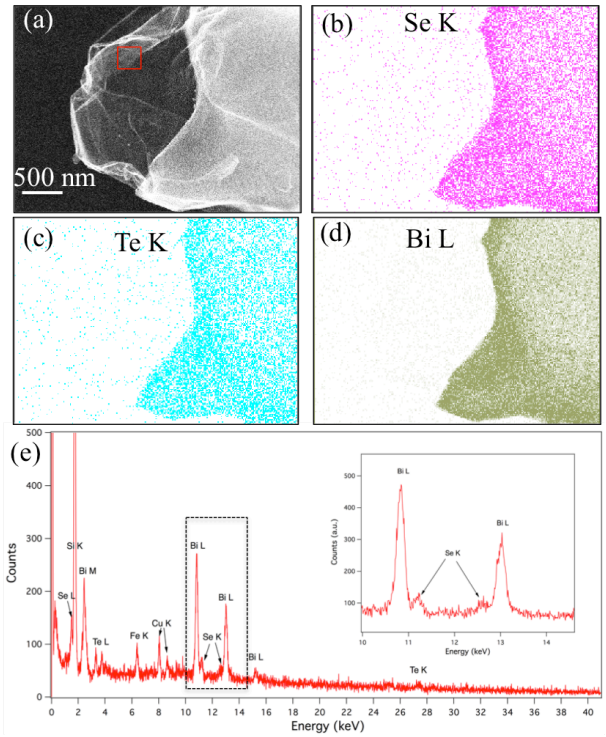

Figure 2.4. STEM EDS mapping of $Bi_2Te_{2.9}Se_{0.1}$ flake after thinning. a) Secondary electron image of the partially thinned flake. b) to d) are the mappings of Se K, Te K and Bi L edges, respectively. e) is a summed spectrum from the area indicated by the red square box in a). The Cu and Fe peaks arise from the sample holder and microscope column respectively. The inset of e) is a zoomed-in view to show Bi L and Se K edges. Reproduced with permission from [48].

As a further source of composition information, we characterized the compounds both before and after evaporative thinning with time-of-flight secondary ion mass spectrometry

(ToF-SIMS). Figure 2.9(a) shows SIMS profiles of a representative sheet before thinning. Given their respective electronegativities, a positive ion mode was used to measure the Bi ion signal, and negative ion mode to measure the Te and Se ion signal. Reference Bi_2Se_3 and Bi_2Te_3 compounds were used to determine the appropriate SIMS conditions and to determine the most appropriate isotopes to compare. The reference samples suggest that the Bi^{209} isotope, the Te^{128} isotope, and both the Se^{78} and Se^{80} isotopes have the most reliable signal intensities. The SIMS profiles confirm that Bi, Te, and Se are present in the composition on the surface of the deposited, thick $Bi_2Te_{2.9}Se_{0.1}$ sheet before thinning. After evaporative thinning, based on the SIMS spectra of the post-thinned flake in figure 2.9b, Bi, Te, and Se are all present. After the Ga^+ sputtering to clean the surface, no appreciable amounts of oxidized species (SeO^-, TeO^-) were detected. While quantitative SIMS analysis can be quite complex, the qualitative trends of the relative intensity ion ratios in the SIMS profiles parallel the EDS profiles for the chalcogenides. Before thinning, there is more Te present in the sample than Se. After thinning, the Te intensity has dropped precipitously while the Se intensity has remained relatively stable. Both EDS and SIMS indicate that the post-thinned nanosheet is bismuth rich.

	Bi L/ Te K	Bi L/ Se K	Te K / Se K	Bi L Atomic % (error)	Te K Atomic % (error)	Se K Atomic % (error)
Thick Sheet	7.8	20.2	2.6	44.9 (.34)	52.4 (1.8)	2.6 (.21)
Thin Nano-sheet	21.8	9.7	0.3	65.8 (2.9)	23.2 (17.9)	11.0 (1.7)

Figure 2.5. Table comparison of EDS peak ratios and resulting EDS-derived chemical compositions pre and post evaporative thinning. Reproduced with permission from [48].

The evaporative thinning synthesis provides a facile way to make a nanosheet Bi-rich ternary compound not previously synthesized in 2D. Based on both compositional techniques, evaporative thinning preferentially removes Te and Se from the structure. This can be understood via a thermodynamic vapor pressure mechanism. In the vapor phase both Bi_2Se_3 and Bi_2Te_3 disassociate into their constituent ions Bi^{3+} and Se^{2-}/Te^{2-}.[92] Based on mass effusion experiments, these ions form species that sublime at different rates as follows: $p(Te_2) > p(BiTe) >> p(Bi_2), p(Se_2) > p(BiSe) > p(Bi_2)$. Of these species Te_2 is the most volatile, corresponding to Bi_2Te_3 being a more volatile compound than Bi_2Se_3. The proposed vapor pressure-driven mechanism describes both the physical vapor deposition and evaporative thinning steps. In both sublimation events the bismuth and chalcogen ions dissociate. During the PVD process the flakes have a chance to deposit on substrates downstream. There are enough nucleation events and energy for re-association into the most thermodynamically preferred stoichiometry during flake formation on the silicon substrate. In the evaporative thinning step material is only sublimed and removed to reach the final nanosheet form. As a result, the vapor pressure differences of the constituent ions dominate so that Te, and to a lesser degree Se, are driven from the structure. Thus, the final 2D nanosheet is Bi-rich. Figure 2.6a shows this preferential evaporative thinning process taking place. More Te leaves the structure than the other elements, and more Se leaves the structure than Bi. As the Bi sheets inside the crystal structure retain their hexagonal symmetry, the final crystal structure of the 2D Bi-rich nanosheet is hexagonal as highlighted by the TEM diffraction pattern in Figure 2.6b. The lattice parameter of the 2D Bi-rich nanosheet is calculated to be 4.44 A from the diffraction pattern, which lines up well with the reported lattice parameters for similar bulk Bi-rich

compounds.[93–95] Bulk Bi-rich compounds (Bi_7Se_3 and Bi_7Te_3) have been found to incorporate additional Bi-Bi slabs between the quintuple layers.[93, 95] The evaporatively thinned nanosheets structure is likely related to these bulk Bi-rich structures, with both Se and Te atoms incorporated in the chalcogen atomic positions.

This mechanism highlights that altered sublimation conditions can cause large changes in nanoscale stoichiometry even while the symmetry remains the same. For nanoscale composites, the interactions within heterogeneous systems can similarly impact the materials' stoichiometry and doping. Careful analysis of carrier type and composition can be critical to understanding the underlying mechanisms and properties of the system.

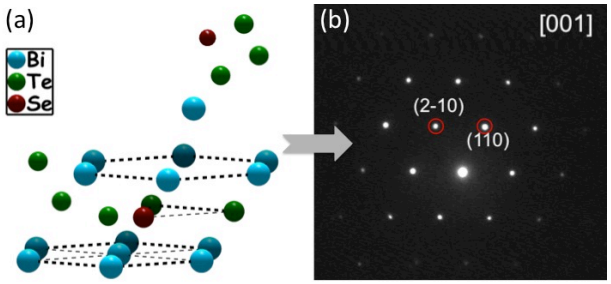

Figure 2.6. a) Schematic of evaporative thinning process within a single unit cell. Chalcogens are preferentially driven from the structure, leaving behind a predominantly bismuth sheet. The dotted lines highlight hexagonal symmetry within the structure. The evaporative thinning process leads to a final hexagonal symmetry, shown in a), the diffraction pattern of a Bi-rich nanosheet along the [001] orientation. Reproduced with permission from [48].

In conclusion, a new 2D Bi-rich composition in the ternary Bi-Te-Se system has been fabricated via an evaporative thinning technique. Utilizing both STEM-EDS and SIMS, we have been able to determine the compositional shift from $Bi_2Te_{2.9}Se_{0.1}$ to a Bi-rich nanosheet as a result of chalcogen ions being preferentially driven out of the structure due to vapor pressure differences. The resultant structure shows single-crystal hexagonal

symmetry, with a lattice parameter aligning with a Bi-rich phase. Based on analogous bulk Bi-rich Selenide and Telluride structures, the 2D Bi-rich nanosheet structure likely includes a Q(1)-Bi-Q(2)-Bi-Q(1) quintuple layer slab with bismuth bilayers to accommodate the additional bismuth atoms. With their predominantly bismuth character and Chalcogen doping, these nanosheets should be further explored to probe their unique electronic properties. Further, the mechanism of Bi-rich nanosheet formation highlights that moderate temperature and pressure changes can cause large shifts in stoichiometry of these compounds. Within the Bi-Te-Se systems even small changes in composition can incur native defect formation, changing both carrier concentrations and majority carrier type. As such, detailed compositional analysis is vital to correctly probe the topological insulating and thermoelectric performance of similar compounds. These lessons and detailed characterization techniques are applied in the following chapters.

2.3. Methods and Supporting Information

2.3.1. Methods

Bulk crystals growth methods were the same as in the previous report on evaporative thinning, with a growth temperature of 850 C for both Bi_2Se_3 and Bi_2Te_3.[38] Following the synthesis of bulk Bi_2Se_3 and Bi_2Te_3, the crystals were crushed into powder with a mortar and pestle. The appropriate ratio of Bi_2Se_3 powder and Bi_2Te_3 powder were intimately mixed to reach the $Bi_2Te_{2.9}Se_{0.1}$ nominal composition.

Figure 2.8's schematic illustrates both steps of the evaporative thinning process. Sheets with $Bi_2Te_{2.9}Se_{0.1}$ nominal stoichiometry were deposited using a catalyst-free physical vapor deposition method. The source powder was placed in the center of the

hot zone of a 12 in. Lindberg Blue tube furnace within a 1 in. silica tube. Si substrates with a 300 nm SiO_2 layer were placed downstream in a colder zone within the furnace (approx. 3 cm from source material), suspended on alumina boats. The chamber pressure was maintained at approximately 20 Torr with an ultra-high purity Ar flowing in at 25 sccm. The furnace was heated to 490 C over the course of 15 min and held at that temperature for 25 min before quenching by opening up the furnace.

After the initial deposition of $Bi_2Te_{2.9}Se_{0.1}$, the substrates covered with crystalline plates were positioned in the hot center of the tube furnace and held at 450 C for 15 min for evaporative thinning. The furnace was opened after the prescribed time in order to quench the samples. Similar to the deposition step, the chamber was held at 20 Torr with 20 sccm of flowing Ar during evaporative thinning.

STEM EDS measurements were taken using a Hitachi HD-2300 Dual EDS STEM to determine pre-thinning stoichiometry. The beam size for STEM imaging and STEM EDS is 0.4 nm with probe current 700 pA using 200 kV. Thirty frames and 10s acquisition time for each spectrum were used to obtain the STEM EDS mapping with good quality. Quantification was calculated with the Cliff-Lorimer with absorbance algorithm, and the atomic percent error represents +/- one standard deviation. TEM was carried out using JEOL 2100F microscope operating at 200 kV. For S/TEM sample preparation, $Bi_2Te_{2.9}Se_{0.1}$ plates were first deposited onto single crystal NaCl substrates using the same growth conditions described above. The NaCl substrates were then dissolved in a small amount of deionized water, and the flakes were scooped out using a TEM grid with 5 nm Si_3N_4 window. The grid was then air-dried on filter paper in a sealed container. A graphite cap was used to reduce interfering signal from the cap. The TEM samples were

then subjected to the same thinning conditions as the samples on 300 SiO_2/Si substrates, and similar EDS measurements were taken.

ToF-SIMS was also deployed for 2D compositional analysis. SIMS consists of mass spectroscopy of secondary ionized particles that are emitted from a sample after being bombarded with energetic primary particles.[96] These ionized secondary particles can be both elemental ions and ionized clusters. By analyzing the time of flight, ToF-SIMS can distinguish between different mass complexes in the sample. Static SIMS uses a low current density primary ion beam in order to maintain monolayer surface integrity for long analysis periods (into several hours).[97] SIMS measurements were taken on a PHI TRIFT III ToF-SIMS with a gallium ion gun. Static SIMS conditions were used to prevent damage to the sample. The primary ion beam was kept below 10^{13} ions/cm^2. Under these low dose conditions, the surface atomic layer is kept intact for several hours. Ga^+ ions were sputtered over a 100 um area for 10 seconds to remove surface contamination without destroying the underlying sample.

2.3.2. Supporting Figures

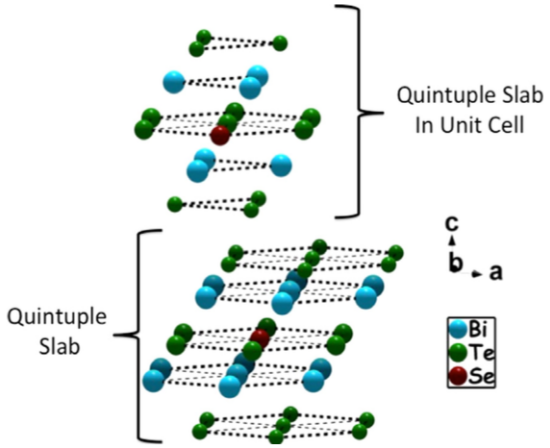

Figure 2.7. Schematic drawing of the $Bi_2Te_{3-x}Se_x$ layered structure, which has the same symmetry as Bi_2Se_3 and Bi_2Te_3. The dotted lines highlight the symmetry of the structure and do not represent bonds. The top quintuple slab shows the atomic positions within a single unit cell, while the bottom quintuple slab has been expanded to highlight the hexagonal symmetry of each atomic layer.Reproduced with permission from [48].

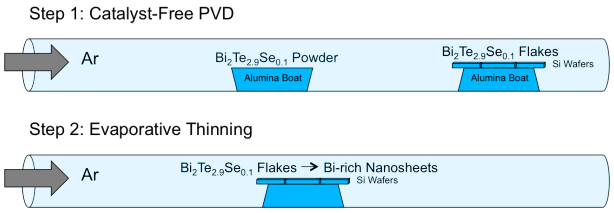

Figure 2.8. Schematic of the catalyst-free physical vapor deposition and evaporative thinning processes to fabricate Bi-rich nanosheets. Reproduced with permission from [48].

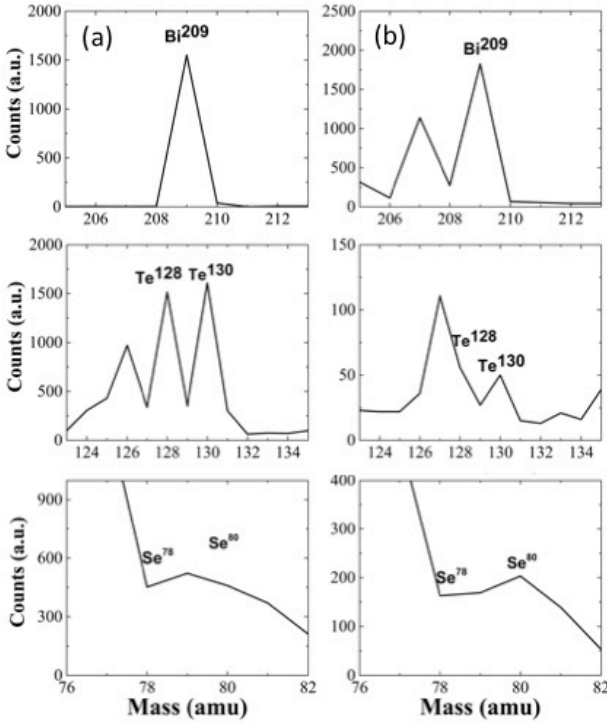

Figure 2.9. a) Representative deposited $Bi_2Te_{2.9}Se_{0.1}$ thick sheet SIMS spectra, b) Representative spectra from a collection of post-thinned Bi-rich nanosheets. Spectra are of the most common Bi, Te, and Se mass isotopes. Reproduced with permission from [48].

CHAPTER 3

Synthesis and electronic property control of 2D MoO_3

Adapted with permission from Eve D. Hanson, Luc Lajaunie, Shiqiang Hao, Benjamin D. Myers, Fengyuan Shi, Akshay A. Murthy, Chris Wolverton, Raul Arenal, Vinayak P. Dravid, Systematic study of oxygen vacancy tunable transport properties of few-layer MoO_{3-x} enabled by vapor-based synthesis, Advanced Functional Materials 27, 1616-3028, 2017.[98]

In chapter 3 we utilize a different vapor-phase synthesis technique, physical vapor deposition, to study the molybdenum trioxide system in 2D form. We also present a detailed structure-property relationship between oxygen substoichiometry (MoO_{3-x}) and correlated electronic transport.

3.1. Introduction and Motivation

Molybdenum trioxide (MoO_3), a layered transition metal oxide, has shown widespread and increasing technological applicability due to its numerous attractive functional properties. Bulk MoO_3 in stoichiometric form is a high-k dielectric ($k > 500$) insulator.[99] Further, the electronic structure of MoO_3 can be tailored by modifying the oxygen sub-stoichiometry (MoO_{3-x}). Oxygen sub-stoichiometry introduces electronic gap states and increased electrical conductivity.[100, 101] These bulk tunable transport properties have shown applicability across a number of technological regimes, including as a promising electrochromic, battery cathode material, and gas sensor.[102–104] Recent excitement has been driven by the high work function (6.6 eV) and hole transport

properties of MoO_{3-x}, which have been used to meaningfully improve conversion efficiencies for solar cells and OLEDs.[105–107] Despite these numerous exciting bulk properties, MoO_3 has received limited attention in two-dimensional (2D) form. Initial studies of 2D MoO_3 and MoO_{3-x} have indicated great potential; few-layer MoO_{3-x} has shown ultra-high mobility (>1100 $cm^2\ V^{-1}\ s^{-1}$) due to high-dielectric constant Coulomb scattering suppression.[14] Nanoscale MoO_{3-x} has also shown broadband photodetector response with high photoresponsivity.[35] Further, chemically exfoliated 2D MoO_{3-x} flakes have been shown to have high enough conductivities to sustain plasmonic resonances in the visible regime and can be made into conductive inks.[62, 108] MoO_3 has also been used to modify other 2D materials in advantageous ways. Thin film MoO_3 has been used to hole dope graphene and improve contact resistance for MoS_2.[22, 23, 109] These preliminary findings indicate that 2D MoO_3 would be a beneficial material to incorporate within interacting, multicomponent, 2D heterostructures.

However, progress in 2D MoO_3 has been stalled in part due to the lack of large-area, "electronic-grade" syntheses. Initial structural and electronic studies have been conducted on sheets fabricated via mechanical exfoliation, chemical exfoliation, or hydrothermal means, but these techniques suffer from low yield, high defect densities, and organic contaminants respectively.[62, 110, 111] Physical vapor deposition directly on SiO_2 substrates allows for rapid identification of few-layer samples as well as provide high-quality samples ready for broader characterization and device integration.[112]

We report a physical vapor deposition synthesis of few-layer MoO_3 directly onto SiO_2 substrates. These few-layer nanosheets are of high quality, as confirmed by a number of techniques including high-resolution transmission electron microscopy (HRTEM, gives

structural information), scanning electron microscopy (SEM, gives morphology information), atomic force microscopy (AFM, gives higher resolution morphology information) and Raman spectroscopy (gives characteristic phonon mode information). We also explore the electronic structure changes due to 2D confinement. Density functional theory (DFT) calculations show that monolayer confinement of MoO_3 leads to a modest increase in the bandgap.

The critical sub-stoichiometry that underlies MoO_{3-x}-based technologies has typically been induced by a H^+ ion post-treatment.[14, 100] However, these H^+ ion-based processes are difficult to control and quantify. A quantifiable oxygen vacancy introduction process could provide a more coherent link between the MoO_{3-x} structure and transport properties. We report a dose-controlled electron-beam irradiation technique to introduce vacancies into few-layer MoO_3.

Prior TEM studies have indicated that bulk or nanostructured MoO_3 can be reduced to MoO_{3-x} and MoO_2 via electron-beam irradiation.[113, 114] In recent years, electron irradiation has offered the possibility of engineering materials at the nanoscale.[115, 116] Building on these preliminary studies and invoking in-situ transport studies, we provide a detailed structure-transport correlation between electron-beam irradiation-induced oxygen vacancy introduction and resultant n-type doping across a variety of MoO_{3-x} layer numbers, down to trilayer thickness. In-situ core loss and monochromated low-loss electron energy loss spectroscopy (EELS) studies provide quantitative insights into the chemistry and band-gap changes during the evolution of the few-layer MoO_3 into few-layer MoO_{3-x}, giving additional evidence of oxygen vacancy introduction during irradiation. Bringing these different characterization results and DFT calculations together,

the Knotek-Feibelman mechanism of radiolysis is presented as the mechanism of oxygen vacancy and n-type carrier introduction. DFT calculations indicate which crystallographically distinct oxygen vacancies are most energetically favorable to form during the doping process. Transport studies show the resistance of the MoO_{3-x} 2D sheet can be modified by over four orders of magnitude via controlled electron-beam doses. As such, MoO_{3-x} shows the properties of a highly tunable 2D functional material. This chapter highlights the exciting potential of MoO_{3-x} as a functional component in fully 2D heterostructures as well as provides a synthesis technique to reliably fabricate MoO_3 and MoO_{3-x} in few-layer form.

3.2. Results and Discussion

3.2.1. Comparison of 2D and bulk MoO_3 electronic structure

MoO_3 is an orthorhombic layered structure (space group Pnma), as indicated by Figure 3.1a. Each fundamental bilayer is comprised of two layers of distorted MoO_6 octahedra and is ~1.4 nm thick. As shown in Figure 3.1a and 3.1d, there are three symmetrically inequivalent oxygen sites (red spheres) in $\alpha - MoO_3$: a singly coordinated oxygen O_1, a doubly coordinated oxygen O_2, and a triply coordinated oxygen O_3. Each distorted Mo octahedra is comprised of a Mo atom (white sphere) bound to one O_1 atom, two O_2 atoms, and three O_3 atoms.

In stoichiometric form, MoO_3 has been experimentally determined to have a large indirect bandgap (~3.2 eV).[117, 118] DFT + U calculations were performed to give insight into the electronic structure of the monolayer form (Figure 3.1e compared to the bulk form (Figure 3.1b. The bulk case shows an indirect bandgap of 1.96 eV, similar

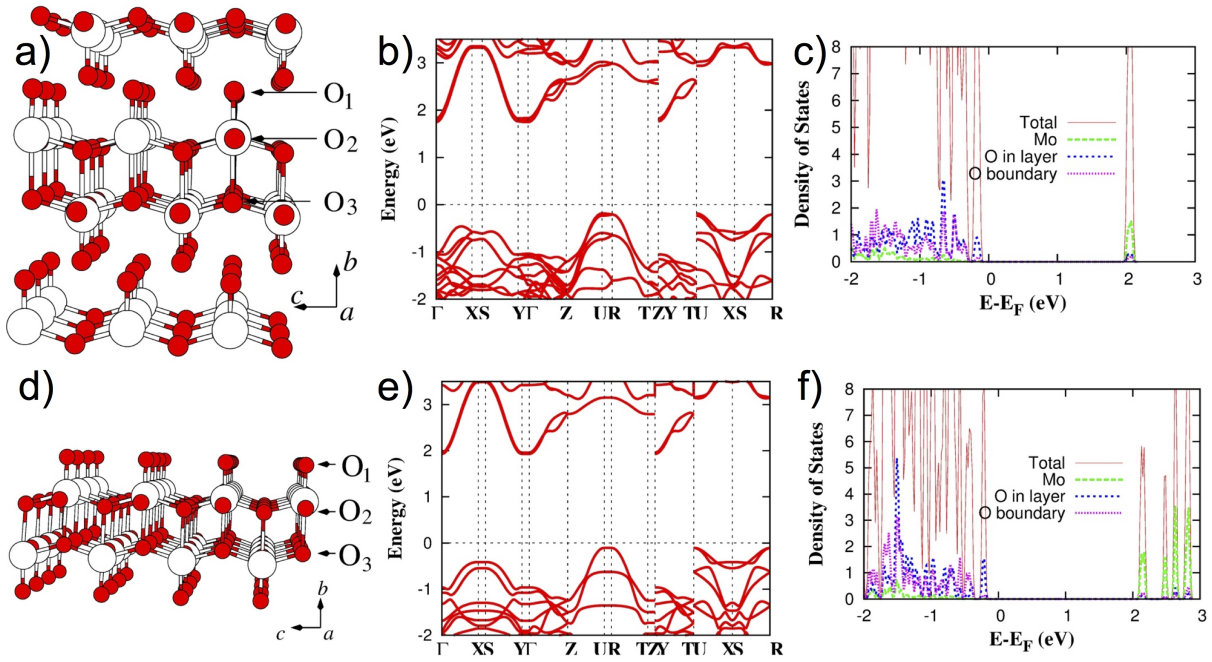

Figure 3.1. DFT calculated electronic structure of the bulk and monolayer MoO_3. a) Bulk structure with oxygen positions labeled, b) bulk electronic structure, c) bulk density of states. d) Monolayer structure with oxygen positions labeled, e) monolayer electronic structure and f) monolayer density of states. Reproduced with permission from [98].

to other DFT + U studies of MoO_3.[119, 120] The DFT-calculated electronic structure of a MoO_3 monolayer shows a slightly larger indirect bandgap of 2.03 eV. Quantum confinement effects in 2D materials often induce a more significant bandgap increase than we found in MoO_3.[121] To understand this relatively modest increase in band gap, we examine the DFT-calculated density of states for both the bulk and monolayer, shown in Figure 3.1c and Figure 3.1f. Since the valence band maximum (VBM) and conduction band minimum (CBM) states are dominated by states from the Mo and position O_2 and O_3 oxygen atoms, which are screened from confinement effects, monolayer confinement only leads to small changes in the electronic structure. The terminal oxygen atoms (O_1

position in Figure 3.1a, would experience the strongest confinement effects, but only have a minor contribution to the CBM and VBM. This simple structural argument explains why the bandgap of MoO_3 is only modestly affected by 2D nanostructuring.

3.2.2. Vapor-based synthesis of few-layer MoO_3

Few-layer MoO_3 sheets were grown via low-pressure physical vapor deposition (PVD). The deposition experimental set-up is shown in Figure 3.7. MoO_3 powder is placed in the hot zone of the furnace and carried downstream with a dry air carrier gas. Dry air carrier gas is crucial to maintain oxygen stoichiometry and deposit the layered MoO_3 structure (vs. using an inert carrier gas to deposit monoclinic MoO_2). The growth is carried out at 700 C for < 5 min and then quickly quenched by opening the furnace to stop further growth. The synthesis method produces a range of thicknesses of MoO_3 sheets. By using 300 nm SiO_2/Si substrates, few-layer samples are easily identified by optical contrast, similar to other 2D materials.[112] Figure 3.2 shows structural characterization of the resultant bi- and few-layer MoO_3 samples. Figure 3.2a displays an optical micrograph corresponding to the AFM and SEM images in Figure 3.2b and Figure 3.2c. The synthesized nanosheets are continuous and of high-quality, with domain sizes on the order of 10 microns. The thickness has been determined by AFM analysis to be 3 nm, which corresponds to a bilayer. Figure 3.2d shows a TEM image of another few-layer sheet. The indexing of the selected area diffraction pattern (inset of Figure 3.2d confirms the orthorhombic structure in the Pnma symmetry. An HRTEM image of the MoO_3 lattice fringes is shown in Figure 3.2e. While there is indication of beam damage, which will be explored in more detail below, the HRTEM micrograph confirms the good crystal quality of these flakes.

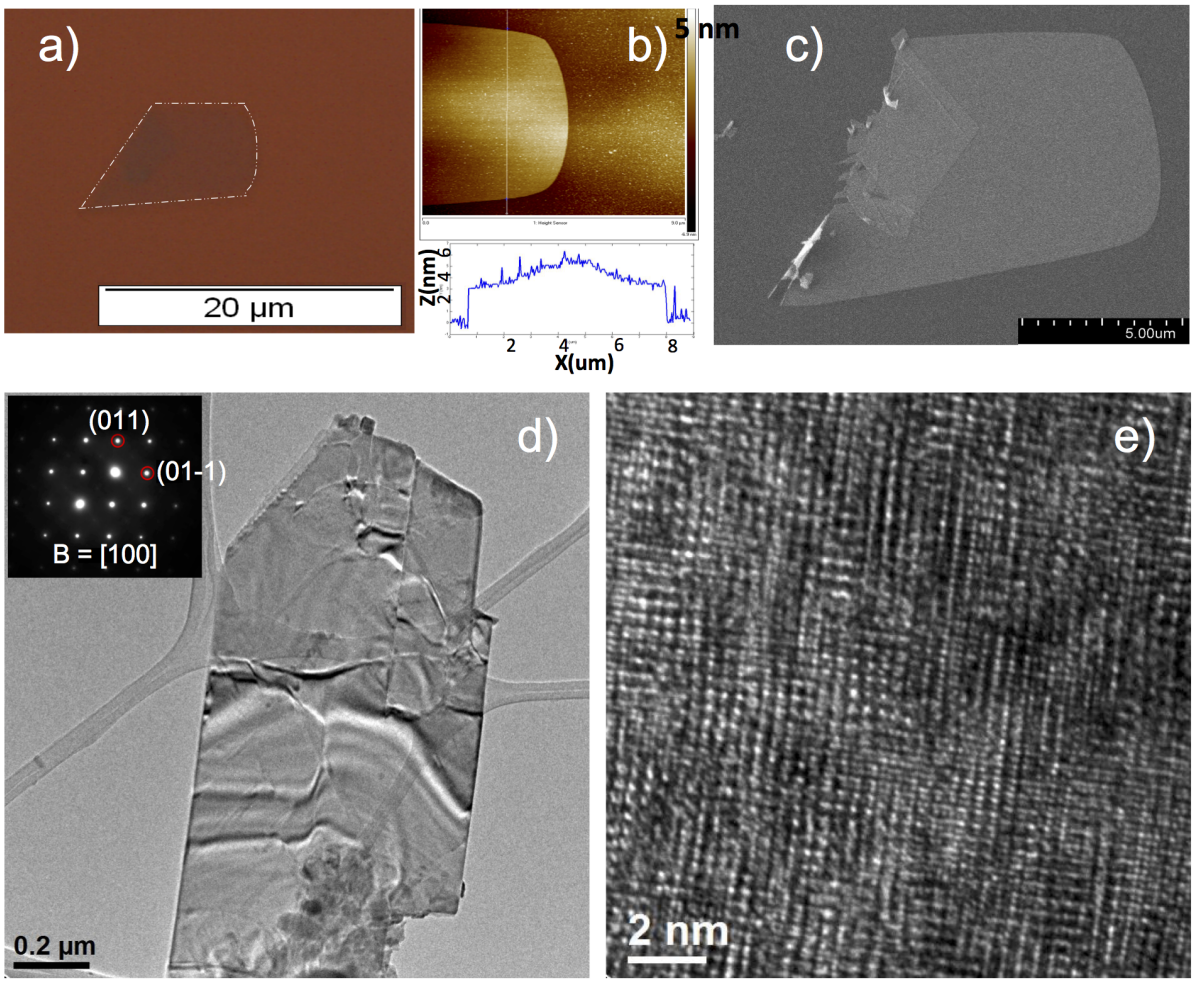

Figure 3.2. Structural characterization of 2D MoO_3. a) Optical image of a bilayer MoO_3, b) corresponding AFM image showing 3 nm height corresponding to bilayer thickness, c) corresponding SEM image. d) TEM image of few-layer sample, inset shows diffraction pattern indexed to Pnma crystal structure. e) HRTEM image showing MoO_3 lattice fringes and beam damage. Reproduced with permission from [98].

Raman spectroscopy was used to probe the changes in phonon modes as a result of extreme geometric confinement and high surface to volume ratios in the 2D crystals. Figure 3.8 shows the Raman spectra of the grown MoO_3 sheets of various thicknesses. As the thickness of the sheets decreases, the overall intensity of the Raman scattering decreases

in lockstep. Ultra-thin 4-nm sheets still show the key MoO_3 Raman modes, which serve as an additional confirmation of the MoO_3 structure. There is some disagreement in the literature about how to index the MoO_3 peaks and their physical interpretation.[122, 123] The Raman modes here were indexed based on the assignments reported by Camacho-Lopez et al.[123] Beyond the traditionally indexed MoO_3 vibrational modes, an additional peak at ~618 cm^{-1} was observed. This peak has been attributed to the hydrated form of MoO_3, which suggests there may be some surface hydration experienced by the few-layer sheets.[110]

3.2.3. Electron irradiation-induced formation of few-layer MoO_{3-x}

In the 2D form, sub-stoichiometry has been introduced to date via H^+ ions.[14] Due to the environmental sensitivity of 2D MoO_3, device fabrication is difficult. As a result, transport properties of MoO_3 have only been reported in the published literature for thicknesses greater than 6 nm.[14, 124] An in-situ electron beam irradiation technique was developed to introduce oxygen vacancies controllably and quantifiably and to overcome these fabrication difficulties.

3.2.3.1. In-situ transport studies. In order to investigate the tunable transport properties of the PVD-grown 2D MoO_3, in-situ transport measurements were performed with a nanoprobe station inside a SEM. This station allows us to bring conductive probes directly in contact with the sample and measure resistance as a function of electron dose. This gives us the ability to forego the frequently damaging lithographic device fabrication process and to probe the pristine intrinsic properties of the MoO_3 nanosheets. Figure 3.3a shows these in-situ nanoprobes in contact with a MoO_3 nanosheet. Figure 3.3b shows

example current-voltage (I-V) curves for a 5 nm-thick sheet as a function of different electron doses. The electron dose is introduced via carefully timed exposures and the electron-beam is blanked during electrical transport measurements. Before exposure, the current is in the sub-nanoamp regime (a 5 nm-thick example is shown in Figure 3.9a. The I-V curves show a dramatic increase in current as a function of electron-beam dose. In the 5 nm case, after an electron dose > 3000 $\mu C/cm^2$, there is a jump in current of over three orders of magnitude compared to before irradiation. This rise in current continues with dose before gradually saturating. After irradiation, the I-V curves are generally linear and ohmic in character. In order to rule out carbon contamination as the new transport route, we measured I-V curves immediately adjacent to an exposed flake in the area of exposure. This adjacent area of SiO_2 with carbon contamination showed sub-nanoamp current even after an electron dose $>75{,}000$ $\mu C/cm^2$ (shown in Figure 3.10). Given such low current, the influence of carbon contamination on 2D MoO_{3-x} transport properties can thus be excluded.

The resistance as a function of electron-beam dose has been measured across a number of flake thicknesses, as shown in Figure 3.3c. Resistance is reported for flakes down to trilayer (4 nm) thickness. Across the flake thicknesses, there is an exponential decay in resistance as a function of dose, and then at higher doses, saturation is present. There is no clear thickness dependence in the final resistance value. In the semi-classical Boltzmann transport model, for a given order of magnitude drop in resistance we expect a similar magnitude increase in carrier concentration. Carrier concentration effects on resistance were calculated from the Boltzmann transport equation, as shown in Figure 3.11b. To put the comparison in similar terms, both the experimental and theoretical changes are

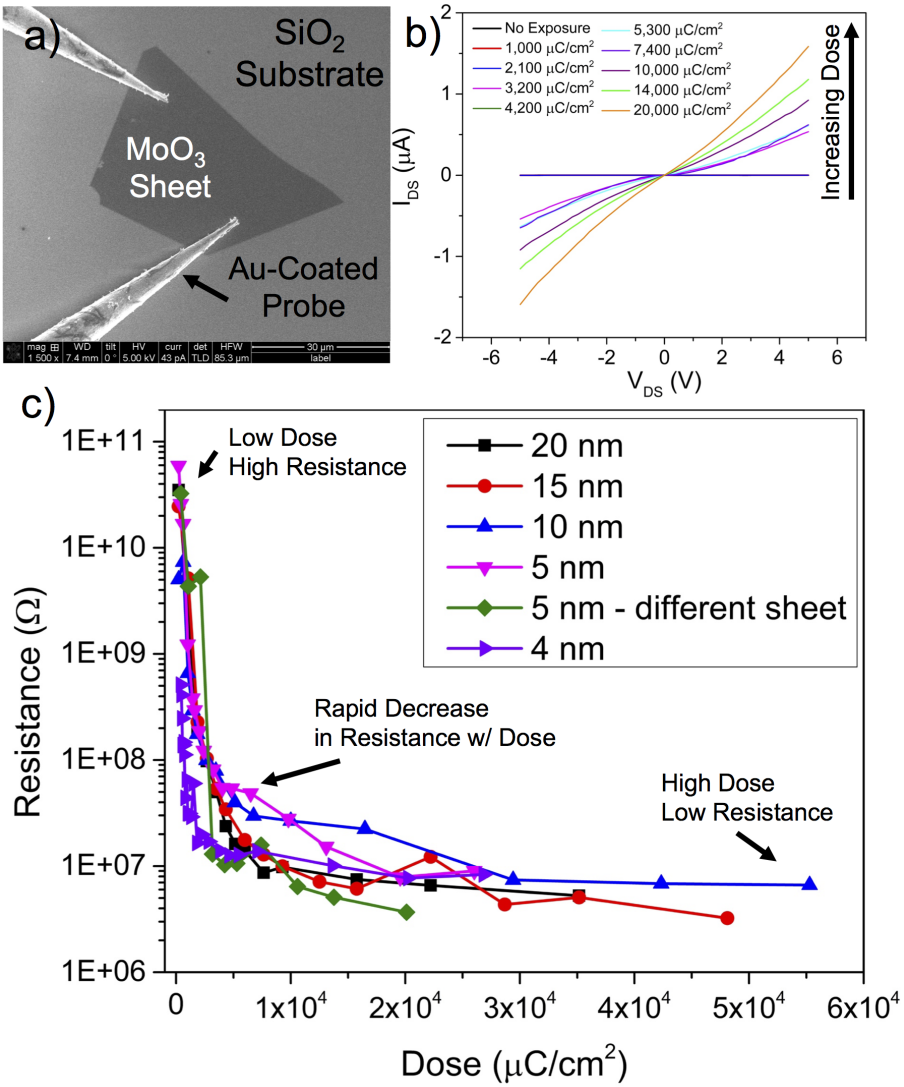

Figure 3.3. Electrical characterization of few-layer MoO_3 as a function of electron dose. a) SEM image of nanoprobes in contact with 20 nm MoO_3 sheet. b) Current-voltage (I-V) curves at a number of doses for a 5 nm MoO_3 sheet. c) Resistance as a function of electron dose across a number of MoO_3 thicknesses. Reproduced with permission from [98].

calculated in terms of relative resistance. The relative resistances in Fig 3.11a were indexed to the most resistive sheet (5 nm, no electron dose). Figure 3.11b was indexed to 10^{15} carriers/cm^3, which has previously been reported to be the carrier concentration of

stoichiometric MoO_3.[125] As expected, higher carrier concentrations correlate to lower relative resistances. Comparing the resistance changes in the experimental and theoretical data, we extrapolate that after the MoO_3 nanosheets are irradiated with doses greater than $10,000$ $\mu C/cm^2$, the carrier concentration has increased to over 10^{18} carriers/cm^3. This result highlights the tunable nature of the irradiated 2D MoO_3 nanosheets.

Raman spectroscopic studies as a function of dose were also investigated (shown in Figure 3.11c and 3.11d. A number of 10 nm-thick nanosheets were exposed to a variety of doses across the dose range shown in Figure 3.11c. The electron dose exposure suppresses the key MoO_3 modes. Previous reports have highlighted the reduction in Raman mode intensity with H_2-based reductions of MoO_3 to MoO_2.[122, 126] Figure 3.11d quantifies the intensity suppression of the key MoO_3 Raman modes as a function of electron dose. We propose that this suppression is due to two reasons: reduction of the MoO_3 to MoO_{3-x} and local disorder introduced by the electron-beam.

3.2.3.2. In-situ TEM-EELS studies. In order to gain further insight on the effect of electron irradiation on the local chemistry, EELS spectra were recorded at regular time intervals during a low-dose irradiation process (432 $\mu C/cm^2.s$) in a STEM microscope. EELS is a technique of choice to get local (even atomic level) chemical information from nanostructures. In particular, a wealth of precise and accurate chemical information on molybdenum oxides can be extracted from the conjugated analyses of the O-K and Mo-$M_{2,3}$ edges.[127] Figure 3.4a shows the EELS core-loss spectra of a 2D nanosheet taken as a function of the irradiation time. The thickness of the corresponding nanosheet has been estimated from the low-loss monochromated EELS spectra and is between 8 and

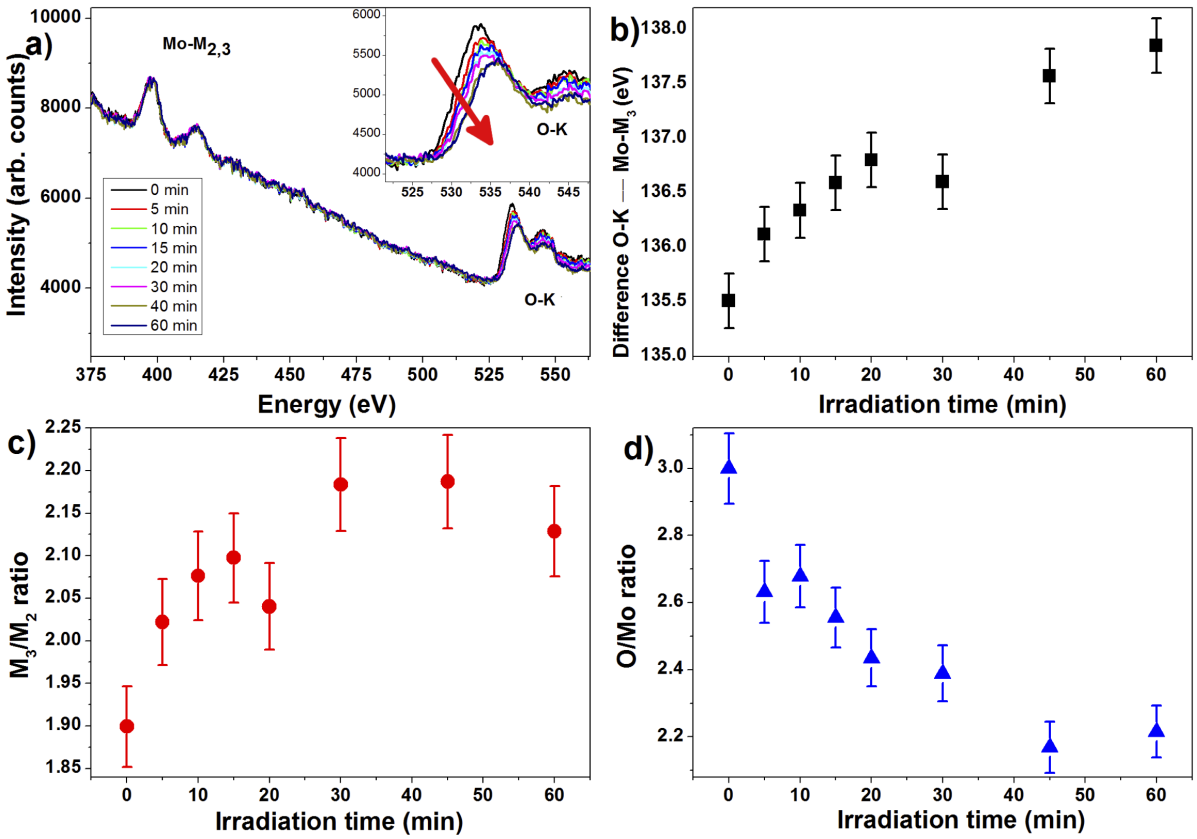

Figure 3.4. a) EELS core-loss spectra of a 2D nanosheet showing the Mo-M_3 and the O-K edge. The spectra were taken as a function of the irradiation time in the low-dose regime (dose = 432 $\mu C/cm^2$.s). The inset shows a magnified view of the spectra close to the O-K edge. The red arrow highlights the shift to higher energy and the intensity decrease of the O-K pre-peak. b) Energy difference between the maxima of the O-K edge pre-peak and the maximum of the Mo-M_3 edge as a function of the irradiation time. c) Mo-M_3/M_2 intensity ratio as a function of the irradiation time. d) O/Mo ratio as determined by EELS elemental quantification as a function of the irradiation time. Reproduced with permission from [98].

10 nm. Figure 3.12 shows the carbon K-edge intensity does not increase with irradiation time, indicating no significant carbon contribution to EELS spectra changes.

A variety of EELS results show that low-dose electron irradiation of MoO_3 produces substoichiometric MoO_{3-x}. The O-K prepeak shift to higher energy (inset of Figure 3.4a

indicates a lower oxidation state of the transition metal linked to the oxygen atoms.[128] In accordance with reference [129], an increase in the difference between the O-K edge and the Mo-M_3 edge and an increase in the Mo-M_3/M_2 ratio both indicate a lower Mo-oxidation state. Electron irradiation of the few-layer sample led to the expected reduction in Mo oxidation state, as shown by the increasing values with irradiation time in Figure 3.4b,c. The decrease of the O-K edge integrated intensity with irradiation (inset of Figure 3.4a indicates oxygen loss. To quantify this process, the O/Mo ratio was derived by using a pristine sample as reference to extract the k-factors (Figure 3.4d. The O/Mo ratio decreases with the irradiation time and is equal to 2.6 and 2.2 after 5 and 60 min of irradiation, respectively. It is important to note that the fine structures of the O-K edge remain the same (except for the prepeak shift) during the whole experiment (inset of Figure 3.4a and that they do not agree with the MoO_2 or the MoO phases but correspond to the MoO_3 phase.[114, 129] These results confirm the creation of oxygen vacancies induced by the electron-beam in the low-dose regime, rather than a phase transformation.

Figure 3.5a shows the low-loss EELS spectra taken with a monochromated electron-beam on an unirradiated and an irradiated area (after 60 min) of the same nanosheet. For comparison, a low-loss spectra of bulk α-MoO_3 taken from reference [127] is also displayed. The energy-loss structures of the unirradiated area match well with those of bulk MoO_3, with a key difference in the A structure energy (5.8 eV for few-layer and 6.9 eV for bulk), although we should be cautious about comparison of spectra recorded with different microscopes. After 60 minutes of electron irradiation at low-dose, the low-loss spectrum is only slightly modified, further discounting the possibility of a phase transformation during low-dose irradiation. Both the unirradiated and irradiated low-loss

spectra do not match the spectrum of MoO_2. The A and P structure remain at the same energy but another contribution on the left side of the B structure can be highlighted (green arrow in Figure 3.5a. The B structure corresponds to a plasmon whose shape and intensity are strongly influenced by the presence of interband transitions linked to oxygen states.[127] The modification of the B structure could thus be due to the introduction of oxygen vacancies in the 2D MoO_3 nanosheet.

Finally, the bandgap was derived by performing a linear fit for the unirradiated and irradiated areas (inset of Figure 3.5a and, for both cases, was found equal to 3.2 eV. This result is important because it is in excellent agreement with experimental values for bulk MoO_3 [118] and thus confirms that the 2D nanostructuring of MoO_3 does not significantly alter the bandgap magnitude as highlighted by the present DFT calculations. It also confirms recent theoretical findings showing that the introduction of vacancies in MoO_3 does not alter the width of the bandgap but gives rise to gap states.[119] The analysis of the core-loss and low-loss spectra thus highlights that electron irradiation at low-dose of few-layer MoO_3 leads to the creation of oxygen vacancies in the MoO_3 network. These vacancies are therefore responsible for the increase of the conductance observed during the electrical measurements.

3.2.4. Mechanism of MoO_3 reduction

The mechanism of the oxygen vacancy introduction is proposed to be the Knotek-Feibelman mechanism for radiolysis, as depicted in Figure 3.5b. In this mechanism, the incident electron radiation creates an inner shell hole on the Mo site (Step 1 in the schematic). Next, an electron from a nearby oxygen atom has an interatomic Auger decay to the Mo inner

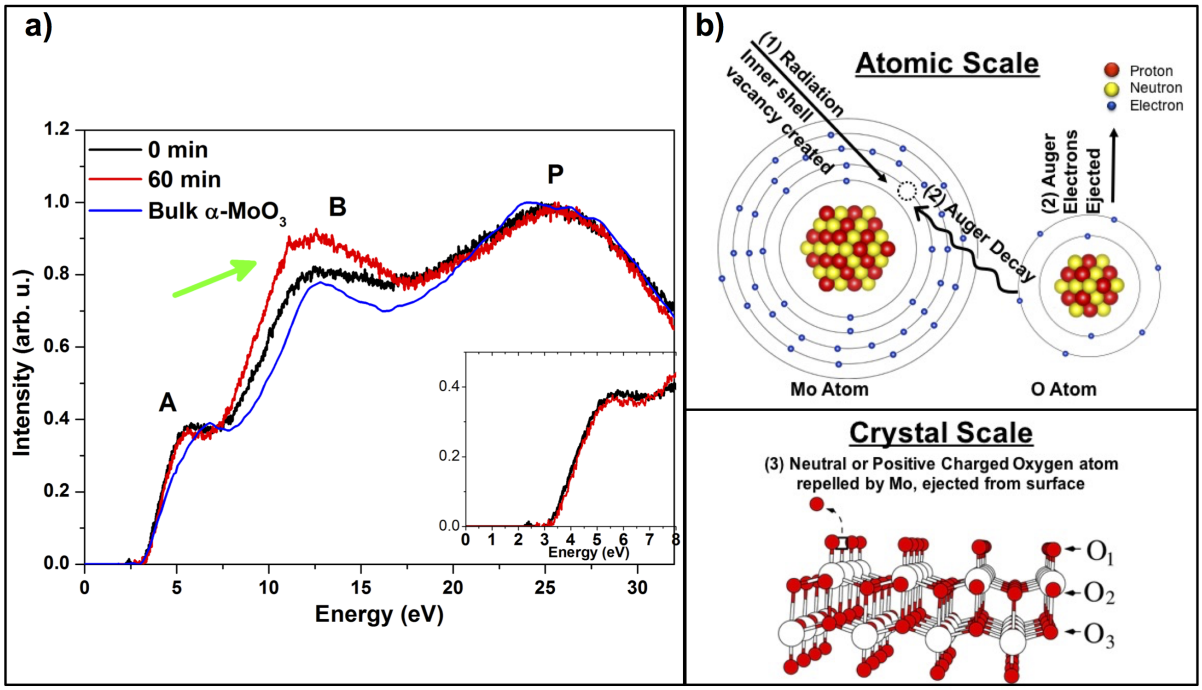

Figure 3.5. a) Low-loss EELS spectra taken from an unirradiated and an irradiated area (after 60 min) of the same nanosheet. The spectra were taken with the monochromator on (resolution 270 meV). For comparison the low-loss EELS spectra taken from reference [127] is also given in blue (resolution 0.8 eV). The green arrow highlights the presence of another contribution in the B structure for the irradiated area. The inset shows a magnified view of the bandgap area. b) Schematic of Knotek-Feibelman mechanism at the atomic and crystal length scales. Reproduced with permission from [98].

shell hole, and further Auger electrons are ejected from the oxygen atom (Step 2). At the crystal level, neutral or positive oxygen atoms are then repelled by the surrounding molybdenum atoms and are ejected from the surface (Step 3) until the sheet becomes conductive enough to screen the oxygen ions.[130] The oxygen vacancy gives rise to n-type doping behavior due to the presence of two leftover electrons per oxygen vacancy.

The outlined mechanism aligns nicely with the transport data. Oxygen vacancies are introduced, n-type doping the material to much higher currents until the MoO_3 nanosheet samples are sufficiently conducting to screen the oxygen atoms.

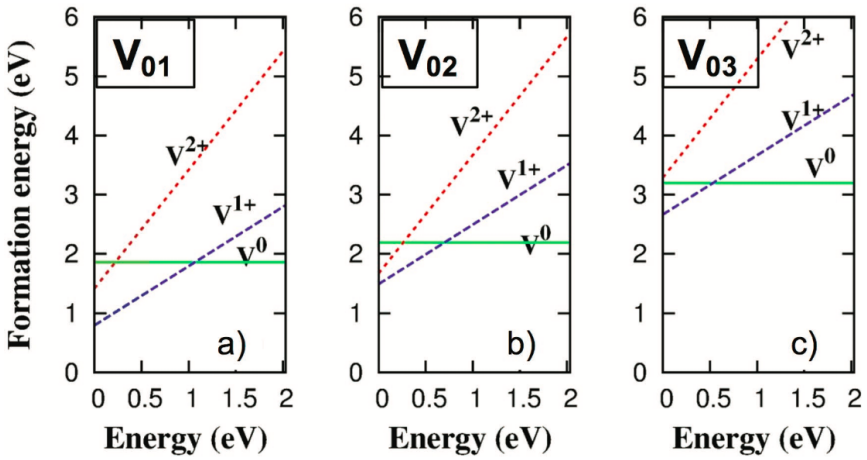

Figure 3.6. Oxygen vacancy formation energies as a function of Fermi level. a) V_{O1}, position O_1 vacancy, where the oxygen vacancy leads to the two donated electrons being localized on a single Mo center reducing it to Mo^{4+}. b) V_{O2}, the doubly coordinated O_2 vacancy leads to a polaron in which the two excess electrons localize on two surrounding Mo atoms. c) The triply coordinated O_3 vacancy also leads to a bipolaron, forming two Mo^{5+} sitting on opposite sides of the vacancy. Reproduced with permission from [98].

It is instructive to consider which crystallographic oxygen positions are favored for creating oxygen vacancies. DFT+U calculations were performed to calculate the energy of formation of oxygen vacancies at the different crystallographic positions (O_1, O_2 and O_3 from Figure 3.1) in a monolayer, as shown in Figure 3.6. The figure shows for each crystallographic vacancy position which resulting polaron, or a local polarization coupled to an electron, is most stable as a function of Fermi level. More details on each polaron

condition (V^0, V^{1+}, V^{2+}) are given in the Supporting Information. Our DFT+U calculations indicate that the terminal O_1 oxygen has the smallest formation energy (E^f_{VO1}) for all accessible Fermi levels and charge states. For the neutral case, these energies are ordered such that $E^f_{VO1} < E^f_{VO2} < E^f_{VO3}$ with calculated values of 1.85, 2.19 and 3.20 eV, respectively. This trend is similar to previous calculations by Tahini et al. on the bulk case, where the corresponding formation energies are 2.06, 2.86, 3.93 eV.[131] From these values we see that V_{O1} has a lower vacancy formation energy in 2D form (compared to bulk). During the reduction process, point defects should be favored by the terminal O_1 oxygens.

Combined, these results show that we can synthesize 2D MoO_3 and controllably introduce different levels of oxygen vacancies via the electron-beam, thereby tuning the electronic properties of few-layer MoO_3. This shows that few-layer MoO_{3-x} can be utilized as a functional electronic material in 2D form. Further, in-situ EELS studies and accompanying mechanism give insight into the MoO_{3-x} reduction process and corresponding measurable signatures (transport, Raman modes, EELS spectra).

3.2.5. Conclusions

Recent reports have highlighted the ultra-high mobility and promising transport characteristics of layered MoO_{3-x}, but full exploration of the few-layer properties have been hindered by the lack of a direct, vapor-phase growth. We report a facile PVD synthesis of high-quality, few-layer MoO_3 directly on SiO_2/Si substrates, enabling study of its exciting electronic properties. DFT+U calculations give insight into the electronic structure of the 2D MoO_3, showing that 2D confinement leads to a modest increase in bandgap. This

modest increase is because the CBM and VBM are comprised of electronic states that are largely screened from confinement effects. An electron-beam irradiation technique for introducing dose-controlled amounts of oxygen vacancies into the few-layer MoO_3, forming n-type doped MoO_{3-x}, is presented. Combining in-situ transport and TEM-EELS studies, we present a detailed structure-property relationship between the Mo-oxidation state reduction and decreased resistance in few-layer MoO_{3-x}. Few-layer MoO_{3-x} transport properties are reported for sheets down to trilayer thickness, the most 2D-like reported hitherto. The n-type doping process is further correlated with Raman mode suppression. Supporting these experimental results, a radiolysis-based reduction mechanism is developed in detail. DFT+U calculations inform which crystallographic oxygen positions are most energetically favored during the oxygen vacancy introduction process in 2D MoO_3. Few-layer MoO_3 shows enormous potential to be incorporated into 2D heterostructures and devices. For example, 2D MoO_3 could be used to hole-dope adjacent 2D materials, lowering contact resistance and creating 2D p-n junctions.[2, 23, 124] These results lay the groundwork and provide a simple synthesis to start investigations of integrating 2D MoO_3 into fully 2D heterostructures. This report provides an additional technique to create sub-stoichiometric 2D MoO_{3-x} to serve as an active n-type 2D material, and a thorough understanding of the modifications induced by low-dose electron irradiation on the local chemistry.

3.3. Methods and Supporting Information

3.3.1. Methods

Synthesis: MoO_3 sheets were grown in a 12 in Lindberg tube furnace. 50 mg of MoO_3 purchased from Sigma Aldrich (99.99 %) was placed inside of an alumina boat in the hot zone of a furnace within a 1 in silica tube. 300 nm SiO_2/degenerately doped Si substrates were placed downstream in a colder zone within the furnace (approx. 4 cm from center), suspended on top of alumina boats. The chamber pressure was kept at 2.8 Torr with a flow rate of 18 sccm of ultra-dry air serving as the carrier gas. The furnace was heated to 675 C over 25 min, then to 700 C over 5 min, before quenching by opening the furnace.
(S)TEM and EELS: Preliminary TEM studies were carried out using a JEOL 2100 microscope at 200 kV. The influence of electron irradiation at low-dose on the local chemistry of 2D MoO_3 was studied by using an FEI Titan Low-Base microscope operated at 80 kV and equipped with a Cs probe corrector, a monochromator, an ultra-bright X-FEG electron source and a Gatan Tridiem ESR 865 EELS spectrometer. The electron dose during electron irradiation was equal to 432 $\mu C/cm^2$.s and the irradiation time was up to 60 minutes. During irradiation, core-loss EELS spectra were collected in STEM mode, the energy resolution was 1 eV with a dispersion of 0.73 eV/pixel and the acquisition time was about 0.5 second/pixel (total acquisition time ~40 seconds). With this set-up, the convergence and collection angles were 36 and 51 mrad, respectively. To increase the signal/noise ratio the EELS spectra were recorded in spectrum image mode[132, 133] and the datasets were then de-noised with the open-source program Hyperspy by using principal component analysis routines.[132, 134] To minimize the systematic error from peak positions, the maximum of

the Mo-M_3 edges was first aligned to the same energy-loss (397.8 eV). Then, determination of the Mo-M_3/M_2 ratio and O/Mo elemental quantification were performed following the methodology described in Lajaunie et al.[129] In particular, the determination of the k-factors was done by using the unirradiated sample as reference and by using an energy window of 15 eV as it yields the best precision for elemental quantification. Low-loss spectra were also acquired on the same nanosheets with the monochromator on. In this case the energy resolution was about 270 meV with a dispersion of 0.02 eV/pixel. The relative thickness t/λ was calculated by using the Fourier-log algorithm.[135] For this purpose a zero-loss peak (ZLP) taken in the vacuum in the same experimental conditions. The absolute thickness was then determined by estimating λ with the modifed Iakoubovskii formula which yielded a value of $\lambda = 98$ nm for α-MoO_3.[135, 136] This method has been shown to yield a reasonable estimation of absolute thickness.[127] After subtraction of the ZLP, the bandgap was determined by using the linear fitting method which yields reliable results for monochromated spectra.[137, 138] The most representative spectra were submitted to the EELS Database as references.[139]

Raman Spectroscopy: Raman spectra were taken on Horiba LabRAM HR Evolution. Spectra were taken with a 532 nm excitation laser with a max power of 50 mW, with neutral density filters at 0.1 % (5 min x 2). Backgrounds were fitted and subtracted to highlight the key features.

In-Situ Transport: In situ electron-beam irradiation and transport measurements were taken using a Kleindiek nanomanipulation system in a FEI Helios Nanolab SEM/FIB. Electrical measurements were taken with a Keithley 4200 Semiconductor Characterization System. Tungsten probes (Micromanipulator, model 7X) were coated with 100 nm

Au to minimize contact resistance.

Theoretical Calculations:

DFT Calculations: We use periodic boundary conditions and a plane wave basis set as implemented in the Vienna ab initio simulation package.[140] The total energies were numerically converged to approximately 3meV/cation with spin-orbit coupling using a basis set energy cutoff of 500 eV and dense k-meshes corresponding to 3000 per reciprocal atom k-points in the Brillouin zone. Our theoretically relaxed Pnma MoO_3 lattice constants are respectively a=3.91 A, b=13.70 A, and c=3.69 A, which are in good agreement with the experimental crystal structure (a = 3.96 A, b = 13.86 A, and c = 3.70 A)[141] and previous calculations(a = 3.908 A, b = 13.831 A, and c = 3.694 A)[127] taking into account Van der Waals forces by using the semi-empirical DFT-D2 method implemented in VASP.[142] It is known that a dielectric crystal responds to the presence of an electron by exhibiting a local lattice distortion to screen the electronic charge. This local distortion leads to polarization coupled to an electron known as a small polaron if the extent of the lattice distortion is on the order of a unit cell. DFT is known not to be able to correctly describe polaronic states in oxides. We therefore resort to using DFT+U to correctly describe the localized electronic states. The total energies and relaxed geometries were calculated by DFT within the generalized gradient approximation of Perdew-Burke-Ernzerhfor the exchange correlation functional with Projector Augmented Wave potentials.[143] The U value was set to 6.3 eV based on the work by Coquet and Willock.[120]

Oxygen vacancy formation energy calculations: To calculate oxygen vacancy formation energies, we consider various oxygen vacancies in monolayer configurations. In the monolayer structure, the 15 A vacuum is added in the cell to avoid slab interactions. As

indicated above, an oxygen vacancy gives rise to n-type semiconducting behavior due to the presence of two leftover electrons per oxygen vacancy. We consider various oxygen vacancies coupled with different polaronic configurations. As shown in Fig3.1d, there are three symmetrically inequivalent O sites in α-MoO_3: a singly coordinated oxygen O_1, a doubly coordinated oxygen O_2, and a triply coordinated oxygen O_3. The removal of O_1 leads to the localization of the two excess electrons on the neighboring Mo (Mo^{4+}). This defect can be viewed as a defect complex formed by a positively charged oxygen vacancy (V_O^{2+}) and the two localized electrons on the Mo^{4+} ion leading to an overall neutral complex. Vacancies on the two fold coordination O_2 site leads to the creation of a bi-polaron, in which two electrons are localized on two separate Mo^{5+} sites. These two Mo^{5+} ions lie in the first and second coordination spheres relative to the vacant site, such that the two Mo^{5+} ions are connected by an O ion. For the V_{O3}, there are two possible polaron configurations of two Mo^{5+}. One is that two Mo^{5+} sitting on opposite sides of the vacancy, and the other one with two Mo^{5+} occupying upward and downward sides of the vacancy. By considering the vacancy and polaron configurations, the vacancy formation energy is defined as $E_f(V_O^q) = E_{tot}(V_O^q) - E_{tot}(pure) - 0.5E_{tot}(O_2) + q(E_{VBM} + E_F + \triangle\varepsilon)$, where $E_{tot}(V_O^q)$, $E_{tot}(pure)$ and $E_{tot}(O_2)$ are respectively total energy of host material with vacancy at different charged q state, total energy of pure host material, and total energy of molecular O_2. The oxygen correction is considered for the O chemical potential.[144] E_{VBM} is the energy of the top of the valence band, E_F the Fermi level restricted to values in the band gap, and $\triangle\varepsilon$ a factor that aligns the electrostatic potential to make the average potential in a bulk like region to the defect-containing supercell the same as average potential of the defect-free supercell. By considering other charge states commonly

adopted by V_O, namely, the singly positive (V_O^{1+}) and doubly positive (V_O^{2+})charge states and their dependence on the Fermi level within the band gap, we can identify regions of stability of these charges. Figure 3.6 shows that, for O_1, V_{O1}^{1+} (which acts as an electron donor) dominates when the Fermi level lies in the lower half of the band gap while V_{O1}^{0} is favored when the Fermi level lies in the upper part of the band gap. The similar trend are found in the other vacancies at O_2 and O_3 sites. The relative favorable V_O^{1+} at certain Fermi range indicates that these defects could donate an electron to the lattice.

Transport calculations: To calculate the electrical resistance we use the Boltzmann transport equation in the framework of semiclassical transport theory.[145] A convenient general way of describing the collisional term in the Boltzmann equation is to define a relaxation-time n,k for an electron in a band n at wavevector k. Then, we obtain the following expressions for the transport tensors as a function of the electron chemical potential (μ) that depends on the doping level of the system in a semiconductor and of the temperature T.

$\sigma_{ij}(T,\mu) = e^2 \int -\frac{df_\mu(T,\varepsilon)}{d\varepsilon}\sigma_{ij}(\varepsilon)d\varepsilon$

Here $df_\mu/d\varepsilon$ is the derivative of the Fermi-Dirac distribution function with respect to the energy. Moreover, we have defined the above quantities in terms of the transport distribution function, $\sigma_{ij}(\varepsilon)$ defined as

$\sigma_{ij}(\varepsilon) = \frac{1}{V}\sum_{n,k} v_i(n,k)v_j(n,k)\tau_{n,k}\delta(\varepsilon - \varepsilon_{n,k})d\varepsilon$

where the summation is over all bands n and over all the Brillouin zone $\varepsilon_{n,k}$, is the energy for band n at k and $v_i(n,k)$ is the i-th component of the band velocity at (n,k)

as given by $v_i(n,k) = 2\pi/hd\varepsilon_{n,k}/dk_i$. Note that the value of chemical potential depends on temperature and carrier concentration, then the transport tensors are also related to temperature and concentration. The relaxation time in principle depends on the band index and wavevector direction. In our case, we consider the relative resistance by taking a reference resistance value of at the carrier concentration of 1 x 10^{15} cm^{-3} to avoid relaxation time identification.

3.3.2. Supporting Figures

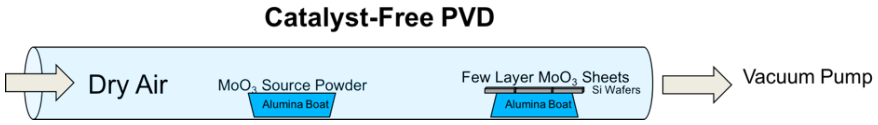

Figure 3.7. Model of low-pressure PVD growth set up. Reproduced with permission from [98].

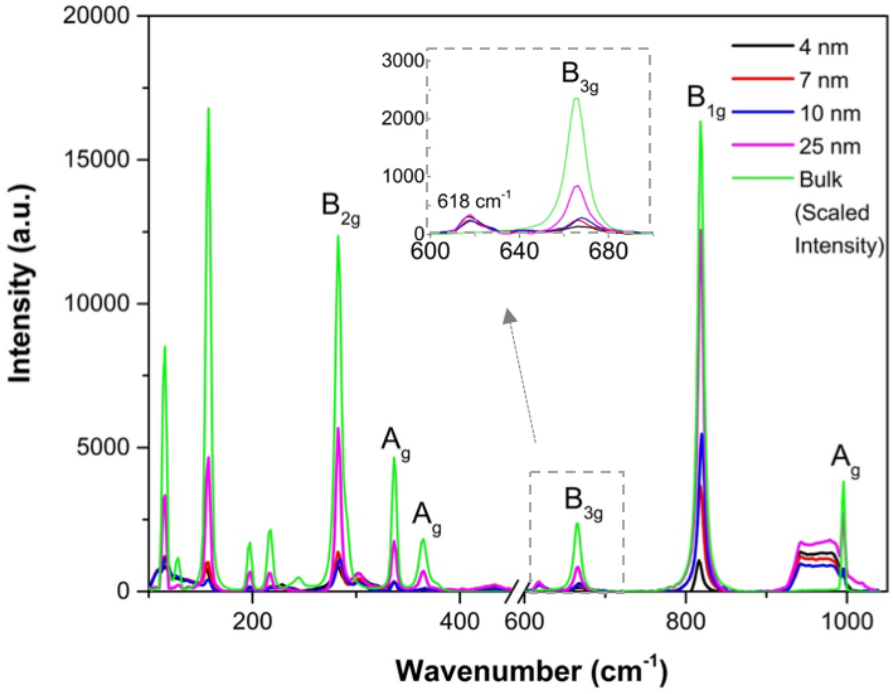

Figure 3.8. Raman spectroscopy of few-layer MoO_3. Full MoO_3 Raman spectra at a variety of thicknesses, inset of hydrated and B_{3g} peak. Reproduced with permission from [98].

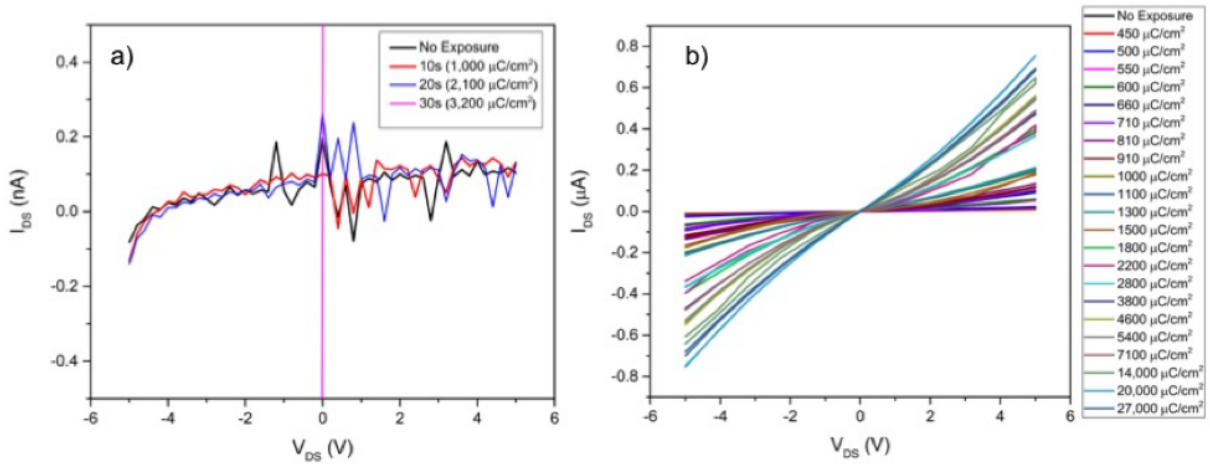

Figure 3.9. a) Current-Voltage (I-V) curves in low-dose regime for a 5 nm sheet. b) I-V curves at a number of doses for a trilayer (4 nm) MoO_3 sheet. Reproduced with permission from [98].

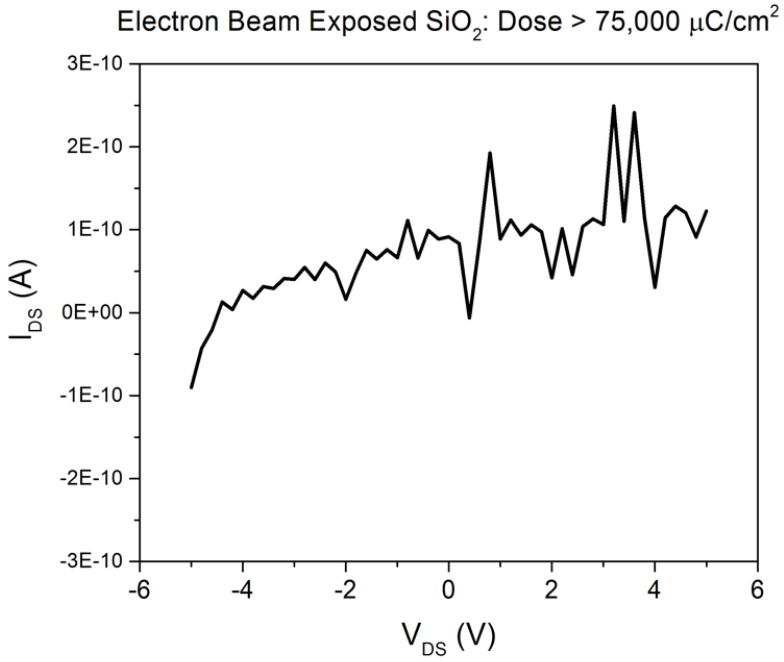

Figure 3.10. Current-Voltage measurement of electron beam exposed SiO_2. Even after a dose > 75,000 $\mu C/cm^2$, the current is in the sub-nanoamp current regime, suggesting minimal carbon contamination transport influence. Reproduced with permission from [98].

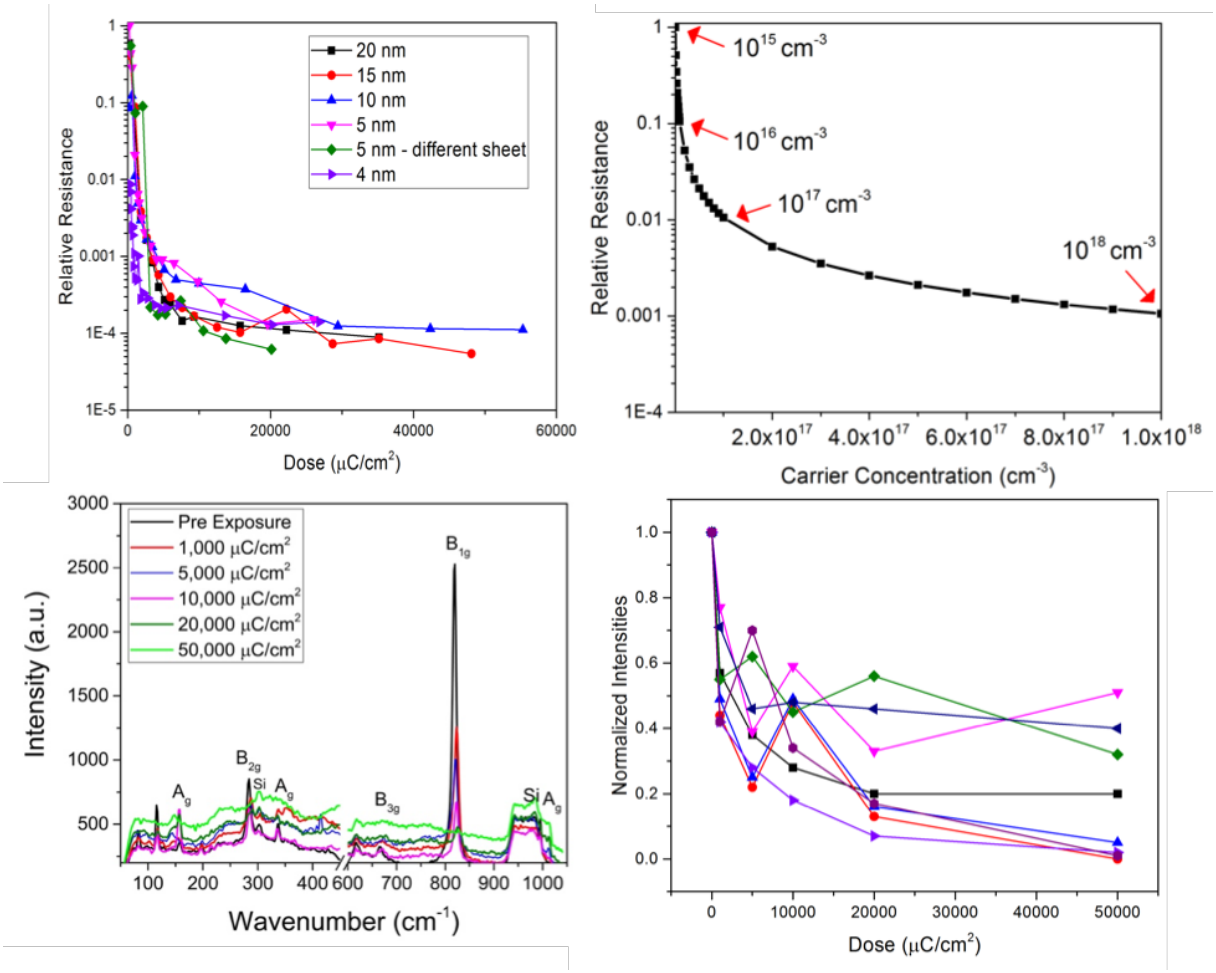

Figure 3.11. Relative resistance of few-layer sheets and Raman spectroscopy of 10 nm MoO_3 sheets as function of dose. a) Relative resistance of sheets, indexed to the most resistive 5 nm sheet with no exposure, b) DFT-calculated relative resistance as a function of carrier concentration, indexed to $10^{15}/cm^3$ carrier concentration, c) full spectra of 10 nm sheets at a number of dose levels, d) intensity of key MoO_3 peaks as a function of dose. Reproduced with permission from [98].

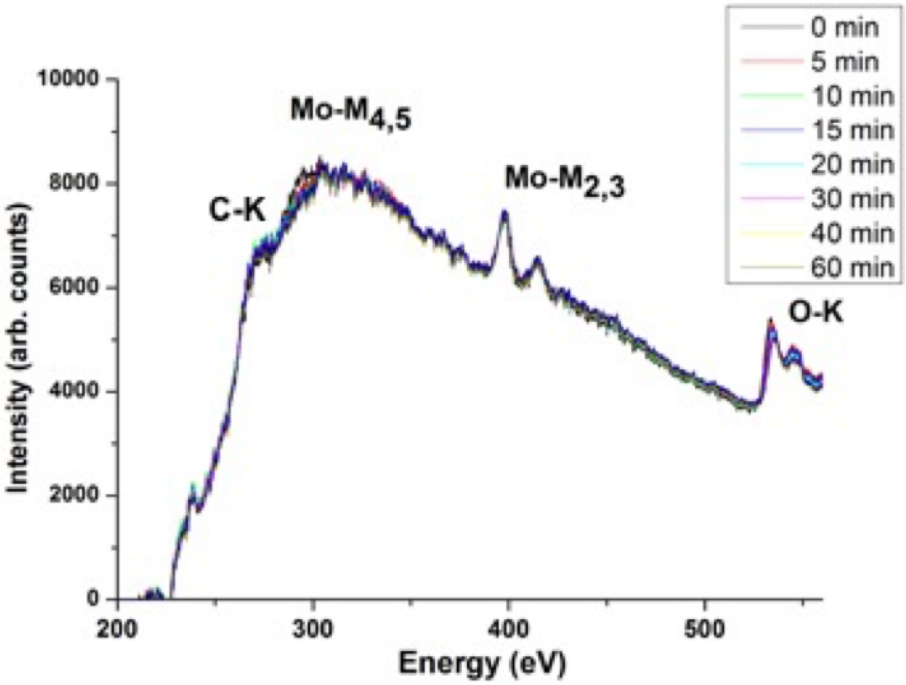

Figure 3.12. EELS core loss spectra showing carbon K Edge. The C-K edge does not increase with irradiation time, indicating no significant carbon contribution to the sample analysis. Reproduced with permission from [98].

CHAPTER 4

Platform CVD synthesis of the 2D TMDs and their heterostructures

4.1. CVD synthesis of the TMDs and their heterostructures

With their technologically-relevant band gaps, electron mobility, and optical responses, the TMDs have emerged as an attractive class of materials to the 2D community. Led by the work of Dr. Jeffrey Cain, we developed CVD syntheses to reliably produce high-quality, large-area monolayer growths of MoS_2, WS_2, $MoSe_2$, and WSe_2. All of these growths rely on the metal oxide-based CVD described in the introduction. A metal oxide precursor (MoO_3, WO_3) is reacted in the vapor phase with a chalcogen vapor (S, Se) in an inert environment to create TMD molecular units that are deposited as monolayers on lower-temperature substrates. The CVD growths produce the TMD 2H phase with direct bandgaps. In alignment with chalcogen bonding trends, the TMD sulfides are more stable than the selenides. We found that the selenides ($MoSe_2$, WSe_2) require perylene-3,4,9,10-tetracarboxylic acid tetra potassium salt (PTAS) seeding molecules to reliably produce monolayer growth. In addition, the differing vapor pressure of the precursor or chalcogen can have important experimental ramifications. Even small amounts of MoO_3 were found to dominate WS_2 growths, producing MoS_2-WS_2 heterostructures. Similarly, small amounts of sulfur present alloy with the TMD selenides to produce ternary alloys

of the form $MoSe_{2-x}S_x$. We took advantage of these precursor vapor pressure differences to develop a suite of TMD heterostructures and alloys.

Inspired by the Time-Temperature-Transformation (TTT) diagrams of traditional metallurgy, we developed a set of CVD principles and protocols to create complex structures: TMD heterostructures and alloys. Figure 4.1 shows the suite of heterostructures and alloys we can fabricate for both the MoS_2-WS_2 and $MoSe_2$-WSe_2 systems. We can directly grow vertical heterostructures (V_H one TMD stacked on top of another), radial heterostructures (R_H one TMD grows laterally from the edges of the original TMD), hybrid structures (H_H a combination vertical and radial structure) and alloys of the form $Mo_xW_{1-x}S_2$ and $Mo_xW_{1-x}Se$. By making these complex structures synthetically-accessible, we enabled the nature of inter-layer coupling and its impact on the heterostructure physics to be explored. Current studies are underway utilizing these structures to characterize their resulting device properties.

4.2. Motivation for chemistry-based property engineering techniques

Despite these important advances, there are limits to what types of heterostructures and electronic junctions can be achieved via CVD-based heterostructure syntheses. Due to the high temperatures required for the vapor-phase reactions, only a few types of heterostructures have been directly grown to date, and generally from two different TMDs of the same dominant carrier. Further, substitutional doping techniques can lead to severe lattice scattering, which can lower charge carrier mobilities and device performance.[146] Similarly, the ability to pattern CVD growth has been limited. A few reports have been able to seed or template the growth of TMDs, such as MoS_2, but this type of templating

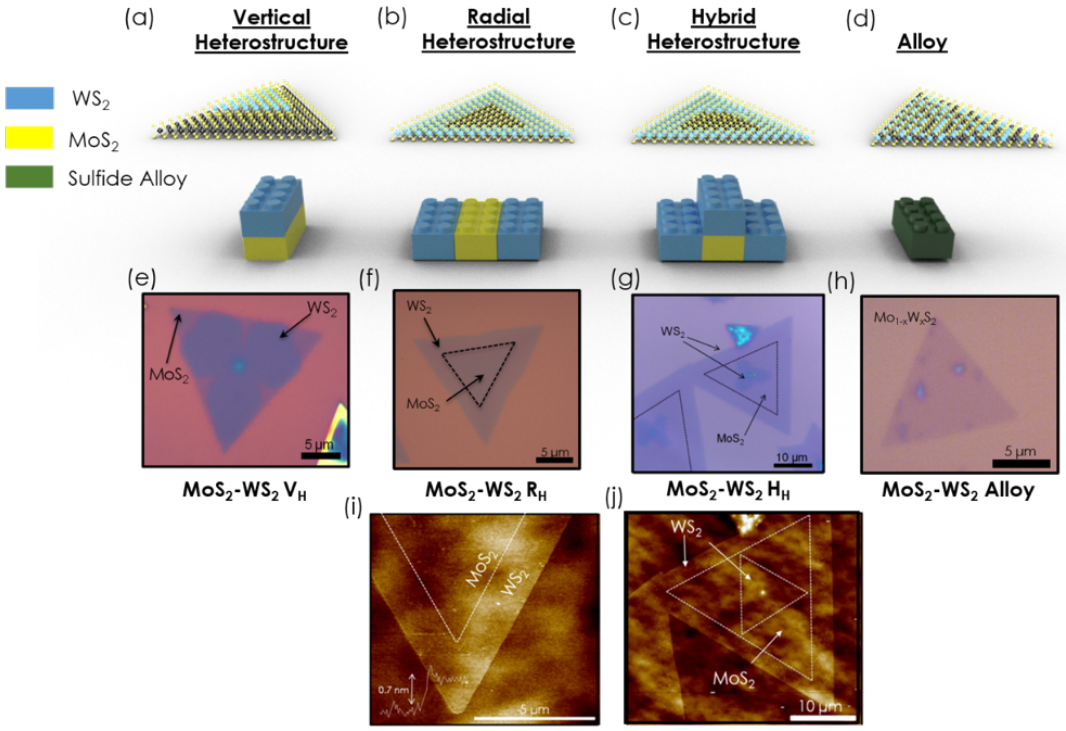

Figure 4.1. Heterostructure morphologies a)-d) Crystal structure schematics and building block representations of heterostructures and alloys. MoS_2, WS_2, and their alloy is represented by the blue, yellow and green building blocks, respectively. e)-h) Optical images of sulfide V_H, R_H, H_H, and alloy, respectively. AFM of i) R_H and j) H_H. Figure courtesy of [49].

can only pattern the materials on the scale of dozens of microns.[147, 148] A better way to engineer and pattern TMD properties in a precise fashion would enable a broad set of new devices and physics to be explored.

To that end, I investigated two methods of utilizing chemical treatments to tailor the properties of the TMDs. The first, utilizing lithium intercalation chemistry to incur the 2H to 1T' phase transition, degenerately n-type doping the material, proved to show interesting physics but have significant challenges to reliability and scalability. These

results are described in chapter 5. On a more promising note, we provide insights into a reliable p-type doping process utilizing the charge transfer dopant $AuCl_3$. As a surface interaction, the doping process should introduce fewer lattice scattering sites. In addition, we were able to develop a Polymer Pen Lithography (PPL) technique to precisely pattern the p-type dopant deposition on a MoS_2 monolayer. These results are described in chapter 6.

CHAPTER 5

Property engineering: phase engineering $MoSe_2$ via lithium intercalation

Adapted from Eve D. Hanson, Laura M. Lilley, Jeffrey D. Cain, Shiqiang Hao, Edgar Palacios, Koray Aydin, Chris Wolverton, Thomas J. Meade, Vinayak P. Dravid, Phase Engineering and Optical Properties of 2D $MoSe_2$: Promise and Pitfalls, Submitted, 2018.

This chapter explores using Li^+ ions as an n-type dopant on CVD-grown monolayer $MoSe_2$ to incur a phase transformation. It highlights both the promise of the resulting TMD 1T' physics, as well as the challenges of utilizing intercalation chemistry to modify monolayer TMD electronic properties for device applications (despite the hype in the 2D community).

5.1. Introduction and Motivation

The monolayer transition metal dichalcogenides (TMDs) have garnered extensive scientific interest due to their attractive electronic properties and potential suitability for integrated circuit architectures.[149] In particular, the molybdenum and tungsten-based TMDs have been extensively investigated due to their direct band gap in monolayer form and compatibility with various chemical vapor deposition growth techniques.[2, 150–152] The Mo and W-families of TMDs have a variety of crystalline phases. Figure 1.3 shows the three different phases for $MoSe_2$. The semiconducting 2H phase has a trigonal prismatic

coordination. The metastable octahedral 1T phase has no bandgap and shows metallic conduction. The metastable 1T' phase is a distorted octahedral phase with a very narrow bandgap, on the order of 0.1 eV and shows nearly metallic conduction.[153–157] The lattice parameters for the 2H phase and the 1T' phase are almost indistinguishable, with the 2H parameters as a=3.29 A, c=12.93 A, and the 1T' parameters a=3.29 A, c=12.93 A.[158, 159] The 2H phase belongs to space group P63/mmc, no 194. The 1T metallic phase is stabilized by electron donation, which is most often induced by lithium intercalation.[160] Lithiation is commonly achieved via reaction with n-butyllithium (n-BuLi), an extremely reactive organo-lithium reagent.[161] While promising, TMD-based device performance, such as those made from monolayers MoS_2 and $MoSe_2$, has been hindered by the prohibitively high contact resistance due to significant Schottky barrier formation with traditional contact metals such as gold.[162] Recent excitement in the community has been driven by a potential breakthrough in this contact resistance issue: phase engineering the TMD system into a two-phase heterostructure to improve transport characteristics.[59–61, 156, 163–166] In these reports, polymer masks (specifically PMMA) are used to control exposure to n-BuLi, resulting in the phase transition to the metastable 1T' phase in defined locations. This process can be used to create metallic 1T' contacts that have been shown to lower contact resistance and thus improve transport characteristics.[59] This behavior has been shown in the MoS_2 and WSe_2 system, both via conversion with n-BuLi.[59, 161] To our knowledge, however, the on-chip $MoSe_2$ monolayer conversion process has not been explored. Based on theoretical calculations, the $MoSe_2$ 1T' phase should be more energetically accessible than in the canonical MoS_2 system.[167] Combined with the smaller bandgap of $MoSe_2$ (~1.55 eV), $MoSe_2$ is

a promising candidate for on-chip phase engineering. We report the first on-chip 2H to 1T' transformation of monolayer $MoSe_2$ on both SiO_2 and sapphire substrates. Our findings show 1T'-$MoSe_2$ having improved transparency (higher transmission in the visible wavelength range) despite increased number of metallic states, due to lithiation induced changes to the $MoSe_2$ band structure. These property changes indicate the electron donation based optoelectronic tunability of the monolayer transition metal dichalcogenides with potential applications in light harvesting and transparent electrodes. However, in order for n-BuLi 2H/1T' phase engineered contacts to be useful for electronics, the on-chip phase engineering must be robust and stable as well as consistent and reproducible. We find that the n-BuLi is an extremely difficult reagent to control, and have manifest doubts about reliability. We explore these challenges with both experimental measurements and theoretical calculations in the following contribution. We believe this underscores significant and practical challenges associated with n-BuLi-based phase engineering's broader applicability in the 2D electronics field.

5.2. Results and Discussion

Monolayer $MoSe_2$ was grown using a chemical vapor deposition technique on 300 nm SiO_2/Si substrates. Figure 5.1 a, b, and c, shows an as-grown monolayer sheet. Atomic force microscopy (AFM, figure 5.1c confirms the monolayer nature, while scanning electron microscopy (SEM, figure 5.1a and optical microscopy (figure 5.1b show that the sheet is continuous with no obvious defects or cracks. To induce the phase transformation, the monolayer sheets were then exposed to n-BuLi in hexane for 12 hours using standard air-free Schlenk line chemistry techniques. After exposure, SEM (figure 5.1d and AFM (figure

5.1f images show the same flake is intact, though some minor organic debris remain atop the sheet and surrounding area. Figure 5.1e shows that the flake is no longer easily visible in optical microscopy. We conducted the n-BuLi based transformation more than ten times, with consistent transformation shown, but with some instances showing exfoliation of the monolayers from the substrate.

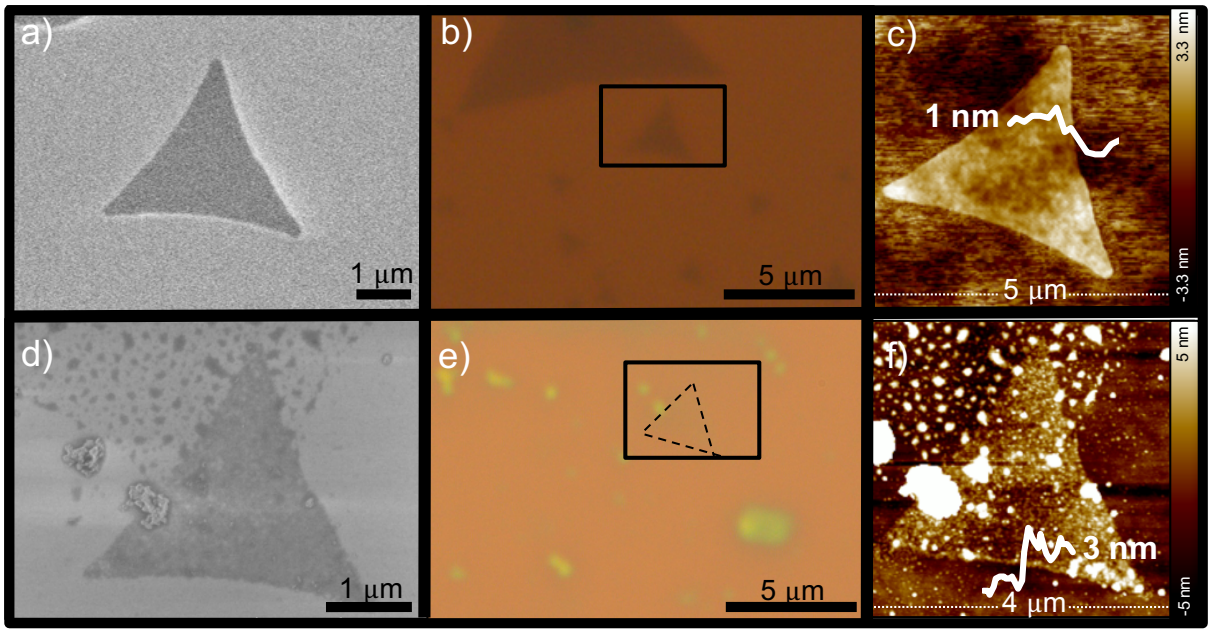

Figure 5.1. a) SEM image, b) optical image, c) AFM image of 2H $MoSe_2$ monolayer on SiO_2/Si substrate, d) SEM image, e) optical image, f) AFM image of the same $MoSe_2$ monolayer on SiO_2/Si substrate after 12-hour n-BuLi exposure leading to 1T' phase conversion.

X-ray photoelectron spectroscopy (XPS) has been shown to reliably measure the 2H to 1T' phase conversion in the TMDs.[64] We employed XPS to investigate the 2H to 1T' conversion in the $MoSe_2$ sheets. Our system was calibrated using the carbon C-C peak (binding energy 284.6 eV). Figure 5.2a shows the Mo 3d spectra of the 2H $MoSe_2$ monolayers. The 2H binding energy peak positions agree with the literature and show no

obvious signs of oxidation.[161, 168] Figure 5.2c shows the Mo 3d spectra after conversion. The XPS peak fitting shows that the monolayer sheets are predominantly the 1T' phase (green fitted peaks), with smaller contributions from the 2H phase (blue fitted peaks) and from the oxidized Mo^{6+} state (grey fitted peaks). Previous reports have shown that the n-BuLi conversion creates an in-plane heterostructure of these quilted phases, but that the transport properties are dominated by the 1T' metallic properties.[169] The same analysis was applied to the Se 3d spectra (figures 5.2b and 5.2d pre and post respectively) with results in strong agreement with the Mo 3d spectra. After n-BuLi exposure, the Se 3d spectra shows a predominately 1T' phase (green fitted peaks) with smaller 2H and oxidized contributions (blue and gray peaks).[168] The survey scans pre (figure 5.7a and post (5.7b n-BuLi exposure are also included in the supporting information for reference, and show the presence of the Si substrate, carbon, and oxygen.

Raman analysis also confirms the 1T' transformation across both SiO_2 and sapphire substrates. On the SiO_2 substrate before conversion (figure 5.3a, the monolayer $MoSe_2$ sheets show the characteristic 2H Raman modes. We observe Raman signatures of the 1T' phase after conversion. In multilayer $MoSe_2$ sheets, we see that a variety of signature 1T' J Raman modes emerge. The J modes are attributed to the $2a_o$ x a_o superlattice structure of the distorted 1T' phase.[170] This includes the J_1 in-plane shearing mode, the J_2 mode which relates to the distance between zig zag chains, and the J_3 mode which represents stretching in the zig zag chain with a small out of plane component.[168, 171] For multilayer $MoSe_2$ on SiO_2, we observe the three J 1T' modes, as well as shifted A_{1g}, E_{1g} and E^1_{2g} peak positions consistent with prior reports on multilayer 1T' $MoSe_2$.[168, 172] We observe that the 1T' conversion largely suppresses the Raman modes of the

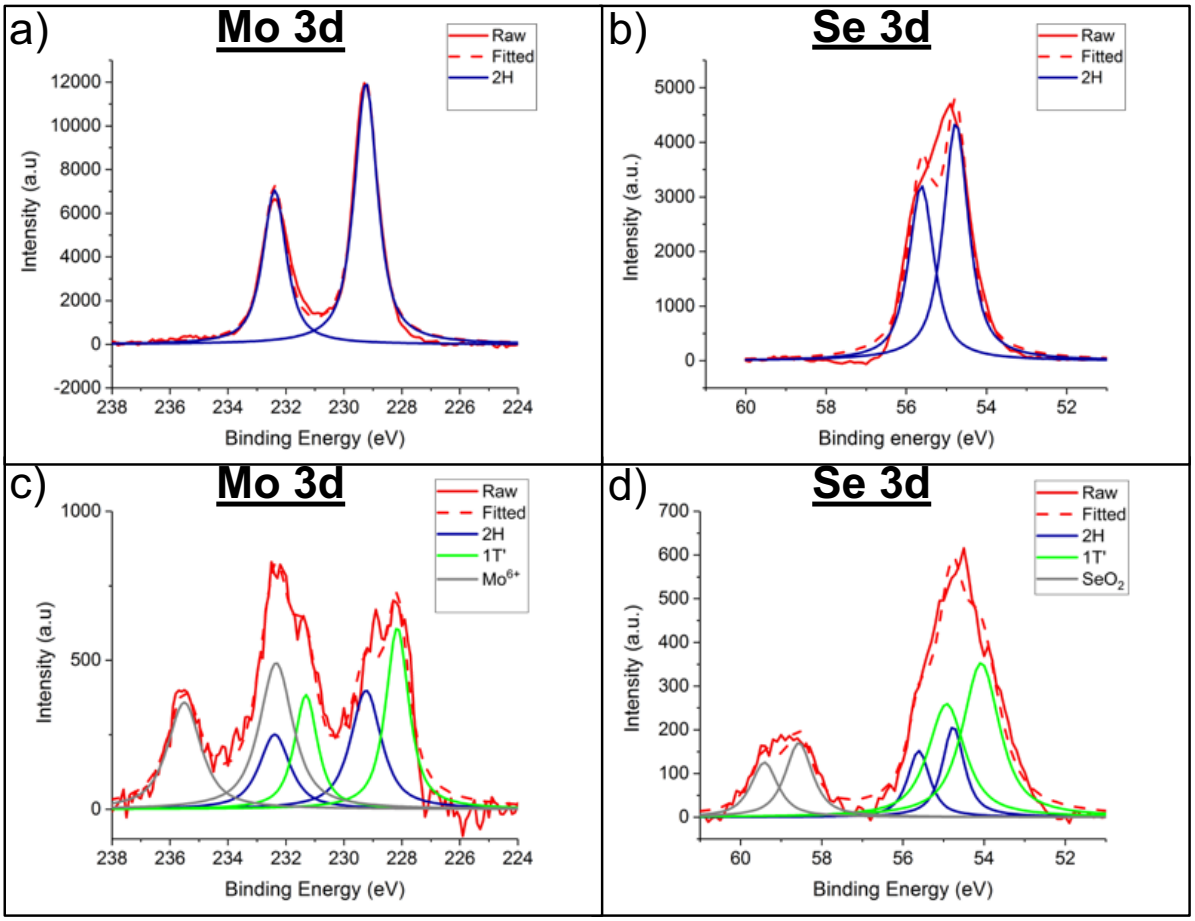

Figure 5.2. XPS characterization of $MoSe_2$ monolayers before and after 1T' conversion. a)Mo 3d spectra and b) Se 3d before n-BuLi exposure. c) Mo 3d, and d) Se 3d after n-BuLi exposure.

monolayer $MoSe_2$ on SiO_2, but still observe the shifted A_{1g} peak and a small J_3 peak.[61] This same Raman analysis was undertaken on $MoSe_2$ grown on sapphire (figure 5.3c. Before conversion, the monolayer 2H $MoSe_2$ on sapphire shows the characteristic A_{1g} and E^1_{2g} modes.[168] After conversion, the multilayer $MoSe_2$ indicates the emergence of the J_1 and J_3 1T' peaks in addition to the A_{1g} peak and broadened E^1_{2g} peaks. After conversion, the monolayer $MoSe_2$ Raman peaks are largely suppressed, but we observe

the shifted A_{1g} peak characteristic of the 1T' phase conversion. 1T' phase conversion is also affirmed by photoluminescence (PL) analysis for both substrates (figures 5.3b and 5.3d. Before conversion, the monolayer 2H $MoSe_2$ shows a bandgap of ~1.52 eV on SiO_2 and ~1.55 eV on sapphire, consistent with literature.[173] After conversion, the monolayer PL is suppressed across both substrates, in accordance with the near-metallic nature of 1T' $MoSe_2$.[167]

We also observe transport ramifications of the 2H to 1T'conversion. Figure S5.8 shows current-voltage curves through the 2H and 1T' films. Due to device fabrication difficulties, measurements were taken with gold probes directly in contact with the multilayer films (high contact resistance). Despite poor Schottky contacts and high contact resistance lowering the overall current densities, we still observe a two order of magnitude higher drain current for the 1T' film vs. the 2H at equivalent source-drain gate voltage, indicating increased carrier density as a function of lithium intercalation and 1T' band structure changes. Transmission and reflection measurements were conducted on both SiO_2 and sapphire substrates. Transmission spectra were taken of $MoSe_2$ grown on sapphire both before and after 1T' conversion (figure 5.4a. The 2H monolayer $MoSe_2$ (in red) shows absorption peaks corresponding to the A exciton (~810 nm) and B exciton (~708 nm).[174] For the 1T' phase, these peaks disappear, in line with the near metallic band structure.[156] The 1T' monolayers also have greater optical transparency (higher transmission in the visible wavelength range) than the 2H phase. The 2H monolayer TMDs have anomalously high absorption, due to band nesting and Van Hove singularities in the density of states leading to a high optical conductivity and absorption.[175] DFT calculations on the related MoS_2 system have shown that lithium intercalation disrupts these

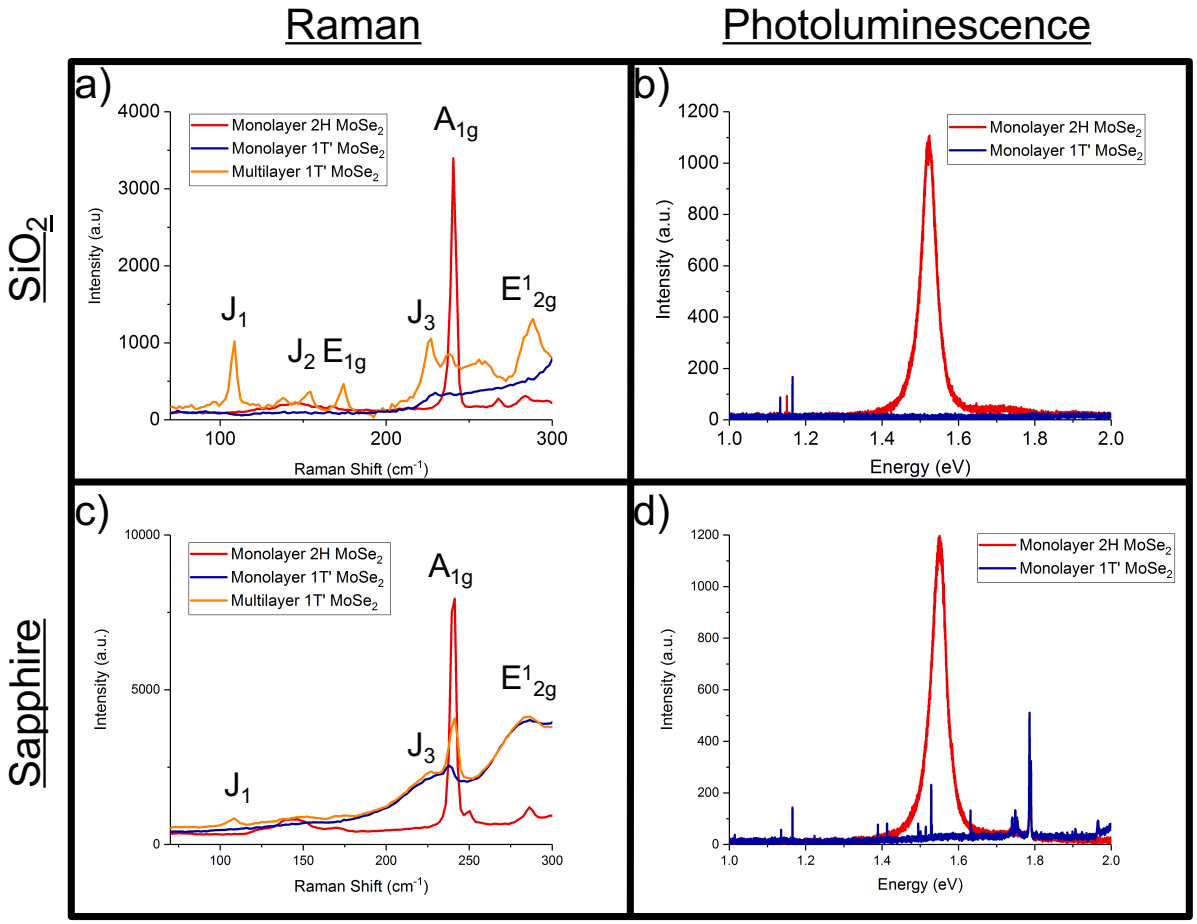

Figure 5.3. Raman and PL analysis of n-BuLi 1T' $MoSe_2$ conversion on both SiO_2 and sapphire substrates. a) shows the Raman signatures of a representative monolayer 2H sample before transformation, the resultant monolayer 1T' sample after transformation, and a representative 1T' multilayer sample after transformation, all on an SiO_2 substrate. b) shows the PL of a representative monolayer $MoSe_2$ sample before and after the 1T' transformation on SiO_2. c) shows the Raman signatures of a representative monolayer 2H sample on sapphire before and after 1T' transformation, as well as a multilayer $MoSe_2$ sample on sapphire after 1T' transformation. d) shows the PL of a representative $MoSe_2$ monolayer on sapphire before and after 1T' transformation.

features; accordingly, the absorption is lower in the lithium-intercalated 1T' phase.[176]

Reflection measurements were taken on $MoSe_2$ sheets of the 2H and 1T' phases. Figure

5.4b shows the reflection spectra normalized by the reference SiO_2 substrate. In alignment with the optical images in figure 5.1, the reflection spectra show that the 1T' reflection is very similar to the SiO_2 substrate reflection profile, while the 2H phase shows a distinct reflection profile. This is a numerical representation of the reduced optical contrast of the monolayer sheet on the 300 nm SiO_2/Si substrate. Based on analysis using Fresnel's law (see Supporting Information for details) we surmise that the changing reflection optical contrast is a function of a change in the complex refractive index with the 1T' conversion.[112] All of these results show that interesting optical and electrical property changes result from the 2H to 1T' phase conversion.

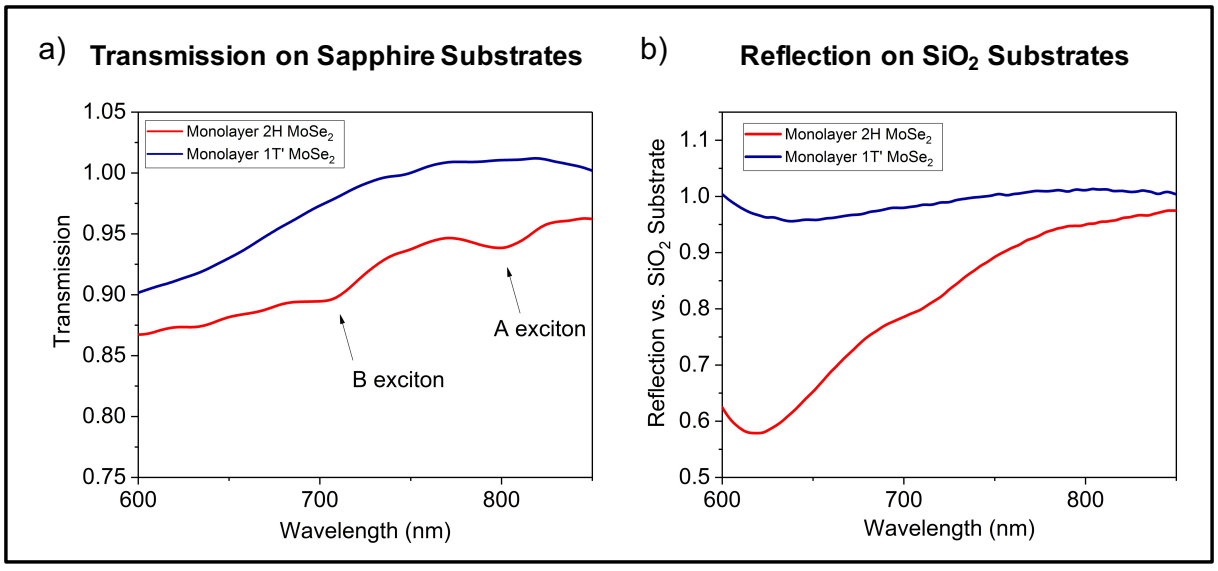

Figure 5.4. Transmission and reflection characterization of the $MoSe_2$ 2H and 1T' phases. a) shows the transmission spectra of $MoSe_2$ monolayers on sapphire substrates before and after transformation while b) shows the reflection spectra of $MoSe_2$ monolayers on SiO_2 substrates normalized to the SiO_2 spectra before and after transformation. The 1T' monolayer $MoSe_2$ exhibits higher transparency than the 2H phase. Similarly, the 1T' monolayer shows lower reflection compared to the SiO_2 substrate than the 2H phase, indicating a refractive index change with phase transformation.

However, there are underlying practical difficulties to patterning the monolayer 1T' phase. We have investigated the theoretical and experimental challenges of the n-BuLi phase conversion via a number of techniques. Figure 5.5 shows DFT calculations of the various energetics incurred by lithium association with the $MoSe_2$ sheet. We consider three conditions: a) no lithium present, b) lithium absorbed on one side of the sheet, and c) lithium absorbed on both sides of the sheet. The 2H phase energy was set as the zero point, and the relative energies of the 1T and 1T' forms are presented. Based on the recent literature, we consider that the 2H phase goes through a 1T phase intermediate in order to transform to the 1T' phase.[177, 178] Across all three cases we see that the distorted 1T' octahedral phase is more energetically favorable than the 1T octahedral phase. With no lithium present (case a), the 2H phase is the most thermodynamically stable, consistent with prior literature and calculations.[161, 167] With lithium only on the top side of the sheet (case b), we calculate that there is no energetic benefit to conversion to the 1T phase intermediate. As a result, there should be little conversion to the 1T phase, and little, and extremely slow conversion to the 1T'. It is only when lithium is present on both sides of the monolayer (case c), that there is a strong thermodynamic driving force to drive the conversion to the 1T phase, and 1T' phase as a result. In case c, the 1T phase is lower in energy than the 2H phase by 0.54 eV, indicating ready conversion. As the 1T' phase is 0.2 eV lower in energy than the 1T phase, there is a driving force for the 1T phase to convert to the 1T' phase. This suggests that lithium should intercalate to both sides of the monolayer, in this case between the monolayer and the substrate, in order for measurable conversion to occur. This helps explain the long reaction time required for the conversion (12 hours), as well as the instability of

the converted sheets. We observe that the monolayer sheets are often exfoliated off the substrate. Across monolayer lithiated sheets, we also observe a height increase of almost 2 nm (shown in Figure 5.1), indicative of lithium intercalation and possible decoupling from the substrate. Altogether, this evidence suggests that lithium intercalates under the monolayer sheet.

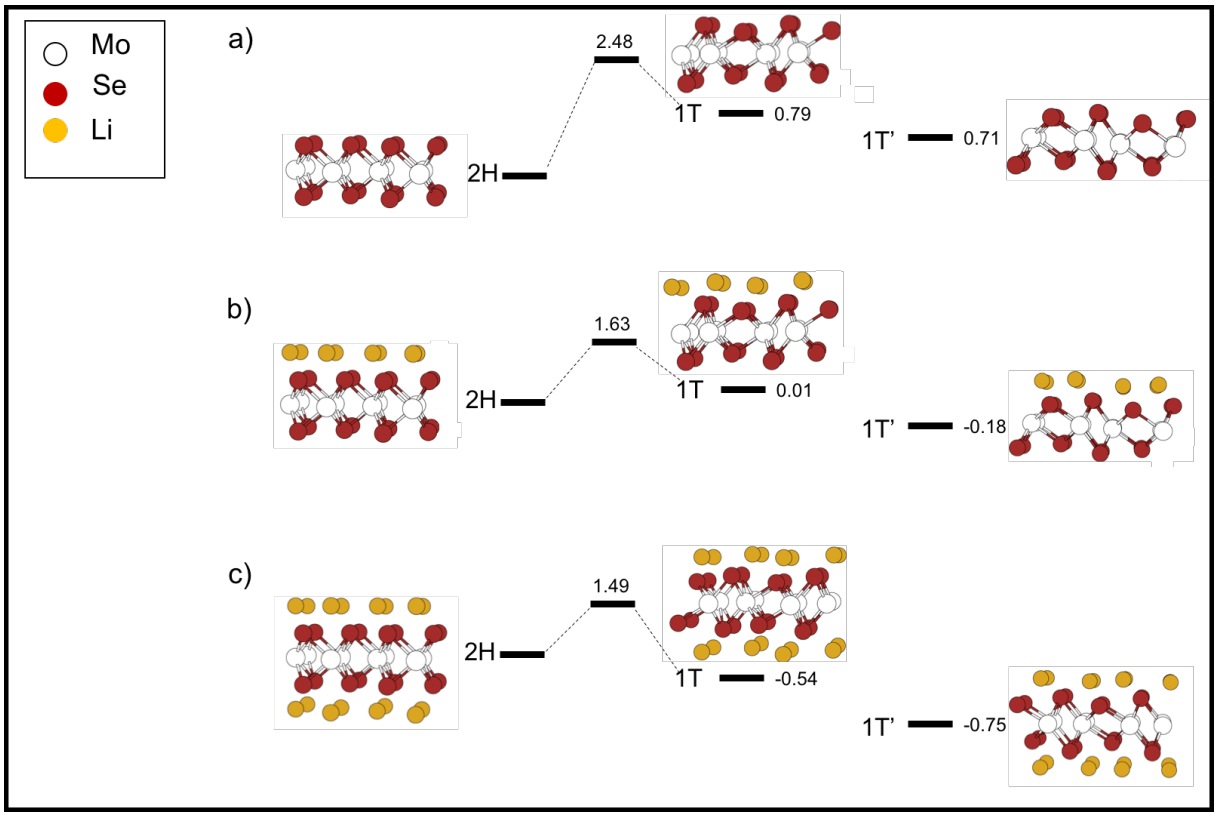

Figure 5.5. DFT calculations of Li configurations on the $MoSe_2$ monolayer showing lithium intercalation-based changes in the thermodynamic driving force for 1T' transformation. Calculations show the energy differences between the 2H phase, the configuration transition phase, the 1T phase and the 1T' phase. a) Shows the case with no additional lithium (energies in eV/supercell) b) shows the case with lithium coordinated on top of the monolayer (energies in eV/Li) while c) shows the case with lithium on both sides of the monolayer (energies in eV/Li). Case c) shows a strong thermodynamic driving force for transformation to the 1T' phase.

Previous reports have touted the ability to controllably pattern n-BuLi-based 1T' transformations; our theoretical and experimental results indicate that, while possible, this approach is unreliable. Similar to previous reports, we used a PMMA mask to selectively expose regions of the $MoSe_2$ sheet to the n-BuLi solution.[59, 61] Experimentally, the kinetics of the patterned exposed regions differ from bulk substrate exposure. When using the same 12 hour protocol that was necessary to incur full transformation on monolayer $MoSe_2$ films, we observed that patterned exposed regions were destroyed. Figure 5.6a shows a SEM image of one such area after a 12 hour exposure protocol. Inside the exposed trench (denoted by red lines) the monolayer flakes are no longer intact. Figure 5.6b shows a patterned region after a 4 hour exposure protocol. Even with a short 4 hour exposure, we observe that large exposed regions are destroyed, as confirmed by SEM. Figure 5.6c shows a large area monolayer that was patterned with dots and received a 4-hour n-BuLi treatment. We compare a larger dot (figure 5.6d, blue square) with a smaller dot (figure 5.6e, green square). Figure 5.6d and 5.6e show triangular shapes; these are nuclei forming of a second layer. Based on inspection of the secondary electron image contrast (figure 5.6e, it appears that the smaller exposed areas are intact while the larger dot area (figure 5.6d is destroyed. These varying results within a single monolayer sheet indicate inhomogeneity in the transformation kinetics. We observed inhomogeneity across four patterning attempts. We hypothesize these differences are due to the fluid dynamic-induced inhomogeneity in local concentration gradients of the n-BuLi solution, as local concentration differences would lead to differing transformation kinetics and resulting transformation times. Further experiments would be required to prove this concretely. Together, these

results point to significant challenges to using patterned exposure of n-BuLi to create patterned devices for electronics, particularly at scale.

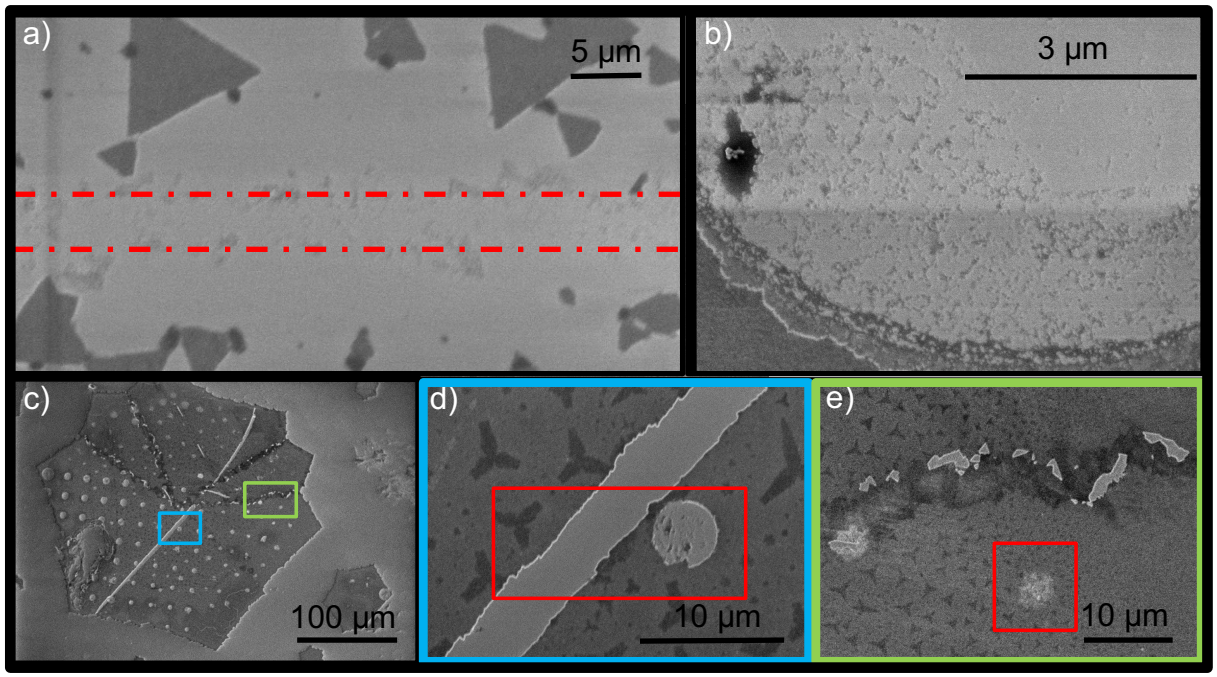

Figure 5.6. SEM images of n-BuLi patterning of $MoSe_2$. a) shows a trench that was exposed to a 12 hour n-BuLi treatment. All of the $MoSe_2$ monolayers inside the trench (trench denoted by red dotted lines) were destroyed. b) shows a circle that was exposed to a 4 hour n-BuLi treatment. Even with just a 4 hour treatment, the exposed area was destroyed. c) shows a large area monolayer film that was patterned with dots; dots were preferentially exposed to a 4 hour n-BuLi treatment. d) shows the region highlighted in blue while e) shows the region highlighted in green. In d) the hole shows tearing while in e) the exposed area appears intact based on the secondary electron contrast.

Across the experimental and theoretical results, we observe that while monolayer on-chip 2H to 1T' conversion is possible in the $MoSe_2$ system and presents promising optoelectronic properties, the high reactivity and changing concentration gradients of n-BuLi present challenges to reliability. DFT and experimental results indicate inherent

challenges to monolayer stability, due to the intercalation of lithium between the monolayer and the substrate. Finally, the metastable nature of the 1T' phase suggests that phase-engineered 1T' devices would be short-lived, even in protected environments.

Recent reports have touted phase engineering 1T' phase contacts as a promising avenue for lowering contact resistance for TMD-based integrated circuits. However, this approach has not been shown for monolayer $MoSe_2$, and too little attention has been paid to the challenges facing the reliability and reproducibility of this approach. We address both of these deficiencies in the literature. First, we show the successful on-chip transformation of 2H $MoSe_2$ to 1T' $MoSe_2$ via n-BuLi exposure. The transformation is confirmed via XPS, Raman, transport and PL analysis. The transformation is shown on both SiO_2 and sapphire substrates. We also highlight resultant 1T' transformation-driven optical properties changes. The 1T' phase shows higher transparency in the transmission spectra, indicating band structure changes with lithium intercalation. The 1T' phase also shows reflection spectra more like that of the 300 nm SiO_2/Si substrate than the 2H phase, indicating a complex refractive index change. However, there are challenges to harnessing these promising optical properties. DFT calculations suggest that Li^+ should diffuse to both sides of the $MoSe_2$ monolayer to induce a strong thermodynamic driving force for the 1T' phase transition. This helps explain the long transformation time required, low stability, and low yield of the on-chip 1T' monolayer transformation. There are additional challenges to n-BuLi-based phase engineering; we observe inconsistent patterning results due to inhomogeneous kinetics of the n-BuLi reaction, even within a single monolayer sheet. Further, the 1T' phase is inherently metastable, and should transform back to the 2H phase over time. These characteristics together challenge the vision of a wafer-scale

patterned 2H/1T' TMD-based integrated circuit. As a result, further investigations of the $MoSe_2$ 1T' phase should focus on its intriguing physical properties. Our results indicate the 2D community should approach using n-BuLi-induced 1T' phase transformations for TMD contact resistance reduction with caution, and that other strategies to reduce TMD contact resistance may be more fruitful. It also suggests that researchers should explore other doping techniques, such as the charge transfer investigations described in the following chapter.

5.3. Methods and Supporting Information

5.3.1. Methods

CVD growth: MoO_3 powder (< 1 mg) is spread onto a substrate and placed in the center of a 1" tube furnace. A small amount of the seeding molecule perylene-3,4,9,10-tetracarboxylic acid tetra potassium salt (PTAS) was applied to the substrate and dried at 50 C on a hot plate. It was found that the seed molecule reservoir was needed to achieve $MoSe_2$ growth. A larger substrate was then suspended 2 mm above the first substrate; the suspended substrate serves as the primary deposition substrate. An alumina boat filled with 500 mg of Se powder was placed ~3 in upstream from the hot center substrate. 190 sccm of high-purity argon served as a carrier gas, with the introduction of H_2 during growth to aid the reduction process. The time-temperature profile was as follows: 20 C to 800 C over 18 min, turn on the 5 sccm of H_2 at 675 C to start the reduction process, hold growth at 800 C for 15 min, turn off H_2, cool naturally to room temperature. The furnace was left to cool overnight, and purged with higher flows of argon, to ensure that no H_2Se (an extremely toxic gas) remained in the system.

n-butyllithium conversion: $MoSe_2$ on SiO_2 or sapphire substrates were exposed to n-BuLi to cause the 2H to 1T' conversion using standard air-free Schlenk line techniques to ensure that no water or air was introduced. The chips were exposed to 1.6 M n-BuLi hexane solution for 12 hours under an argon atmosphere at room temperature. After 12 hours the n-BuLi was cannulated into a quench solution of 1:1 isopropanol (IPA)/hexane at 0 C. While maintaining an argon atmosphere, each substrate was rinsed 3 times with hexane, exposed to air and rinsed further with IPA to remove any salts. Each substrate was then dried under a stream of argon and returned to an inert atmosphere.

Raman and PL analysis: Raman and photoluminescence spectra were taken on Horiba LabRAM HR Evolution (at room temperature). Raman spectra were taken with a 532 nm excitation laser with a max power of 50 mW, with neutral density filters at 1% (1 min x 4). PL spectra were taken with a 532 nm excitation laser with an acquisition time of 1s and neutral density filters at 1%.

XPS: Spectra were obtained with monochromated Al K-alpha radiation with a 500 μm aperture at room temperature. For Mo spectra, $3d_{5/2}$ and $3d_{3/2}$ doublets were constrained to the same FWHM, the $3d_{3/2}$ energy was constrained to 3.15 eV higher than the $3d_{5/2}$ peak, and to the 63% area ratio. For Se spectra, the $3d_{3/2}$ energy was constrained to 0.85 eV higher than the $3d_{5/2}$ peak, to a 73.5% area ratio, and to the same FWHM.

Transmission and reflection measurements: The transmission and reflection measurements were made using a broadband halogen light source coupled through a Nikon inverted microscope at room temperature. In transmission mode, the incident light is shined on the backside of the sample using a 1x objective and collected from the front side of the sample using a 100x objective with NA=0.9. In reflection mode, both transmission and

reflected light travel through the 100x objective. Collected light is then spatially filtered through a physical slit and CCD binning on an Andor 303mm focal length spectrometer with an Andor Newton electron multiplication charge-coupled device (EM-CCD) detector.

Density Functional Theory Calculations: We use density functional theory within the generalized gradient approximation, periodic boundary conditions, and plane wave basis set as implemented in the Viennaab initiosimulation package to obtain the relaxed atomic geometries of the systems and their total energies.[179–181] All the calculations are based on a monolayer slab of $MoSe_2$ with 15 A of vacuum as the spacing layer between the slab and its periodic image. Projector augmented wave potentials have been used for each species, where the 4p states of Mo and the 1s states of Li are treated as valence states.[182, 183] To simplify the calculations, we consider the full coverage of Li on the top site of Mo atoms in the 1x1 conventional cell of $MoSe_2$containing 6 atoms. The nudged elastic band method is applied for finding the energy barriers of configuration transition from 2H to 1T.[184] All the atomic positions are relaxed until the forces exerted on the active atoms are less than 0.05 eV/A.

Fresnel's Law Analysis: Using Fresnel law, optical contrast can be defined as:

$$\text{Optical contrast} = (\mathrm{I_{flake}} - \mathrm{I_{substrate}})/(\mathrm{I_{flake}} + \mathrm{I_{substrate}})$$

where I represents the reflected intensity. In line with reference [112]

$$\mathrm{I} = [\mathrm{r_{01}e^{i(\Phi_1+\Phi_2)}} + \mathrm{r_{12}e^{-i(\Phi_1-\Phi_2)}} + \mathrm{r_{23}e^{-i(\Phi_1+\Phi_2)}} + \frac{\mathrm{r_{01}r_{12}r_{23}e^{i(\Phi_1-\Phi_2)^2}}}{\mathrm{e^{i(\Phi_1+\Phi_2)}}} + \mathrm{r_{01}r_{12}e^{-i(\Phi_1-\Phi_2)}} + \mathrm{r_{01}r_{23}e^{-i(\Phi_1+\Phi_2)}} + \mathrm{r_{12}r_{23}e^{-i(\Phi_1-\Phi_2)}}]^2$$

$$r_{ij} = (n_i - nj)/(n_i + n_j)$$

$$\Phi_i = 2\pi n_i d_i/\lambda$$

With subindices 0, 1, 2, and 3 referring to air, monolayer, SiO_2, and Si respectively. n_i is the complex refractive index, d_i is the thickness of the medium i, λ is the wavelength, and r_{ij} and Φ_i do not have direct physical interpretations.[112]

With the 2H to 1T' conversion, the refractive indices for air and substrate remain constant, leaving the only independent variable the $MoSe_2$ monolayer refractive index. As a result, we surmise that the changing reflection optical contrast is a function of a change in the complex refractive index with the 1T' conversion.

5.3.2. Supporting Figures

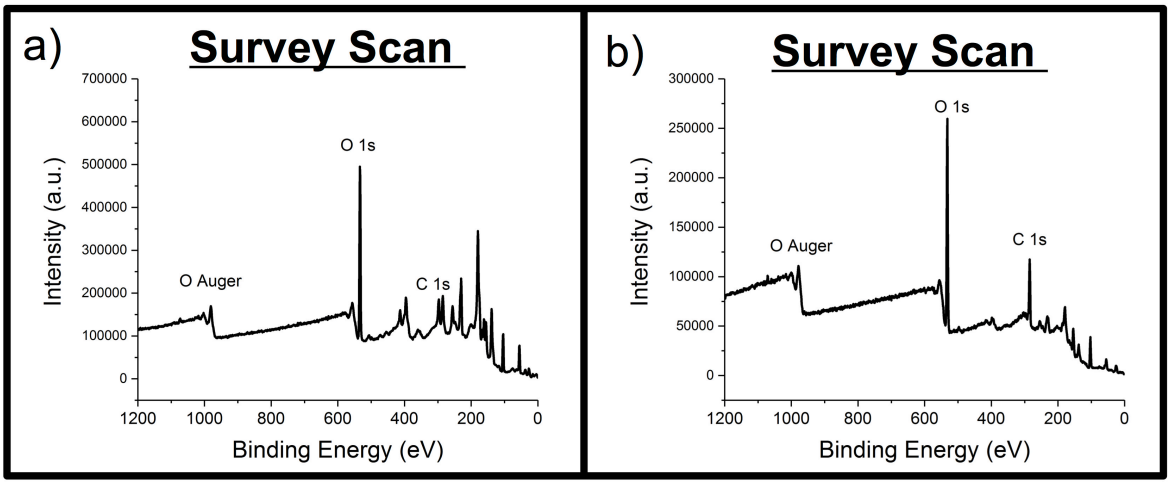

Figure 5.7. XPS survey scans of $MoSe_2$ monolayers before and after 1T' conversion. a) Survey scan before and b) survey scan after n-BuLi exposure, corresponding to XPS data presented in figure 5.2.

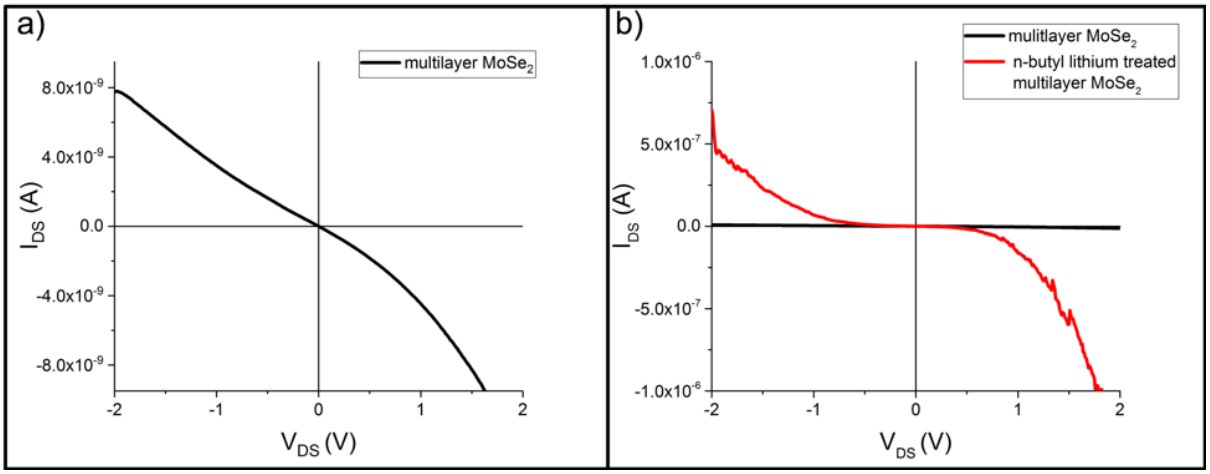

Figure 5.8. Current-voltage characterization of 2H and 1T' $MoSe_2$ films. a) shows the current-voltage behavior of multilayer 2H $MoSe_2$ before transformation, while b) shows the current-voltage behavior of multilayer films both before and after transformation.

CHAPTER 6

Property engineering: p-type MoS_2 via charge transfer doping

This chapter is based on work by Eve D. Hanson, Jingshan Du, Teodor Stanev, Akshay Murthy, Laura M. Lilley, Yuan Li, Fernando Castro, Thomas J. Meade, Nathaniel Stern, Chad Mirkin, and Vinayak P. Dravid.

This chapter explores the promising avenue of charge transfer doping as a technique to exert property control over the monolayer TMD systems.

6.1. Introduction and Motivation

Integration of the two-dimensional transition metal dichalcogenides into more complex electronics has been hindered by the lack of reliable doping techniques. Molybdenum disulfide, the extensively studied 2D TMD, is challenging to p-type dope. MoS_2 is intrinsically an n-type material. In addition, sulfur vacancies serve as electron donors to surrounding Mo atoms.[185] The common practice of using elemental materials as contacts further enhances this n-type behavior, due to Fermi level pinning at the metal-semiconductor interface limiting the ability to hole-dope the material via gating techniques.[73, 185–188] Traditional doping approaches are challenging to apply to a fundamental monolayer, as there are fewer available dopant sites without disrupting the lattice. A few recent approaches have shown progress in forming MoS_2 p-type field effect transistors (PFETs), but with significant limitations. For example, MoS_2 has been doped with Nb, but this requires mechanical exfoliation, is not well controllable, and shows high off currents.[55] Thin-film

MoO_x has been used as a high work function contact and hole dopant, but required high-vacuum deposition conditions and was only shown with near-bulk MoS_2 samples.[23] In contrast, chemical doping is a promising approach for doping low-dimensional materials, and only recently has received attention for the transition metal dichalcogenides.[189, 190] Monolayer materials are all surface, thus susceptible to charge transfer surface doping techniques. Recent reports have shown highly controllable, high-performance PFET devices utilizing the p-type charge transfer dopant $AuCl_3$.[71–73]

$AuCl_3$ has previously been used to create Au nanoparticles on the surface of MoS_2 in aqueous suspensions in order to create composite structures with synergistic functional properties. Zou et al. show the composite structures can be used for sensing of a variety of biologically-relevant chemicals (dopamine, ascorbic acid, uric acid), Kim et al. show that the composite structures have enhanced electrocatalytic activity, and Su et al. report enhanced surface enhanced Raman scattering (SERS) activity.[191–193]

Recent reports have focused on electronic property changes. Liu et al. reported a CMOS inverter comprised of the intrinsic MoS_2 n-type field effect transistor (NFET) combined with a $AuCl_3$-doped multilayer PFET, as well as precise tunability of the p-type doping level, tunable by both the $AuCl_3$ concentration and annealing time.[73] Li et al. show an ultra-thin MoS_2 p-n junction utilizing the $AuCl_3$ p-type dopant.[72] However, across all of these exciting reports of multilayer MoS_2 systems, the chemical, structural, and oxidation state changes incurred by the $AuCl_3$ p-type doping process are not well understood, particularly at the surface. Most reports have represented the doping process as a black box, yet there are complex structural and chemical changes at play.

In this chapter, we provide a detailed study of the structural and chemical changes that accompany the $AuCl_3$ redox reaction-based MoS_2 p-type doping at the all-surface, monolayer limit. We provide a proposed coordination geometry of the Au^{3+} and detailed structural information about the resultant gold nanoparticle (Au NP) formation across a variety of characterization techniques. We show XPS and transport data to confirm the p-type doping process. Low-temperature photoluminescence (low-T PL) measurements give insight into the unique light-matter interactions of this system. Our low-T PL measurements provide optical evidence of the p-type doping process at the monolayer limit.

MoS_2 electronics have also been hindered by the lack of controlled doping and sensitization. Precise patterning is required to make devices at scale. We present a new patterning technique to control the $AuCl_3$ deposition. We utilize polymer pen lithography (PPL), a facile, direct patterning technique to pattern the $AuCl_3$ p-type doping treatment. PPL is a low-cost, high-throughput scanning probe patterning technique that uses an array of soft elastomeric tips to directly write chemical inks onto the surface of a substrate.[194] We utilize $AuCl_3$ dissolved in nitromethane as a chemical ink to directly write the redox reaction onto the MoS_2 monolayer surface. We show structural and chemical characterization of the patterned dopant, to highlight both the Au nanoparticle and Au^{3+} ion transfer. This patterning could potentially be used to make p-n junctions at scale as well as to functionalize MoS_2 with a variety of chemical treatments. We highlight the wide applicability of the PPL approach to the 2D community.

6.2. Results and Discussion

Figure 6.1 shows a schematic of the monolayer MoS_2-$AuCl_3$ redox reaction. $AuCl_3$ is a strong oxidizing agent, and has been used as a p-type dopant with both graphene and carbon nanotubes.[68–70] $AuCl_3$ is a good candidate for charge transfer doping MoS_2, due to the strong affinity between the Au^{3+} ion and the terminating sulfur on the monolayer MoS_2. In line with the analysis by Kim et al., $AuCl_3$ has a strong reduction potential relative to MoS_2.[192] The potential of $AuCl_4^-$ is 1 V vs. the standard hydrogen electrode (4.5 eV work function) giving an implied work function of ~5.5 eV, compared to the 5.2 eV fermi level of monolayer MoS_2. This energy difference provides an electrochemical driving force for the redox reaction and p-type doping.[192, 195–197]

The overall reaction is a reduction-oxidation reaction, where the Au^{3+} ion in solution is reduced to form Au^0 nanoparticles (NPs) on the MoS_2 surface, and the MoS_2 layer is oxidized (electrons removed) to form a positively charged MoS_2 layer. Dissolved in nitromethane (CH_3NO_2), $AuCl_3$ disproportionates to form a square planar [$AuCl_4^-$] (Au^{3+}) complex and [$AuCl_2$–] (Au^{1+}), due to the weak ligand donor properties of CH_3NO_2.[198] Au^{3+} is a highly reactive, 16 e^- system that undergoes associative reaction mechanisms where the intermediate is a 5-coordinate species, particularly with sulfur donor atoms.[199, 200]

Based on the literature, we propose a Au^{3+} center coordinates with a sulfur atom on the surface of the MoS_2 and subsequently undergoes ligand dissociation and reduction to Au^0, nucleating Au NP formation. Figure 6.1 shows this associative reaction mechanism, [$AuCl_4^-$] associates with a sulfur atom on the MoS_2 surface serving as a fifth ligand, generating a reactive intermediate. A redox process then occurs at the surface reducing

the Au^{3+} to a Au^0 center, leaving the MoS_2 positively charged and nucleating Au^0 NP formation. Previous study on $AuCl_3$-S systems have suggested a chloride bridged electron transfer.[201]

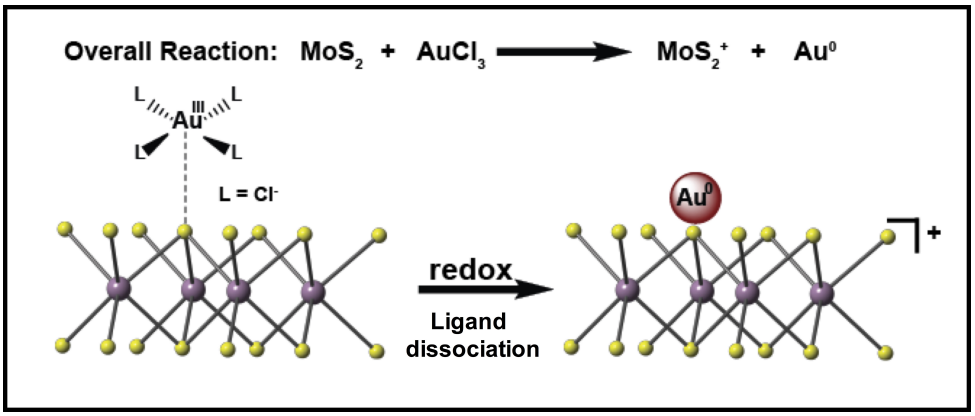

Figure 6.1. Proposed Au NP nucleation mechanism on MoS_2 surface. $AuCl_3$ dissolved in anhydrous CH_3NO_2 undergoes ligand dissociation and reduction on the MoS_2 surface nucleating Au NP formation. MoS_2 structure where the Mo and S are represented by purple and yellow spheres, respectively.

6.2.1. Chemical, structural, and optical changes with $AuCl_3$ treatment

$AuCl_3$ serves as a strong redox agent that induces p-type doping in the MoS_2 monolayer and complex structural and chemical changes. Figure 6.2 shows the characterization of MoS_2 monolayers after 5 mM $AuCl_3$ treatment. In accordance with previous reports, the monolayers were spincoated with a 5 mM $AuCl_3$ solution in nitromethane. More details are given in the methods section. Figure 6.2a shows a transmission electron micrograph of a monolayer MoS_2 film with Au NPs on the surface. Based on our TEM analysis, we observe that the $AuCl_3$ treatment leads to a distribution of Au NPs from ~10 nm to ~150 nm in size. Figure 6.2b shows a higher magnification TEM image. The film is dotted with

smaller Au NP (~10 nm). There is additional strain contrast and PMMA residue. Figure 6.2c shows a higher magnification image of one of the larger Au NPs. We observe that the particle shows dendritic-like features, indicating anisotropic Au NP growth that produces polycrystalline NPs. Figure 6.7 shows the diffraction patterns of the MoS_2 film before and after $AuCl_3$ treatment. Before $AuCl_3$ treatment, the native MoS_2 diffraction can be indexed to the hexagonal MoS_2 symmetry along the [001] and P63/mmc space group. After treatment, the diffraction pattern can be indexed to both the MoS_2 monolayer and the Au (111), (200), and (220) planes. Figure 6.2c and 6.2d show a different monolayer with the $AuCl_3$ spincoat treatment. The SEM and AFM images indicate that there are generally larger nanoparticles on the scale of ~50 nm, surrounded by smaller Au NPs on the order of ~10 nm. Given the random nature of a spincoating process, there is variation in the nanoparticle size from sample to sample. The underlying MoS_2 does not show any obvious cracks, pits, or signs of damage. Together, these results show that the 5 mM $AuCl_3$ treatment can be safely applied without damaging the MoS_2 monolayer and that the redox reaction produces a distribution of Au NP sizes. High-resolution TEM studies could be further undertaken to explore possible defects introduced by the $AuCl_3$ treatment.

XPS analysis and transport measurements can be used to probe the p-type doping process. Figure 6.3a shows a gate-sweep transport characterization of the same MoS_2 monolayer device before and after $AuCl_3$ treatment. We observe a majority n-type to majority p-type transport change as a function of 5 mM $AuCl_3$ treatment. This is indicated by the change in source-drain current behavior with applied gate; before treatment positive gate bias leads to a large increase in I_{DS} due to increasing carrier concentration in

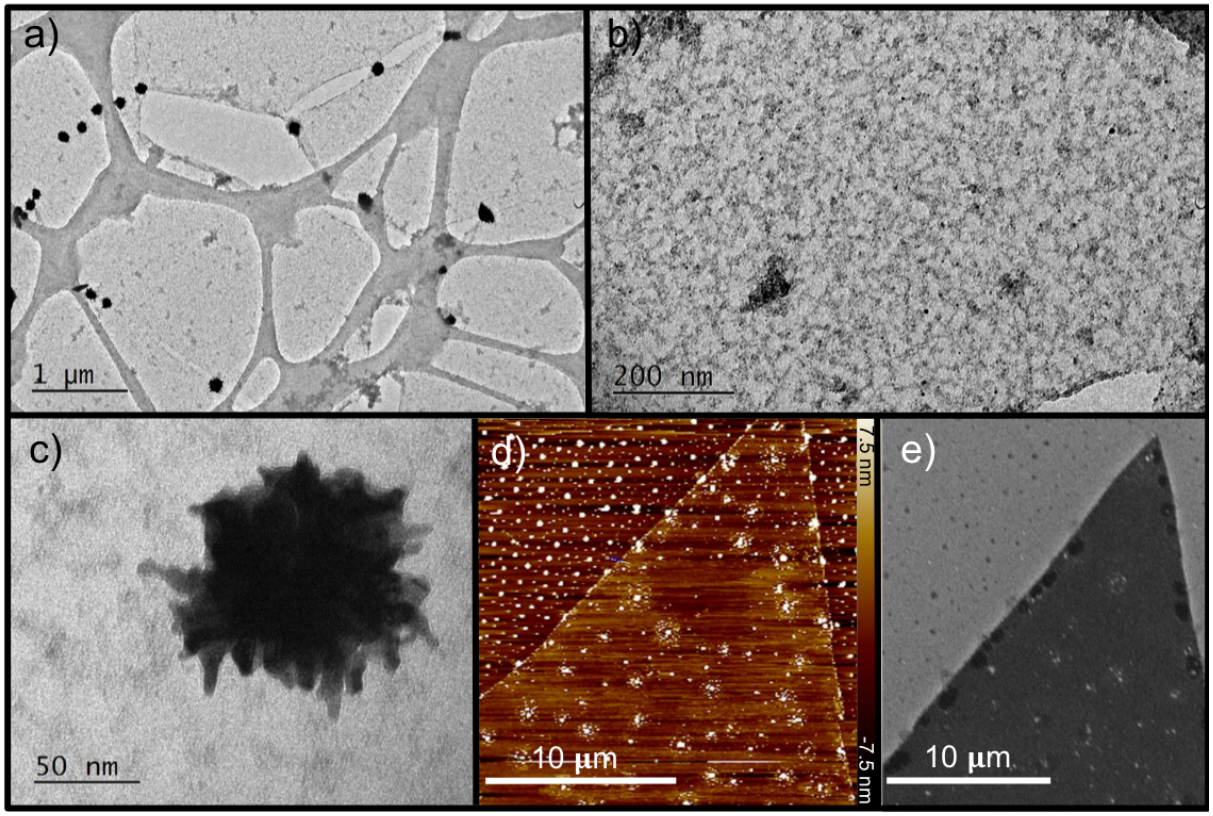

Figure 6.2. Characterization of MoS_2 monolayers after $AuCl_3$ treatment. a) shows a TEM micrograph of a MoS_2 monolayer on a lacey carbon TEM grid that has been treated with 5 mM $AuCl_3$ solution. 100 nm Au NPs dot the surface. b) shows the same monolayer at higher magnification. In addition to the 100 nm Au particles, small 10 nm particles dot the surface. c) shows a higher magnification image of a 100 nm Au nanoparticle. The particle shows dendritic features. d) shows the AFM image of a MoS_2 monolayer treated with 5 mM $AuCl_3$ solution. The monolayer remains flat, and is dotted with large 50 nm NPs surrounded by smaller 10 nm NPs. e) shows the same monolayer in SEM. The SEM micrograph shows the continuous MoS_2 monolayer and Au NP formation.

an n-type semiconductor, while after treatment negative gate bias leads to increasing I_{DS} due to increasing carrier concentration in a p-type semiconductor. I_{DS} is plotted on a log scale. We also used XPS to measure the p-type doping effect on the chemical constituents. Previous reports have indicated that p-type doping of MoS_2 should lead to a shift to lower binding energy for both the Mo and S constituents.[55, 202] This is because with p-type doping, the Fermi level shifts to lower energy. The XPS core-level binding energies are referenced to the Fermi energy; as such, a lower Fermi energy will lead to a downward shift of the relevant core level energies. We observe a consistent downward shift of the Mo 3d and S 2p binding energies with increasing $AuCl_3$ treatment, as shown in Figure 6.3a and 6.3b. We observe a consistent downward shift of 0.2 eV for 5 mM $AuCl_3$ treatment and 0.4 eV for the 20 mM $AuCl_3$ treatment. The carbon calibration spectra are included in the supporting information for reference (Figure 6.8). A previous report of Nb-based degenerate p-type doping corresponds to a downward shift of 0.7 eV.[55] Our smaller observed shifts align with our transport that indicates non-degenerate p-type doping for the 5 mM $AuCl_3$ treatment with 5 min anneal.[73] These results show the successful, non-degenerate p-type doping of monolayer MoS_2 with 5 mM $AuCl_3$ treatment.

Figure 6.9a-c shows the same Mo 3d data fit with the constituent peaks. We observe that there is a small oxidized component (Mo^{3+}) before exposure, as well as after the 5 mM exposure. the 20 mM exposure leads to a higher Mo^{3+} oxidized contribution, suggesting that the redox reaction can lead to over-oxidation with too high of concentration. Figure 6.9 shows the Au 4f spectra before and after the different $AuCl_3$ exposures. As expected, the native MoS_2 does not show Au signal. After the 5 mM spincoating treatment, we observe Au 4f contributions from the Au^0 binding energy, showing that the full

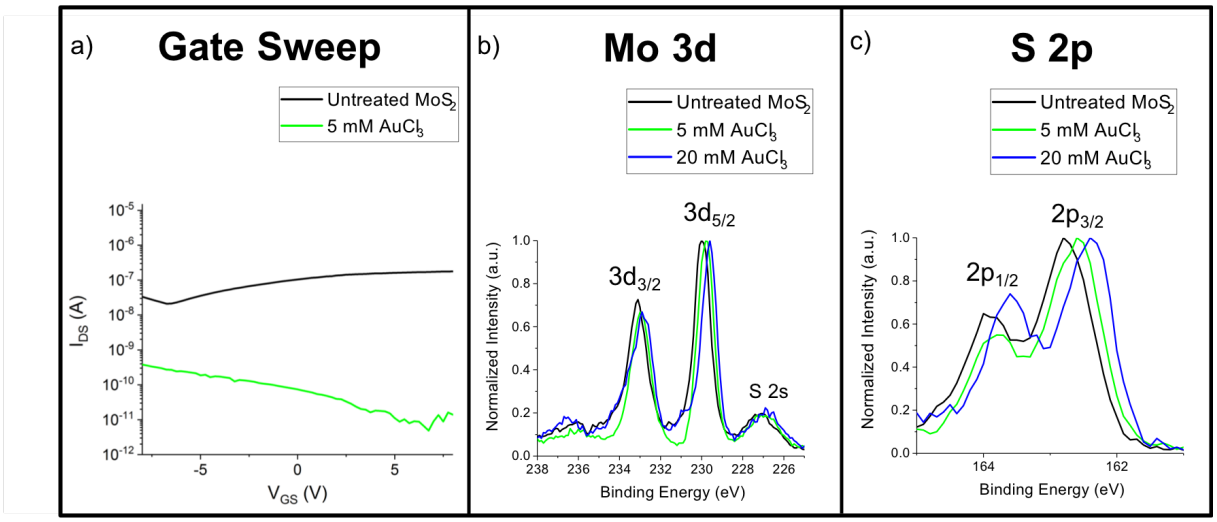

Figure 6.3. Transport and XPS analysis of $AuCl_3$ p-type doping treatment. a) Gate-sweep measurements of MoS_2 monolayer device before and after $AuCl_3$ treatment. b) Mo 3d spectra before and after treatment, normalized for comparison. c) S 2p spectra for untreated, and treated MoS_2 layers, normalized for comparison.

reduction has taken place. We also observe a large contribution from Au in the Au^{3+} oxidation state.[203] This suggests that the $AuCl_3$ solution is in excess, and not all of the solution has been involved in the redox reaction. The largest contribution is from an intermediate Au oxidation state. The disproportionated solution, intermediate Au oxidation states from the redox reaction, or reactions with the ambient atmosphere could all contribute to producing intermediate charge states. For the 20 mM $AuCl_3$ treatment we still observe that the largest contribution is from the intermediate charge state, with a larger contribution from the Au^0 charge state aligned with a greater degree of MoS_2 oxidation-Au reduction.

Optical investigations also indicate p-type doping. We conducted low-temperature photoluminescence measurements to evaluate the $AuCl_3$ treatment's effects on the optical properties of monolayer MoS_2. Low temperature (low-T) PL measurements are better

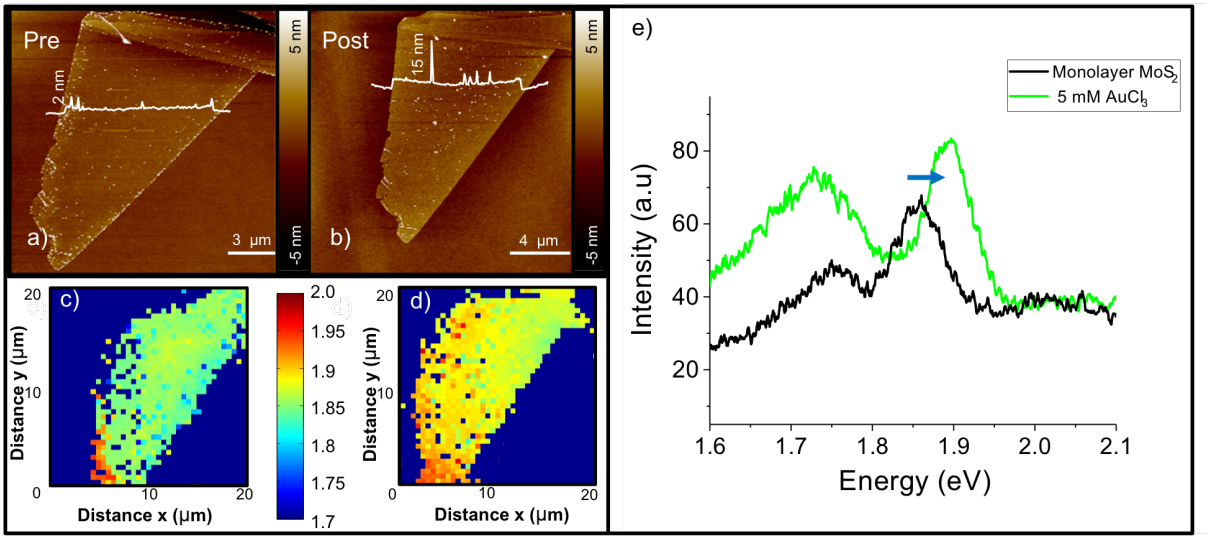

Figure 6.4. Low-temperature photoluminescence characterization of $AuCl_3$ treatment on a MoS_2 monolayer. a) AFM before treatment, b) AFM after treatment, c) PL map before treatment, d) PL map after treatment, e) representative PL spectra before and after treatment.

able to isolate excitonic effects, as they remove many thermally activated processes such as phonon interactions. Low-T PL better resolves the constituent excitonic peaks, and shows a small blue shift described by the temperature dependent Varshni relationship for semiconductors.[204] Looking at these properties under vacuum helps remove adsorbates from the surface, reducing unwanted absorbate interactions. Figure 6.4 shows the AFM image of a MoS_2 image before and after treatment. This particular spincoating treatment left only a few, small (< 10 nm) Au NPs on the surface. As such, there should not be a strong plasmonic effect on the properties. In the supporting information we detail a case when a large number of Au NPs lead to plasmonic PL enhancement, but this is not the focus of the current study. We observe that the optical signatures are consistent with p-type doping. Figure 6.4 shows a representative spectra before and after treatment. We observe a consistent blue shift after treatment and enhancement of the defect states.

This indicates p-type doping of the monolayer. As electrons are removed, the trion peak (A-) is suppressed, leading to greater contribution from the higher energy neutral exciton peak (A).[205, 206] Typically excess electrons passivate sub-bandgap defect states. As electrons are removed these defect states are no longer passivated, leading to a greater contribution from the defect states. Defects introduced by the $AuCl_3$ treatment could also contribute to this defect state enhancement. We observe that the p-type doping behavior is consistent throughout the flake, as shown in the pre and post maps. Before treatment, the monolayer combined A/A- exciton/trion peak is centered at 1.86 eV, while after treatment the combined A/A- exciton/trion peak is centered at 1.895 eV. The 1.895 eV peak is blueshifted relative to a previously reported monolayer MoS_2 undoped sample at low T, again indicating p-type doping.[207] This shift is homogeneous throughout the maps.

6.2.2. Patterning $AuCl_3$ dopant via polymer pen lithography

We employ a novel patterning technique to control the lateral extent of the $AuCl_3$ solution on the MoS_2 monolayers. Polymer pen lithography (PPL) is a direct write patterning technique that utilizes arrays of elastomeric tips to precisely deposit chemical inks on a substrate.[194] Supplementary figure 6.13 shows a schematic of the polymer pen process. The PDMS tip is coated in $AuCl_3$ in nitromethane, which is then pressed onto the MoS_2 surface, leaving behind $AuCl_3$ solution which both forms the Au NP and dopes the MoS_2 layer. The polymer pen process is dependent on several factors: surface properties, solvent evaporation rate, and environmental conditions. We pre-tested substrates

for hydrophobicity or hydrophilicity, but future experiments could further optimize this process.

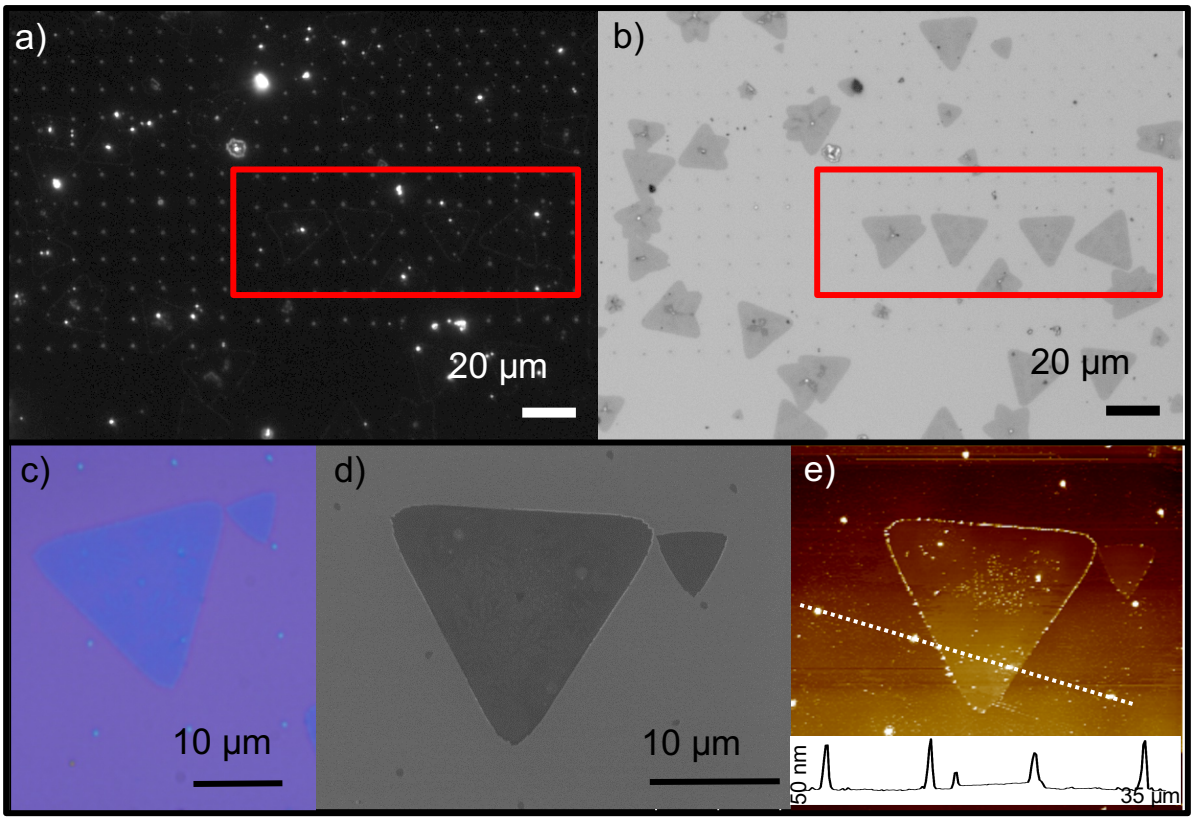

Figure 6.5. PPL patterning of $AuCl_3$ treatment on MoS_2 monolayer. a) dark field image of MoS_2 region patterned with $AuCl_3$ solution b) corresponding bright field image. C) Higher-magnification optical micrograph of patterned MoS_2 monolayer, d) corresponding SEM image and e) AFM image with height profile at bottom from white dotted line.

We utilize PPL to deposit the $AuCl_3$ nitromethane solution on the MoS_2 monolayer. Figure 6.5 shows polymer pen patterning of the $AuCl_3$ solution on MoS_2 monolayers. Figure 6.5a and Figure 6.5b shows the same area. Figure 6.5a is a dark field image; the rows of patterned dots result from scattered light from the deposited Au NPs. Figure 6.5 shows that same region under bright field; on close inspection in the red highlighted

regions, one can see that several of the Au NP bright dots, corresponding to scattering Au NPs, are patterned directly on the MoS_2 monolayers. Both images highlight the large area patterning enabled by PPL. Figure 6.5c shows an optical micrograph of one MoS_2 triangle at higher magnification, while Figure 6.5b and 6.5c show the corresponding SEM and AFM images. All three show regular patterns of the Au NPs. On close inspection of Figure 6.5b and 6.5c, it appears that there is some diffusion of the $AuCl_3$ solution, leading to smaller Au NPs surrounding the large Au NP. The height inset in Figure 6.5e shows the large Au NPs are on the order of 50 nm, while the surrounding small Au NPs are on the order of a few nm. This shows an ability to directly control Au NP placement.

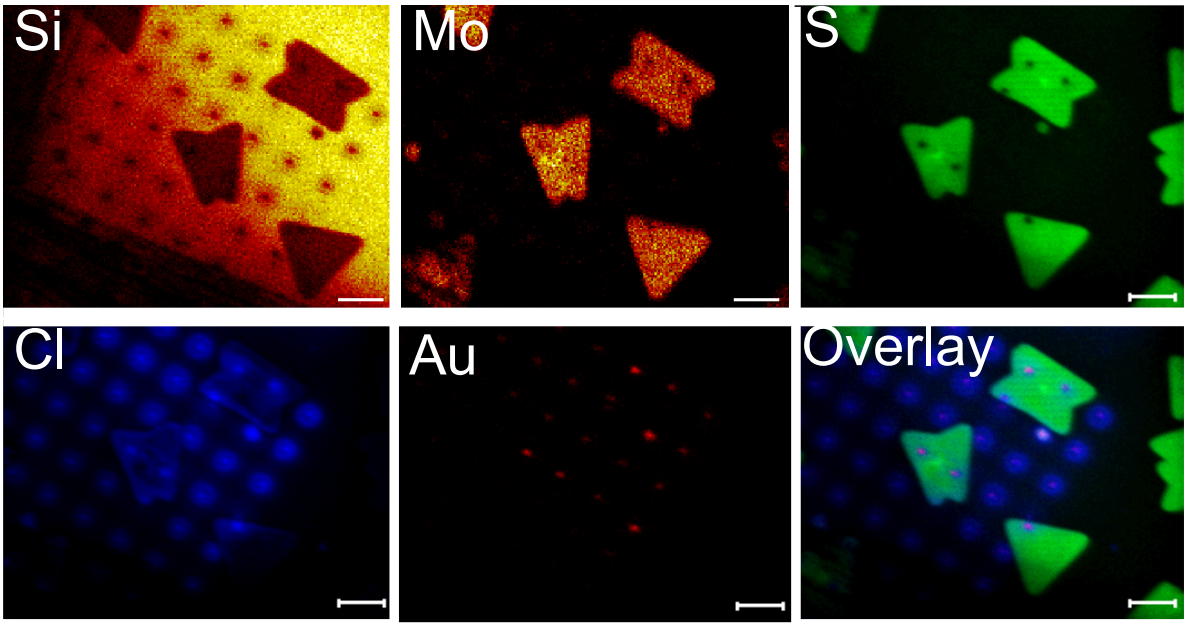

Figure 6.6. SIMS characterization of $AuCl_3$ patterning on MoS_2 monolayers. The different squares correspond to different mass isotopes, while the last area, titled "Overlay", overlays the S, Cl, and Au signal to highlight the chemical patterning on the MoS_2 monolayers. Scale bars represent 5 μm.

Figure 6.6 shows Secondary Ion Mass Spectroscopy (SIMS) characterization of a patterned sample. Each SIMS map corresponds to a single mass isotope; this identifies the chemical composition of the signal. The Mo(98) signal was taken under positive ion mode, while the Si(32), S(28), Cl(35), and Au(197) maps were taken under negative ion mode. From the Si, Mo and S maps, one can observe several triangular MoS_2 flakes. The Cl and Au signal show the patterned region, corresponding to the PPL patterning of the $AuCl_3$ solution. The overlay map shows the S, Cl and Au maps combined. From the overlay map we can clearly see that the Au (giving purple dots in the overlay map) and the Cl signal overlap the MoS_2 flakes. The Cl spreads to a larger extent than the Au signal, suggesting an Au NP surrounding by excess solution. Taken with Figure 6.5, these results show clear evidence of the successful PPL patterning of the $AuCl_3$ dopant on the MoS_2 monolayers.

6.2.3. Conclusions

To conclude, we present a detailed study of the $AuCl_3$ p-type doping process of MoS_2 as well as present a new patterning technique to spatially control the $AuCl_3$ deposition process. We give structural analysis of the $AuCl_3$ treatment, showing TEM, SEM, and AFM characterization of the $AuCl_3$ treatment on MoS_2 monolayers. We show evidence of the p-type doping via transport, XPS analysis, and low-temperature PL optical characterization. As 2D materials are all surface, they are particularly susceptible to charge transfer-doping techniques. This study will help elucidate how to better utilize these charge transfer approaches. We also present a PPL technique to precisely pattern the

$AuCl_3$ p-type dopant and resulting Au NP deposition. This technique is potentially extendable to a wide array of charge transfer inks and TMDs, presenting a new way to precisely sensitize the 2D TMDs.

6.3. Methods and Supporting Information

6.3.1. Methods

MoS_2 CVD growth: MoS_2 was grown via the previously reported MoO_3-based CVD technique.[208] In addition, a small amount of seed molecule perylene-3,4,9,10-tetracarboxylic acid tetra potassium salt (PTAS) was applied to the substrate to enhance growth.[209]

MoS_2 mechanical exfoliation: Monolayer MoS_2 samples were made using mechanical exfoliation from bulk crystal on 285nm SiO_2 capped, p-doped silicon substrates. Suitable samples were identified by optical microscopy and thickness was confirmed independently through atomic-force microscopy. Chosen samples were first annealed at 400 C in Ar/H_2 to remove residue from the exfoliation process.

$AuCl_3$ solution preparation: Solutions of either 5 mM or 20 mM $AuCl_3$ were prepared in anhydrous nitromethane, forming yellow solutions. They were stored in oven-dried 20 mL scintillation vials with an over-pack of Drierite and kept in the dark.

$AuCl_3$ doping process: $AuCl_3$ solutions were spin coated onto substrates at 4000 RPM for 30 seconds. The substrates were then put on a hot plate at 50C for 5 min to encourage nitromethane evaporation and further reduction-oxidation.

XPS analysis: XPS spectra were obtained with monochromated Al K-alpha radiation with a 900 um aperture and calibrated to the C-C peak at 284.6 eV. Doublet peaks were constrained to the same FWHM. The relationships for doublet peaks were applied as

follows: For Mo 3d spectra, the $3d_{3/2}$ energy was constrained to 3.15 eV higher than the $3d_{5/2}$ peak, for Cl the $2p_{1/2}$ was constrained to 1.6 eV higher than $2p_{3/2}$, for the S 2p spectra, the $2p_{1/2}$ peak was constrained to 1.15 eV higher than $2p_{3/2}$. For the Au 4f spectra, the $4f_{5/2}$ energy was constrained to 3.7 eV higher than the $4f_{7/2}$ peak.

$AuCl_3$ patterning procedure: Polymer pen arrays were fabricated following a previous report.[210] A nitromethane solution containing 5 mM of $AuCl_3$ was drop-casted onto a polymer pen array as the ink. The array was attached to the Z scan head of an AFM (Park System XE-150) against the substrate that supports MoS_2 flakes. Then, the tips of the pen array was brought in contact with the MoS_2 flakes to transfer the ink down to local areas.

Low temperature PL: Photoluminescence measurements were performed using a continuous wave 532nm laser, with a set laser power of 50 μW and 300 μW and spot size of ~1 micron using a 100x objective with NA of 0.70. Collection was performed using an Andor Spectrometer on a 300 lines/mm grating. Measurements were performed before and after 5 mM $AuCl_3$ treatment.

6.3.2. Supporting figures

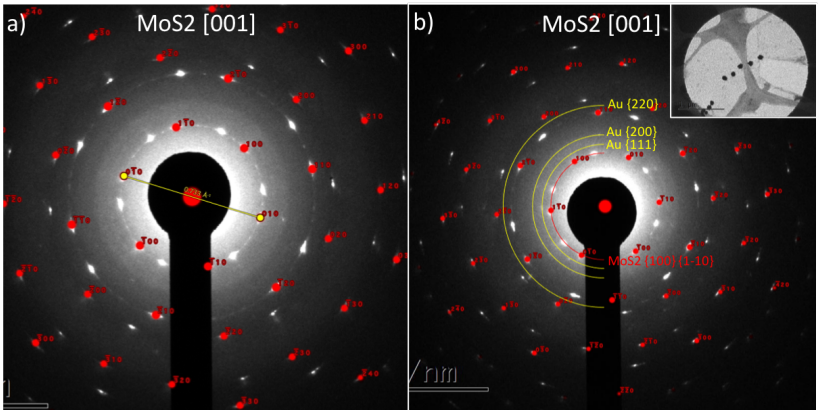

Figure 6.7. Diffraction patterns of MoS_2 monolayers before and after $AuCl_3$ treatment.

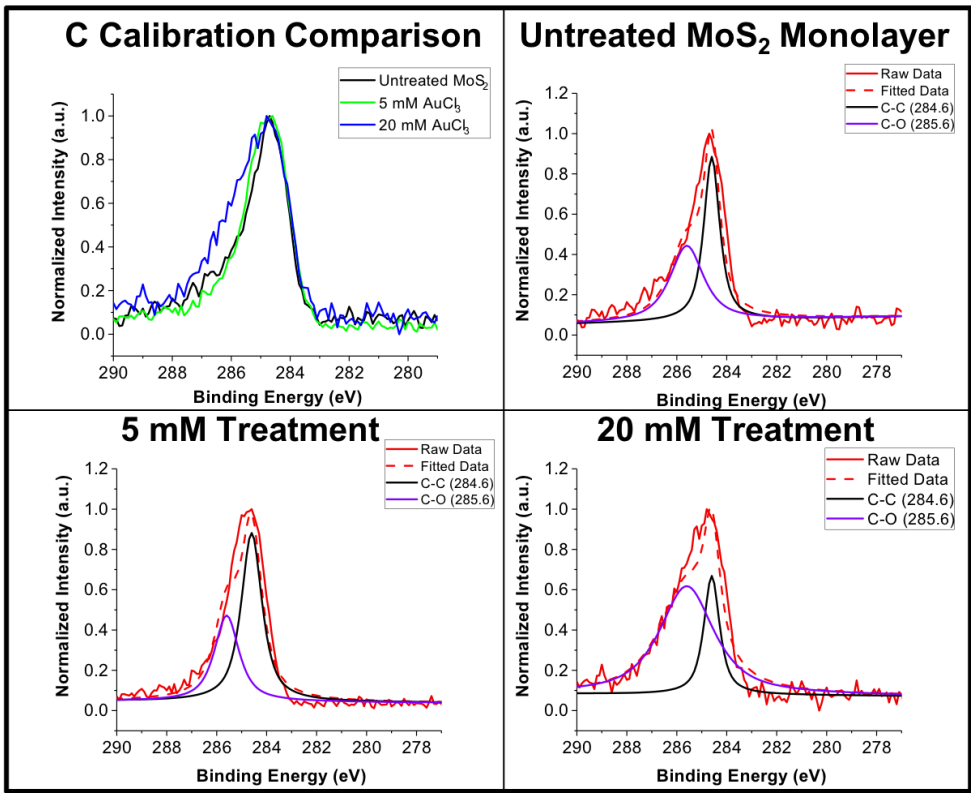

Figure 6.8. XPS carbon calibration spectra. The first panel shows the three spectra overlaid, while the remain spectra show the fitting for the C-C peak.

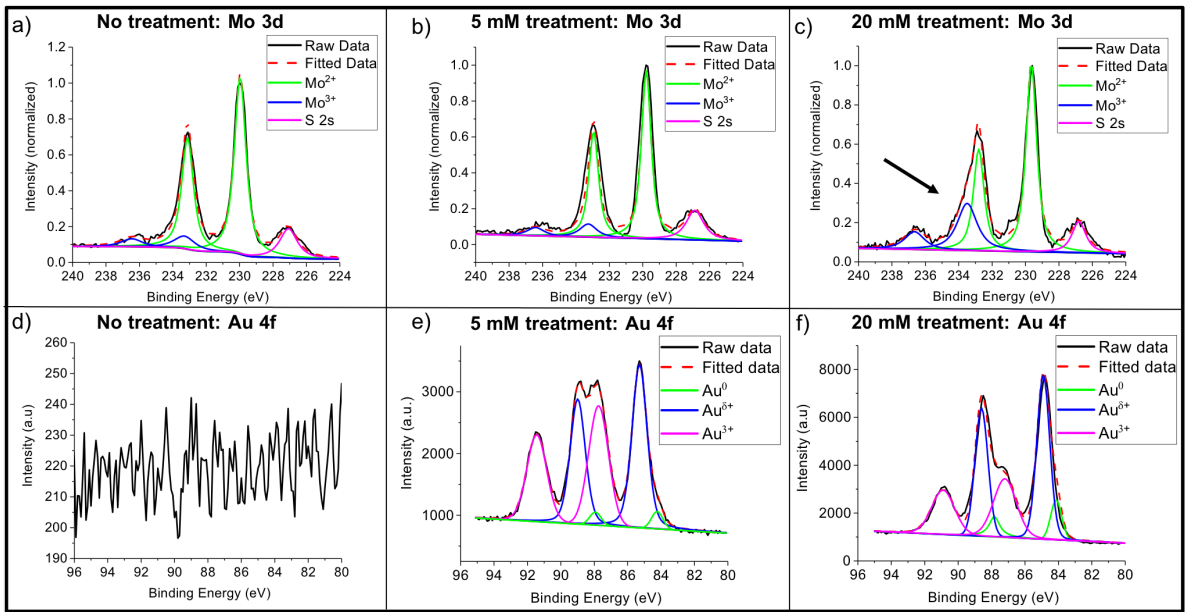

Figure 6.9. XPS analysis of $AuCl_3$ treatments. a) Shows the Mo 3d scan for MoS_2 without treatment, while b) shows after a 5 mM $AuCl_3$ treatment and c) shows after a 20 mM treatment. d) shows the Au 4f scan for MoS_2 without treatment, while e) shows the Au 4f scan after a 5 mM treatment and f) shows the Au 4f scan after a 20 mM $AuCl_3$ treatment.

6.3.3. Supporting analysis

6.3.3.1. Higher concentration Au NPs lead to enhanced light-matter interactions. When depositing a large concentration of Au NPs, the spincoating $AuCl_3$ treatment can also increase light-matter interactions with the MoS_2 monolayer. Figure 6.10d shows an averaged low-temperature photoluminescence spectra of a mechanically exfoliated MoS_2 sheet before and after 5 mM $AuCl_3$ treatment. Both before and after treatment, there are signatures of the A/A- peak and a broad defect peak.[211] We observe that the average A/A- exciton PL emission intensity is enhanced over 3-fold after the $AuCl_3$ treatment producing a high concentration of larger Au NPs.

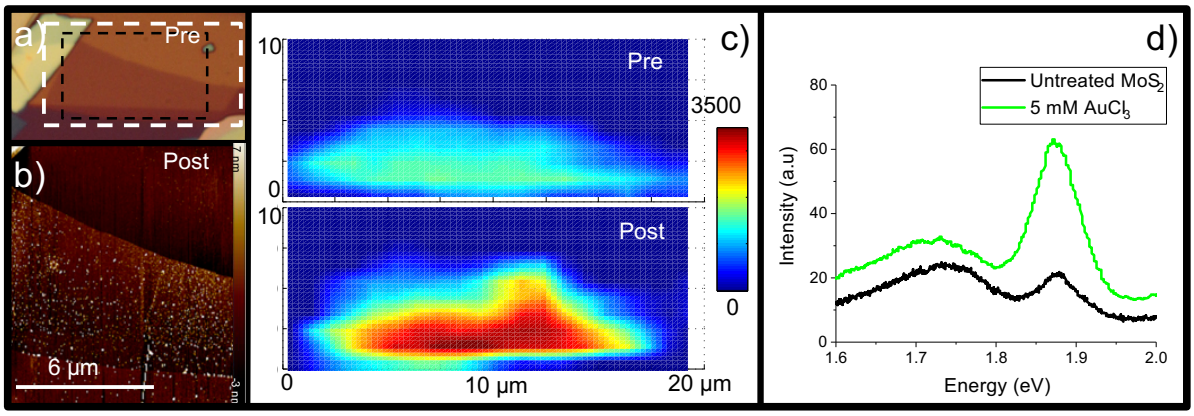

Figure 6.10. Low-temperature photoluminescence measurements of $AuCl_3$ treated MoS_2 monolayers. a) optical image of the monolayer flake before treatment, b) AFM image of the flake after treatment, c) PL map before and after treatment map after treatment, d) representative spectra before and after treatment, showing a three fold intensity enhancement.

Figure 6.10a shows an optical image of the monolayer flake pre treatment and b shows an AFM image of the same flake post treatment. Figure 6.10c shows the PL map pre (top) and post (bottom) treatment. The maps show the intensity of emission from the direct band gap A/A- exciton. The map post-treatment shows a strong PL enhancement throughout the flake, with increased enhancement along the bottom edge. This enhancement can be explained by plasmonic enhancement from Au NPs. Figure 6.10b AFM shows a concentration of Au NPs on the order of 15 nm throughout the flake. Figure 6.11 shows a height profile along two directions. We observe in the AFM image a greater density of larger Au NPs (~30 nm) along the bottom border. Correspondingly, we see additional PL intensity along the bottom border of the monolayer region.

We surmise that the enhanced intensity is due to the plasmonic behavior of the Au NPs. It is well established that Au NPs can increase MoS_2 photoluminescence yield via plasmonic enhancement.[148, 212, 213] PL plasmonic enhancement is due to both

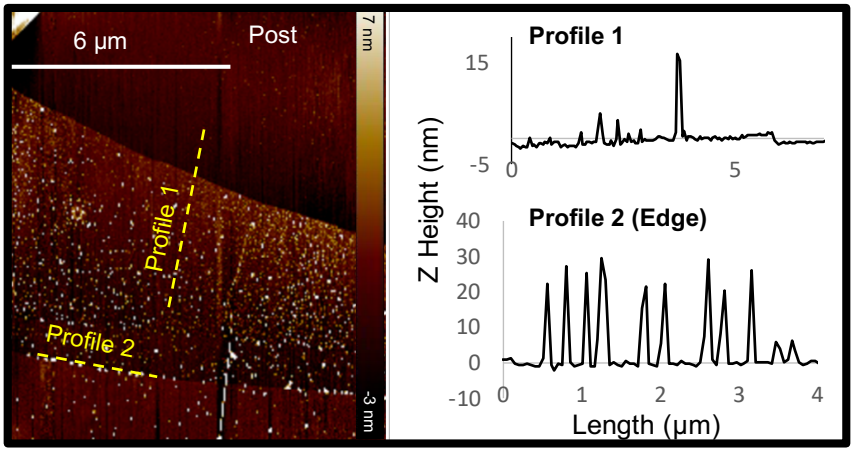

Figure 6.11. More detailed AFM analysis of $AuCl_3$ treated monolayer from Figure 6.10, showing aggregation of larger Au NPs on the bottom edge.

enhanced MoS_2 absorption and emission.[214] The monolayer sheet has a very small absorption cross-section; monolayer MoS_2 generally shows an absorption efficiency around 3%.[215] Plasmonic particles on the surface of the monolayer sheet can enhance the local electric field, increasing the local light absorption.[214] We performed discrete dipole analysis (DDA) calculations to better understand which size of Au NPs should contribute to plasmonic enhancement. Figure 6.12 shows the results of these calculations. Figure 6.12a shows the simulated absorption curves of various Au NPs. For modeling simplicity, the nanoparticles were modeled as spheres. Previous reports have indicated that dendritic-type particles (nanourchins or nanostars) should following similar trends, with a redshift due to hybridization between dipoles and high-order multipoles.[216] Plasmonic enhancement should be greater with greater absorption curve overlap. Based on these absorption curves, while all nanoparticles may be able to contribute to absorption, the amount of plasmonic enhancement should increase with size (up to 100 nm). This conclusion is reinforced by the electric field distribution curve calculations. Figure 6.12b shows an example

calculated structure; we modeled a single nanoparticle on a MoS_2 monolayer. Figure 6.12c shows the resulting electric field distributions. The numbers below show the maximum electric field enhancement $(E/Eo)^2$. In accordance with the absorption curves, the electric field maximum on the MoS_2 layer increases with size up to 100 nm. This aligns with our observation of more enhancement along the bottom edge of the monolayer, where a concentration of larger ~35 nm particles aggregated.

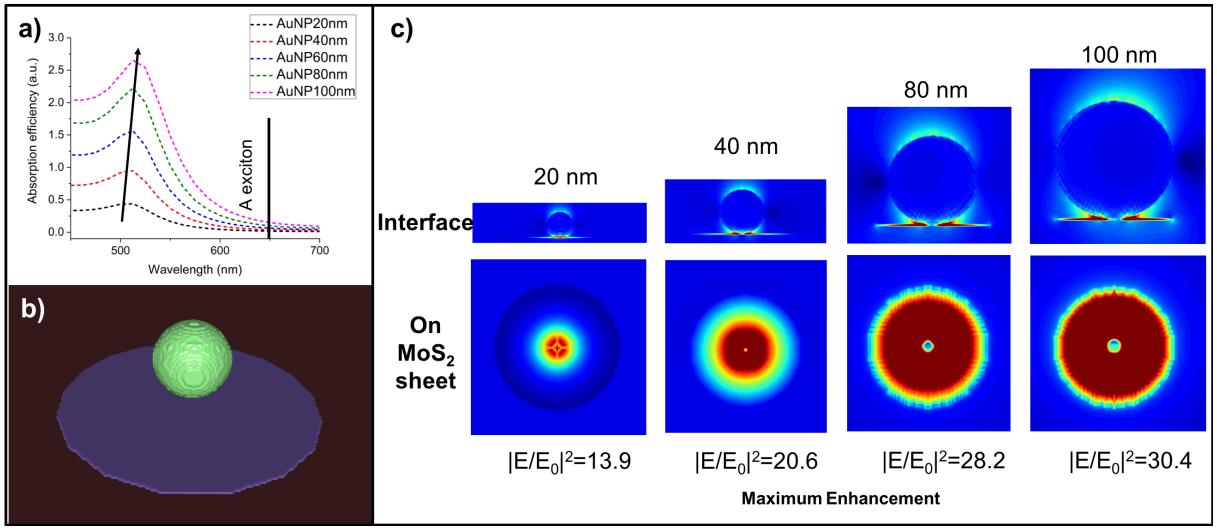

Figure 6.12. DDA calculations of plasmonic properties. a) shows simulated absorption curves for the Au NPs superimposed on the MoS_2 monolayer A exciton energy b) shows the simulated image and c) shows the electric field enhancement by nanoparticle size (532 nm incident light).

6.3.3.2. PPL process and optical properties. Figure 6.13 shows the PPL patterning process. The PDMS tip is coated with the $AuCl_3$ nitromethane solution, then the tip is brought in contact with MoS_2 surface, leaving behind solution which participates in the redox reaction, leaving behind Au NPs and a p-type doped MoS_2 surface.

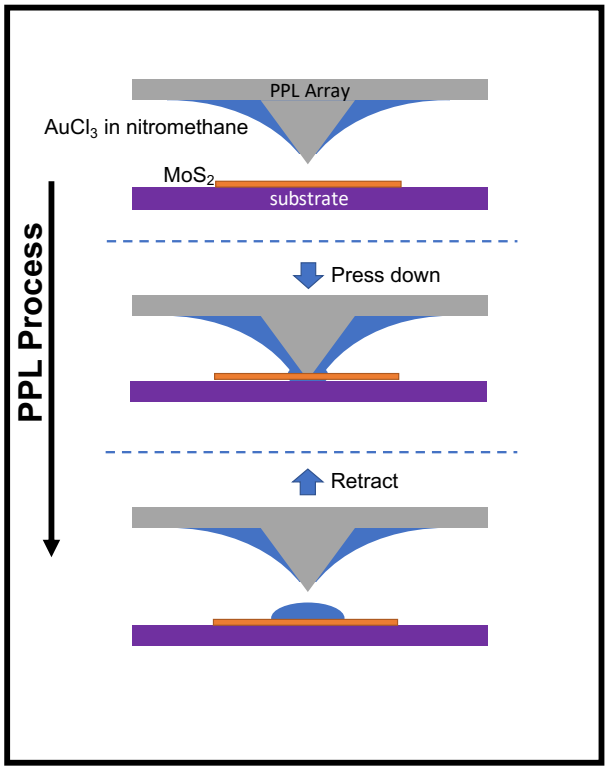

Figure 6.13. Polymer pen lithography (PPL) process is comprised of the following: the PDMS tip is coated with the $AuCl_3$ nitromethane solution, then the tip is brought in contact with MoS_2 surface, leaving behind solution which participates in the redox reaction, leaving behind Au NPs and a p-type doped MoS_2 surface.

6.3.3.3. PPL process optical characterizations. Preliminary optical characterization confirms that the PPL process can p-type dope the MoS_2 monolayer. We investigated the optical properties of the patterned samples. For the fully patterned samples, we observed a similar optical shift of the combined A/A- peak position. Figure 6.14 shows

a MoS_2 monolayer before and after PPL $AuCl_3$ treatment. We see via AFM analysis that the patterning has successfully been applied to the monolayer. The Au NPs are on the order of 15 nm, surrounded by sub 5 nm particles (shown in Figure 6.14). Given the small area of the MoS_2 monolayer, it appears that the patterned dots were applied to the entire surface. This aligns with the SIMS data, which indicates the current PPL process deposits Au NPs surrounded by dopant circles with a radius of ~1 μm. Given the dense PPL pattern, the treatment was applied everywhere on the monolayer sheet (shown by the 1-2 nm Au nanoparticles everywhere on the surface). Figure 6.14c and 6.14d show the PL intensities for a line scan across the sheet before and after treatment respectively (energy scale is on the x-axis, line scan distance is on the y-axis). The treatment leads to a relatively homogenous p-type doping of the layer similar to the spincoating treatment, as indicated by the PL blueshift and defect state enhancement. The PL shows a 15 meV blue shift (a smaller shift than for the spincoating treatment), as shown in Figure 6.14e.

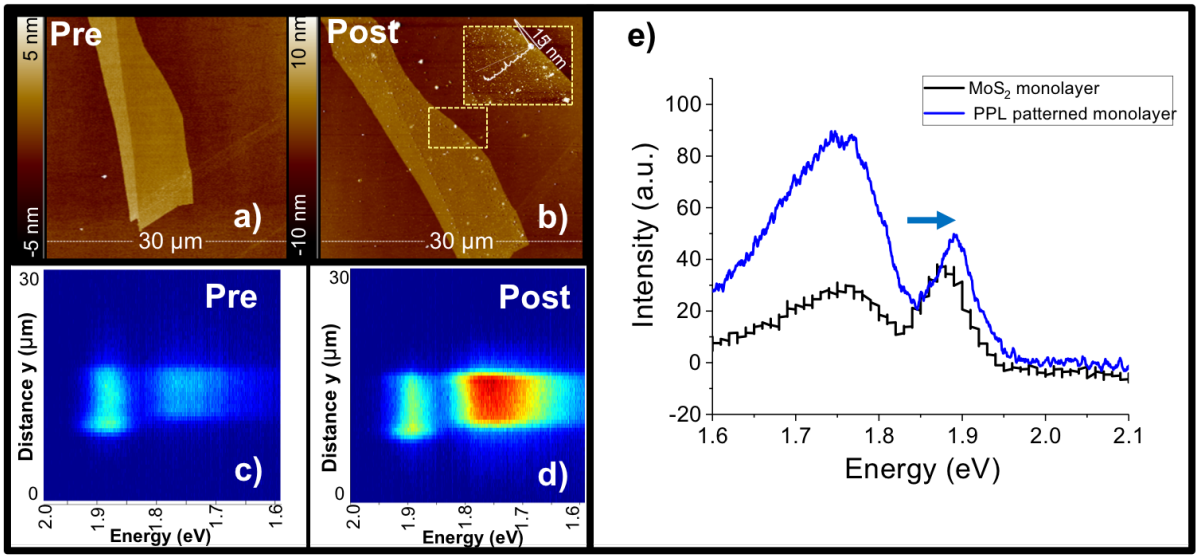

Figure 6.14. Optical characterization of the PPL-treated MoS_2 monolayer. a) AFM pre treatment, b) AFM post treatment showing large-area patterning, (inset) zoomed in AFM treatment showing a height profile of a 15 nm nanoparticle surrounded by <5 nm Au NPs. c) PL line scan before treatment, d) PL line scan after treatment, e) averaged representative spectra before and after treatment showing the exciton blue shift after treatment consistent with p-type doping.

CHAPTER 7

Future directions in the field

7.1. Thesis summary

This thesis presents several case studies in 2D oxide and chalcogenide synthesis and property engineering. Chapter 1 introduces the 2D oxide and chalcogenide field, current synthesis techniques, and current chemical-based property engineering techniques.

In chapter 2, the evaporative thinning synthesis technique was applied to a ternary chalcogenide system for the first time to produce a Bi-rich, selenium and tellurium-doped monolayer sheet. This shows the wide adaptability of the evaporative thinning technique to produce high-quality monolayer materials. The chapter also presents a case study in careful stoichiometry characterization at the nanoscale; this is critical given the large shifts in electronic properties that can be induced by small stoichiometry shifts. Additionally, a preferential evaporative thinning mechanism and resulting structure is presented.

Chapter 3 demonstrates a novel physical vapor deposition synthesis for few-layer MoO_3. We present an electron beam dose-based property engineering technique to introduce substoichiometry into the structure (MoO_{3-x}), thereby introducing gap states into the electronic structure and n-type doping the material. In-situ transport measurements are combined with core-loss and monochromated low-loss STEM studies to develop a detailed structure-property relationship between Mo oxidation state and resistance. We present a radiolysis-based mechanism for the oxygen vacancy introduction, and conduct

DFT studies to inform the oxygen defect configurations. We report that the terminal oxygens are most susceptible to vacancy introduction. In sum, we present a new synthesis and dose-based property engineering technique to bring few-layer MoO_3 and substoichiometric MoO_{3-x} into the 2D materials family with exquisite electronic property tunability.

Chapter 4 presents CVD-based growth of the transition metal dichalcogenides and heterostructures. Led by Dr. Jeffrey Cain, we develop a robust method for growing a wide variety of TMDs (MoS_2, $MoSe_2$, WS_2, WSe_2), as well as their constituent alloys and heterostructures. Substitutional doping and alloying presents one method of engineering TMD electronic structure and properties. While this approach is promising, there are limitations to the level of the property-engineering control that can be achieved by current CVD growth methods. In chapter 4, I describe the motivation for additional chemical-based methods of electronic property control.

Chapter 5 and chapter 6 present two different property engineering techniques to modify TMD optoelectronic properties. Chapter 5 presents lithium intercalation of monolayer $MoSe_2$, via treatment with the aggressive chemical n-butyllithium, as a way to engineer the monolayer $MoSe_2$ phase directly on a chip. The 2H to 1T' transition is accompanied by a variety of optical and electronic structure changes. Interestingly, the lithium-treated 1T' phase is more transparent (higher transmission in the visible spectrum) than the semiconducting 2H phase due to lithium intercalation-based band structure changes. Despite these promising physical and optical properties, we also highlight the challenges in this highly-touted on-chip phase engineering approach. The n-butyllithium shows inhomogeneous kinetics that makes patterning inconsistent, and lithium intercalation between the monolayer and substrate suggests the monolayer is unstable. Together, this indicates

that while the lithium intercalation 1T' phase holds interesting properties and promise, on-chip phase engineering is not a robust process for device construction. It also indicates that intercalation chemistry based-property engineering may be challenging to control and implement at the on-chip monolayer limit for electronics applications. Alternatively, chapter 6 presents a charge-transfer based property engineering technique to p-type dope monolayer MoS_2. We present structural and chemical characterization of the on-chip $AuCl_3$ doping process to understand the redox chemistry at play. Further, we present a polymer pen lithography (PPL) technique to pattern the $AuCl_3$ deposition process.

Together, these works advance both the synthesis and control of the all-surface 2D chalcogenides and oxides. As in Brattain's Nobel Lecture describing the importance of surfaces, we work to better understand and control these surface systems to describe novel phenomena. The following section outlines future research directions to build on the presented works.

7.2. Future directions

7.2.1. Future directions for chapter 2: evaporative thinning of Se-doped Bi_2Te_3

Chapter 2 showed the generalizability of the evaporative thinning synthesis technique to ternary compounds. Evaporative thinning is a versatile technique that could be applied to a variety of binary and ternary compounds to produce 2D sheets. Other groups have shown that evaporative thinning can be used to synthesize 2D MoS_2 and black phosphorus.[217, 218] For evaporative thinning to be applied, the target material must

evaporate congruently (as individual molecular uniques). In general, the evaporative thinning synthesis method should be employed as a technique for challenging to synthesize 2D chalcogenide materials.

In addition, chapter 2 synthesized a novel monolayer Bi-rich compound in the Bi-Te-Se system. This structure should be further investigated for transport properties. With its predicted structure similar to the Bi-rich Bi_7Se_3 compound, we would expect to see semi-metallic transport and potential spin-splitting; this may be modified by quantum confinement effects.[11, 95]

7.2.2. Future directions for chapter 3: synthesis and property engineering of few-layer MoO_3

7.2.2.1. MoO_3-based 2D heterostructures. Chapter 3 described a novel synthesis and electron-beam based property engineering technique to bring few-layer MoO_3 and the substoichiometric form MoO_{3-x} into the 2D family. Few-layer MoO_{3-x} shows great potential to be integrated into 2D heterostructures and devices. With its extremely high work function, few-layer MoO_{3-x} could be integrated with other 2D materials to hole-dope adjacent materials.[2, 22] This could be used to both lower contact resistance of the adjacent material as well as could be used to create p-n junctions (adjacent p-type doped material, and n-type MoO_{3-x}). Fabrication of these 2D heterostructures could be instigated via both direct growth of the MoO_{3-x} material on a previously created 2D substrate, or via physical stacking of the MoO_{3-x} on a different 2D material. As a result, fully 2D p-n junctions could be formed to create diodes, solar cells, and complex transistors.

7.2.2.2. In-situ transport techniques applied to 2D nanoarchitectures. We reported in chapter 3 in-situ transport measurements of the modified 2D MoO_{3-x} nanosheets. This in-situ transport technique could be more generally applied to newly developed 2D materials and nanoarchitectures. The advantage of this technique is that it does not require the frequently-damaging processing required for electron-beam lithography or photolithography. It can be used to better probe the pristine properties of the 2D materials, particularly those that are processing-sensitive.

7.2.2.3. Energetic-beam based 2D property engineering. In chapter 3 we presented an electron dose-based technique to introduce oxygen vacancies into the MoO_3 network, forming MoO_{3-x}. This electron dose-based vacancy introduction is potentially extendable to other 2D chalcogenides and oxides, as radiolysis generally leads to anion vacancies.[130] Preliminary anion defect engineering has been shown in MoS_2, but could be extended to other members of the 2D chalcogenide and oxide family to engineer their electronic properties.[219] As an additional benefit, the electron dose can both be tuned and spatially controlled via electron beam lithography, providing a local property engineering technique for 2D structures.

Ion beam-based property engineering should also be explored as a possible economically-attractive alternative. Ion beams are frequently used in the semiconductor industry for local surface manipulation and implantation doping. The energetic ion beam could similarly be used to introduce anion vacancies into 2D oxides and chalcogenides to alter their optoelectronic properties.

7.2.3. Future directions for chapters 4-6: TMD property engineering

7.2.3.1. 1T' TMD phase engineering. In chapter 5 we highlight both the promise and limitations presented by on-chip n-BuLi-based TMD phase engineering. While we caution against using the on-chip n-BuLi phase engineering for contact resistance reduction and complex device fabrication, there are interesting physics to explore within the 1T' monolayer TMD systems. We suggest that 2D researchers continue their efforts on the energetically-accessible $MoTe_2$ 1T' system (only 35 meV separate the 2H and 1T' phases).[165]

Additional efforts could be focused on finding a more controllable n-type dopant to incur the 1T' phase transformation in the TMD systems. Within our lab, we attempted using lithium hydride without success, but it is possible that other strong n-type dopants could be used to incur degenerate doping, and potentially the 1T' transformation.

7.2.3.2. MoS_2-$AuCl_3$ p-type doping and polymer pen controlled deposition.

7.2.3.3. Redox chemistry property engineering. In chapter 6 we present a redox-chemistry based approach to p-type dope the TMDs, changing the majority carrier type. We present detailed structural and chemical characterization of the p-type doping process. To date, this approach has only been showed for MoS_2. As a first step, future work should extend the $AuCl_3$ doping system to the other n-type TMDs ($MoSe_2$, WS_2), to study the resulting electronic, structural, and chemical changes.

This type of redox chemistry should be further pursued to create a library of chemical engineering tools, in conjunction with the library of 2D materials. Together, this will enable a much broader variety of properties, devices, and physics to be explored. There are a variety of similar high work function metal chlorides that should be investigated,

such as $PdCl_3$, $RhCl_3$, and $IrCl_3$.[220] These have previously been shown to p-type dope graphene, and have not been explored to date in the 2D chalcogenide or oxide systems.

7.2.3.4. Polymer pen lithography as sensitization platform. Polymer pen lithography has the potential to be a wide-ranging platform for 2D sensitization and local engineering. In particular for the MoS_2-$AuCl_3$ system, future work should continue to optimize the PPL process and utilize the PPL process to locally dope the monolayer to create large-scale p-n junctions. The PPL system could also be used with a variety of functional chemistries. The Mirkin group has previously published on utilizing the PPL platform to pattern a variety of biological, chemical, and nanoparticle functionalizations, highlighting the widespread applicability of the patterning platform.[210, 221–223] Future work should investigate utilizing these chemistries to create complex and precisely patterned nanocomposites for synergistic properties with the 2D monolayers. Of particular interest are surface functionalization that takes advantage of the terminating thiol or oxide group; thiol chemistry is a well-developed field, particularly for biologically relevant functionalization.[65, 224, 225] In addition, PPL is compatible with a combinatorial approach that could allow for a large variety of chemistries and functionalizations to be investigated in parallel. With PPL's patterning tunability, the sensitizing elements (such as nanoparticle antennas) could be tuned by sensitizer size/shape, array periodicity, array size, and array shape.

In order to take advantage of the PPL platform, a variety of system parameters need to be controlled and optimized, such as:

- Surface properties: The underlying substrate has been shown to largely control the surface wetting properties of monolayer TMDs.[226] As such, the underlying

surface wetting properties should be tightly controlled to create reliable patterning conditions.

- Chemical ink solvent: The solvent has to be carefully controlled, to have the proper evaporation rate to be reliably patterned via microcontact printing, as well as to interact in the desired fashion with the target chemistry. This latter part should be carefully considered; for example, in our preliminary experiments $AuCl_3$ in dimethyl sulfoxide (DMSO) showed much lower p-type doping than $AuCl_3$ in nitromethane, despite similar solvent polarities.
- Environmental conditions: Previous reports have shown that environmental humidity can be absorbed into the PDMS tip array, thereby altering the tip properties. Analytical descriptions can be used to estimate these effects and adjust the patterning procedure accordingly.[227]

With this approach, a wide variety of surface property engineering techniques could be developed and patterned on 2D surfaces.

7.3. Outlooks on 2D chalcogenides and oxides

The field of 2D chalcogenides and oxides has rapidly advanced over the last five years. However, there are several key challenges that the field as a whole needs to overcome to significantly advance to new physical breakthroughs and potential technological viability. Similar to how Brattain's groundbreaking research into p-n junctions was enabled by the painstaking work of metallurgists purifying the germanium crystal growth and doping techniques, future breakthroughs in 2D materials will be enabled by advances in synthesis, doping, and patterning.

7.3.0.1. Materials synthesis and control. Materials quality is critical to downstream investigations. Recent advances have centered on new vapor-phase synthetic techniques to achieve one of two aims: wafer-scale growth, or heightened lateral control for heterostructures. Recent reports by Sahoo et al. and Zhang et al. both describe physical vapor deposition-based methods to create lateral superlattices via block-by-block epitaxial growth.[228, 229] These types of precise superlattices lend themselves to new physical studies of complex, interacting quantum confinement effects. However, the yield of these high-precision structures is low. On the other end of the scale, Kang et al. have pioneered wafer-scale growth of MoS_2 and WS_2 via metal organic chemical vapor deposition.[47] A grand challenge of the field will be bringing both of those characteristics to a single growth; large-scale growth with precise material quality and structure control. To enable that to happen, materials scientists will need to develop deep understanding of the mechanisms underlying these particular growths in order to engineer the developing reaction, control defect states, and engineer resulting properties. This will build a robust 2D platform that will allow for new types of experiments and investigations to take place.

7.3.0.2. Extrinsic doping. Additional effort needs to be made in property engineering and doping of the 2D chalcogenides and oxides. This thesis represents one set of efforts, but limitations of the current state-of-the-art are readily apparent. Better tunability control at both small and large conductivity ranges are required, such as tuning the transport from degenerately n-type doped to degenerately p-type doped within the 2D plane (similar to Si-electronics). The most promising current approach for such wide swings, the chemical-based property engineering methods described in the introduction as well as chapter 6, currently suffer from short lifetimes. Future efforts should more fully

expand the library of dopants, build out experimental and theoretical understanding of their mechanistic behavior and impact on target 2D materials, as well as develop new chemistries or capping layers to make these chemical reactions longer-lasting and robust.

7.3.0.3. Patterning. Devices require precise spatial control of electronic properties. This could require both patterned materials growth and patterned doping techniques. I present one such approach, polymer pen lithography, but new ways to pattern both material placement during growth and ways to pattern heterojunctions and applied chemical doping techniques will enable further levels of control and optimization.

7.3.0.4. Synergistic multidimensional composites and nanoarchitectures. New opportunities arise from combining the best properties of 2D oxides and chalcogenides with other dimensional architectures (0D, 1D, 3D) to create synergistic composites and nanoarchitectures. Developing synergistic relationships between MoS_2 and Au has been an early research area in this regard: beyond the efforts described in chapter 6, I have also contributed to work encapsulating Au nanoparticles with MoS_2 leading to stronger light-matter interactions, photodetection and hydrogen evolution performance.[148, 212] This approach could be extended across the nanoscale library; 2D materials serve as an ideal planar platform to build up more complex structures with sensitizers such as quantum dots or carbon nanotubes. Emergent properties can also arise at multidimensional interfaces, providing an avenue to novel emergent phenomena. There is a large phase space of nanoarchitectures and composites that could be explored; initial targets should be lead by calculations investigating potential synergistic properties between composite materials.

7.3.1. Summary

Over the last decade, the 2D chalcogenides and oxides have presented an exciting frontier of discovery for new materials properties and physics. The next decade will present new challenges across materials synthesis and quality, property engineering, patterning, and nanoarchitecture fabrication to explore novel structures, physics, and devices.

References

[1] W. H. Brattain, "Surface properties of semiconductors," *Science*, vol. 126, no. 3265, pp. 151–153, 1957.

[2] J. D. Cain, E. D. Hanson, F. Shi, and V. P. Dravid, "Emerging opportunities in the two-dimensional chalcogenide systems and architecture," *Current Opinion in Solid State and Materials Science*, vol. 20, no. 6, pp. 374–387, 2016.

[3] K. S. Novoselov, A. K. Geim, S. V. Morozov, D. Jiang, Y. Zhang, S. V. Dubonos, I. V. Grigorieva, and A. A. Firsov, "Electric field effect in atomically thin carbon films," *Science*, vol. 306, no. 5696, pp. 666–669, 2004.

[4] M. Shulaker, P. Wong, and S. Mitra, "how we'll put a carbon nanotube computer in your hand." Available at https://spectrum.ieee.org/semiconductors/devices/how-well-put-a-carbon-nanotube-computer-in-your-hand, 2016.

[5] Samsung, "Samsung qled tv." Available at http://www.samsung.com/global/tv/, 2018.

[6] "Global graphene battery market 2017- graphenano, sinode systems, xg sciences and graphene 3d lab." Available at https://www.openpr.com/news/470851/Global-Graphene-Battery-Market-2017-Graphenano-SiNode-Systems-XG-Sciences-and-Graphene-3D-Lab.html, 2017.

[7] K. J. Koski and Y. Cui, "The new skinny in two-dimensional nanomaterials," *ACS Nano*, vol. 7, no. 5, pp. 3739–3743, 2013.

[8] S. Das, J. A. Robinson, M. Dubey, H. Terrones, and M. Terrones, "Beyond graphene: Progress in novel two-dimensional materials and van der waals solids," *Annual Review of Materials Research*, vol. 45, no. 1, pp. 1–27, 2015.

[9] Y. Ding, Y. Wang, J. Ni, L. Shi, S. Shi, and W. Tang, "First principles study of structural, vibrational and electronic properties of graphene-like MX_2 (M= Mo,

Nb, W, Ta; X= S, Se, Te) monolayers," *Physica B: Condensed Matter*, vol. 406, no. 11, pp. 2254–2260, 2011.

[10] B. McCombe and G. Seidel, "Magnetothermal oscillations and spin splitting in bismuth and antimony," *Physical Review*, vol. 155, no. 3, p. 633, 1967.

[11] H. Tang, X. Wang, Y. Xiong, Y. Zhao, Y. Zhang, Y. Zhang, J. Yang, and D. Xu, "Thermoelectric characterization of individual bismuth selenide topological insulator nanoribbons," *Nanoscale*, vol. 7, no. 15, pp. 6683–6690, 2015.

[12] Y.-C. Lin, D. O. Dumcenco, Y.-S. Huang, and K. Suenaga, "Atomic mechanism of the semiconducting-to-metallic phase transition in single-layered MoS_2," *Nature Nanotechnology*, vol. 9, no. 5, pp. 391–396, 2014.

[13] G. Eda, T. Fujita, H. Yamaguchi, D. Voiry, M. Chen, and M. Chhowalla, "Coherent atomic and electronic heterostructures of single-layer MoS_2," *ACS Nano*, vol. 6, no. 8, pp. 7311–7317, 2012.

[14] S. Balendhran, J. Deng, J. Z. Ou, S. Walia, J. Scott, J. Tang, K. L. Wang, M. R. Field, S. Russo, and S. Zhuiykov, "Enhanced charge carrier mobility in two-dimensional high dielectric molybdenum oxide," *Advanced Materials*, vol. 25, no. 1, pp. 109–114, 2013.

[15] D. Su and G. Wang, "Single-crystalline bilayered V_2O_5 nanobelts for high-capacity sodium-ion batteries," *ACS Nano*, vol. 7, no. 12, pp. 11218–11226, 2013.

[16] A. Kuc, N. Zibouche, and T. Heine, "Influence of quantum confinement on the electronic structure of the transition metal sulfide TS_2," *Physical Review B*, vol. 83, no. 24, p. 245213, 2011.

[17] K. F. Mak, C. Lee, J. Hone, J. Shan, and T. F. Heinz, "Atomically thin MoS_2: A new direct-gap semiconductor," *Physical Review Letters*, vol. 105, no. 13, p. 136805, 2010.

[18] B. Peng, P. K. Ang, and K. P. Loh, "Two-dimensional dichalcogenides for light-harvesting applications," *Nano Today*, vol. 10, no. 2, pp. 128–137, 2015.

[19] D. Kozawa, R. Kumar, A. Carvalho, K. K. Amara, W. Zhao, S. Wang, M. Toh, R. M. Ribeiro, A. C. Neto, and K. Matsuda, "Photocarrier relaxation pathway in two-dimensional semiconducting transition metal dichalcogenides," *Nature Communications*, vol. 5, 2014.

[20] S. Wu, C. Huang, G. Aivazian, J. S. Ross, D. Cobden, and X. Xu, "Vapor-solid growth of high optical quality MoS_2 monolayers with near-unity valley

polarization," *ACS Nano*, vol. 7, no. 3, pp. 2768–72, 2013.

[21] H. Qiu, T. Xu, Z. Wang, W. Ren, H. Nan, Z. Ni, Q. Chen, S. Yuan, F. Miao, F. Song, G. Long, Y. Shi, L. Sun, J. Wang, and X. Wang, "Hopping transport through defect-induced localized states in molybdenum disulphide," *Nature Communications*, vol. 4, 2013.

[22] S. McDonnell, A. Azcatl, R. Addou, C. Gong, C. Battaglia, S. Chuang, K. Cho, A. Javey, and R. M. Wallace, "Hole contacts on transition metal dichalcogenides: Interface chemistry and band alignments," *ACS Nano*, vol. 8, no. 6, pp. 6265–6272, 2014.

[23] S. Chuang, C. Battaglia, A. Azcatl, S. McDonnell, J. S. Kang, X. Yin, M. Tosun, R. Kapadia, H. Fang, R. M. Wallace, and A. Javey, "MoS_2 p-type transistors and diodes enabled by high work function MoO_x contacts," *Nano Letters*, vol. 14, no. 3, pp. 1337–1342, 2014.

[24] Y.-F. Lin, Y. Xu, S.-T. Wang, S.-L. Li, M. Yamamoto, A. Aparecido-Ferreira, W. Li, H. Sun, S. Nakaharai, and W.-B. Jian, "Ambipolar $MoTe_2$ transistors and their applications in logic circuits," *Advanced Materials*, vol. 26, no. 20, pp. 3263–3269, 2014.

[25] N. R. Pradhan, D. Rhodes, S. Feng, Y. Xin, S. Memaran, B.-H. Moon, H. Terrones, M. Terrones, and L. Balicas, "Field-effect transistors based on few-layered -$MoTe_2$," *ACS Nano*, vol. 8, no. 6, pp. 5911–5920, 2014.

[26] S. Fathipour, N. Ma, W. S. Hwang, V. Protasenko, S. Vishwanath, H. G. Xing, H. Xu, D. Jena, J. Appenzeller, and A. Seabaugh, "Exfoliated multilayer $MoTe_2$ field-effect transistors," *Applied Physics Letters*, vol. 105, no. 19, p. 192101, 2014.

[27] K. Taniguchi, A. Matsumoto, H. Shimotani, and H. Takagi, "Electric-field-induced superconductivity at 9.4 K in a layered transition metal disulphide MoS_2," *Applied Physics Letters*, vol. 101, no. 4, p. 042603, 2012.

[28] R. Roldan, E. Cappelluti, and F. Guinea, "Interactions and superconductivity in heavily doped MoS_2," *Physical Review B*, vol. 88, no. 5, p. 054515, 2013.

[29] S. Jo, D. Costanzo, H. Berger, and A. F. Morpurgo, "Electrostatically induced superconductivity at the surface of WS_2," *Nano Letters*, vol. 15, no. 2, pp. 1197–1202, 2015.

[30] D. J. Late, B. Liu, J. Luo, A. Yan, H. S. S. Matte, M. Grayson, C. N. Rao, and V. P. Dravid, "GaS and GaSe ultrathin layer transistors," *Advanced Materials*, vol. 24, no. 26, pp. 3549–54, 2012.

[31] R. B. Jacobs-Gedrim, M. Shanmugam, N. Jain, C. A. Durcan, M. T. Murphy, T. M. Murray, R. J. Matyi, R. L. Moore, and B. Yu, "Extraordinary photoresponse in two-dimensional In_2Se_3 nanosheets," *ACS Nano*, vol. 8, no. 1, pp. 514–521, 2013.

[32] T. Forster, P. Kruger, and M. Rohlfing, "Two-dimensional topological phases and electronic spectrum of Bi_2Se_3 thin films from GW calculations," *Physical Review B*, vol. 92, no. 20, p. 201404, 2015.

[33] J. D. Wood, S. A. Wells, D. Jariwala, K.-S. Chen, E. Cho, V. K. Sangwan, X. Liu, L. J. Lauhon, T. J. Marks, and M. C. Hersam, "Effective passivation of exfoliated black phosphorus transistors against ambient degradation," *Nano Letters*, vol. 14, no. 12, pp. 6964–6970, 2014.

[34] S. Balendhran, "Devices and systems based on two dimensional MoO_3 and MoS_2," 2013.

[35] D. Xiang, C. Han, J. Zhang, and W. Chen, "Gap states assisted MoO_3 nanobelt photodetector with wide spectrum response," *Scientific Reports*, vol. 4, p. 4891, 2014.

[36] P. Joensen, R. F. Frindt, and S. R. Morrison, "Single-layer MoS_2," *Materials Research Bulletin*, vol. 21, no. 4, pp. 457–461, 1986.

[37] C. Zhang, M. Liu, B. Y. Man, S. Z. Jiang, C. Yang, C. S. Chen, D. J. Feng, D. Bi, F. Y. Liu, H. W. Qiu, and J. X. Zhang, "Facile fabrication of graphene-topological insulator Bi_2Se_3 hybrid dirac materials via chemical vapor deposition in Se-rich conditions," *CrystEngComm*, vol. 16, no. 38, pp. 8941–8945, 2014.

[38] Y.-K. Huang, J. D. Cain, L. Peng, S. Hao, T. Chasapis, M. G. Kanatzidis, C. Wolverton, M. Grayson, and V. P. Dravid, "Evaporative thinning: A facile synthesis method for high quality ultra-thin layers of 2D crystals," *ACS Nano*, 2014.

[39] Y. Zhao, R. W. Hughes, Z. Su, W. Zhou, and D. H. Gregory, "One-step synthesis of bismuth telluride nanosheets of a few quintuple layers in thickness," *Angewandte Chemie International Edition*, vol. 50, no. 44, pp. 10397–10401, 2011.

[40] B. Kumar, D.-H. Lee, S.-H. Kim, B. Yang, S. Maeng, and S.-W. Kim, "General route to single-crystalline SnO nanosheets on arbitrary substrates," *The Journal of Physical Chemistry C*, vol. 114, no. 25, pp. 11050–11055, 2010.

[41] S. Acharya, S. Sarkar, and N. Pradhan, "Subnanometer thin β-indium sulfide nanosheets," *The Journal of Physical Chemistry Letters*, vol. 3, no. 24,

pp. 3812–3817, 2012.

[42] X.-H. Ma, K.-H. Cho, and Y.-M. Sung, "Growth mechanism of vertically aligned SnSe nanosheets via physical vapour deposition," *CrystEngComm*, vol. 16, no. 23, pp. 5080–5086, 2014.

[43] K. Gong, F. Du, Z. Xia, M. Durstock, and L. Dai, "Nitrogen-doped carbon nanotube arrays with high electrocatalytic activity for oxygen reduction," *Science*, vol. 323, no. 5915, pp. 760–764, 2009.

[44] Y. Zhang, Y. Zhang, Q. Ji, J. Ju, H. Yuan, J. Shi, T. Gao, D. Ma, M. Liu, and Y. Chen, "Controlled growth of high-quality monolayer WS_2 layers on sapphire and imaging its grain boundary," *ACS Nano*, vol. 7, no. 10, pp. 8963–8971, 2013.

[45] H. Liu, K. K. Antwi, S. Chua, and D. Chi, "Vapor-phase growth and characterization of $Mo_{(1-x)}W_{(x)}S_2$ ($0 <= x <= 1$) atomic layers on 2-inch sapphire substrates," *Nanoscale*, vol. 6, no. 1, pp. 624–9, 2014.

[46] Q. Ji, Y. Zhang, T. Gao, Y. Zhang, D. Ma, M. Liu, Y. Chen, X. Qiao, P.-H. Tan, M. Kan, J. Feng, Q. Sun, and Z. Liu, "Epitaxial monolayer MoS_2 on mica with novel photoluminescence," *Nano Letters*, vol. 13, no. 8, pp. 3870–7, 2013.

[47] K. Kang, S. Xie, L. Huang, Y. Han, P. Y. Huang, K. F. Mak, C.-J. Kim, D. Muller, and J. Park, "High-mobility three-atom-thick semiconducting films with wafer-scale homogeneity," *Nature*, vol. 520, p. 656, 2015.

[48] E. D. Hanson, F. Shi, T. C. Chasapis, M. G. Kanatzidis, and V. P. Dravid, "Two-dimensional bismuth-rich nanosheets through the evaporative thinning of se-doped Bi_2Te_3," *Journal of Crystal Growth*, vol. 436, pp. 138–144, 2016.

[49] J. D. Cain, E. D. Hanson, and V. P. Dravid, "Controlled synthesis of 2D transition metal dichalcogenide heterostructures and alloys," *Submitted*, 2018.

[50] N. S. Arul and V. D. Nithya, "Molybdenum disulfide quantum dots: synthesis and applications," *RSC Advances*, vol. 6, no. 70, pp. 65670–65682, 2016.

[51] D. Kiriya, M. Tosun, P. Zhao, J. S. Kang, and A. Javey, "Air-stable surface charge transfer doping of MoS_2 by benzyl viologen," *Journal of the American Chemical Society*, vol. 136, no. 22, pp. 7853–7856, 2014.

[52] H. Li, X. Duan, X. Wu, X. Zhuang, H. Zhou, Q. Zhang, X. Zhu, W. Hu, P. Ren, and P. Guo, "Growth of alloy $MoS_{2x}Se_{2(1-x)}$ nanosheets with fully tunable chemical compositions and optical properties," *Journal of the American Chemical Society*, vol. 136, no. 10, pp. 3756–3759, 2014.

[53] Z. Lin, M. T. Thee, A. L. Elas, S. Feng, C. Zhou, K. Fujisawa, N. Perea-Lopez, V. Carozo, H. Terrones, and M. Terrones, "Facile synthesis of MoS_2 and $Mo_xW_{1-x}S_2$ triangular monolayers," *APL Materials*, vol. 2, no. 9, p. 092514, 2014.

[54] J. J. Cha, D. Kong, S.-S. Hong, J. G. Analytis, K. Lai, and Y. Cui, "Weak antilocalization in $Bi_2(Se_xTe_{1-x})_3$ nanoribbons and nanoplates," *Nano Letters*, vol. 12, no. 2, pp. 1107–1111, 2012.

[55] J. Suh, T.-E. Park, D.-Y. Lin, D. Fu, J. Park, H. J. Jung, Y. Chen, C. Ko, C. Jang, Y. Sun, R. Sinclair, J. Chang, S. Tongay, and J. Wu, "Doping against the native propensity of MoS_2: Degenerate hole doping by cation substitution," *Nano Letters*, vol. 14, no. 12, pp. 6976–6982, 2014.

[56] K. Zhang, S. Feng, J. Wang, A. Azcatl, N. Lu, R. Addou, N. Wang, C. Zhou, J. Lerach, and V. Bojan, "Manganese doping of monolayer MoS_2: the substrate is critical," *Nano Letters*, vol. 15, no. 10, pp. 6586–6591, 2015.

[57] V. Nicolosi, M. Chhowalla, M. G. Kanatzidis, M. S. Strano, and J. N. Coleman, "Liquid exfoliation of layered materials," *Science*, vol. 340, no. 6139, p. 1226419, 2013.

[58] Q. Li, Z. Yao, J. Wu, S. Mitra, S. Hao, T. S. Sahu, Y. Li, C. Wolverton, and V. P. Dravid, "Intermediate phases in sodium intercalation into MoS_2 nanosheets and their implications for sodium-ion batteries," *Nano Energy*, vol. 38, no. Supplement C, pp. 342–349, 2017.

[59] R. Kappera, D. Voiry, S. E. Yalcin, B. Branch, G. Gupta, A. D. Mohite, and M. Chhowalla, "Phase-engineered low-resistance contacts for ultrathin MoS_2 transistors," *Nature Materials*, vol. 13, no. 12, pp. 1128–1134, 2014.

[60] A. L. Friedman, F. K. Perkins, A. T. Hanbicki, J. C. Culbertson, and P. M. Campbell, "Dynamics of chemical vapor sensing with MoS_2 using 1T/2H phase contacts/channel," *Nanoscale*, vol. 8, no. 22, pp. 11445–11453, 2016.

[61] Y. Ma, B. Liu, A. Zhang, L. Chen, M. Fathi, C. Shen, A. N. Abbas, M. Ge, M. Mecklenburg, and C. Zhou, "Reversible semiconducting-to-metallic phase transition in chemical vapor deposition grown monolayer WSe_2 and applications for devices," *ACS Nano*, vol. 9, no. 7, pp. 7383–7391, 2015.

[62] M. Alsaif, K. Latham, M. R. Field, D. D. Yao, N. V. Medehkar, G. A. Beane, R. B. Kaner, S. P. Russo, J. Z. Ou, and K. Kalantar-zadeh, "Tunable plasmon resonances in two-dimensional molybdenum oxide nanoflakes," *Advanced Materials*, vol. 26, no. 23, pp. 3931–3937, 2014.

[63] S. Lei, X. Wang, B. Li, J. Kang, Y. He, A. George, L. Ge, Y. Gong, P. Dong, and Z. Jin, "Surface functionalization of two-dimensional metal chalcogenides by lewis acid-base chemistry," *Nature Nanotechnology*, vol. 11, no. 5, pp. 465–471, 2016.

[64] S. S. Chou, Y.-K. Huang, J. Kim, B. Kaehr, B. M. Foley, P. Lu, C. Dykstra, P. E. Hopkins, C. J. Brinker, J. Huang, and V. P. Dravid, "Controlling the metal to semiconductor transition of MoS_2 and WS_2 in solution," *Journal of the American Chemical Society*, vol. 137, no. 5, pp. 1742–1745, 2015.

[65] S. S. Chou, M. De, J. Kim, S. Byun, C. Dykstra, J. Yu, J. Huang, and V. P. Dravid, "Ligand conjugation of chemically exfoliated MoS_2," *Journal of the American Chemical Society*, vol. 135, no. 12, pp. 4584–4587, 2013.

[66] B. Xu, Y. Su, L. Li, R. Liu, and Y. Lv, "Thiol-functionalized single-layered MoS_2 nanosheet as a photoluminescence sensing platform via charge transfer for dopamine detection," *Sensors and Actuators B: Chemical*, vol. 246, pp. 380–388, 2017.

[67] X. Zhang, Z. Shao, X. Zhang, Y. He, and J. Jie, "Surface charge transfer doping of low-dimensional nanostructures toward high-performance nanodevices," *Advanced Materials*, vol. 28, no. 47, pp. 10409–10442, 2016.

[68] K. K. Kim, J. J. Bae, H. K. Park, S. M. Kim, H.-Z. Geng, K. A. Park, H.-J. Shin, S.-M. Yoon, A. Benayad, and J.-Y. Choi, "Fermi level engineering of single-walled carbon nanotubes by $AuCl_3$ doping," *Journal of the American Chemical Society*, vol. 130, no. 38, pp. 12757–12761, 2008.

[69] D.-C. Choi, M. Kim, Y. J. Song, S. Hussain, W.-S. Song, K.-S. An, and J. Jung, "Selective $AuCl_3$ doping of graphene for reducing contact resistance of graphene devices," *Applied Surface Science*, vol. 427, pp. 48–54, 2018.

[70] K. K. Kim, A. Reina, Y. Shi, H. Park, L.-J. Li, Y. H. Lee, and J. Kong, "Enhancing the conductivity of transparent graphene films via doping," *Nanotechnology*, vol. 21, no. 28, p. 285205, 2010.

[71] M. S. Choi, D. Qu, D. Lee, X. Liu, K. Watanabe, T. Taniguchi, and W. J. Yoo, "Lateral MoS_2 p-n junction formed by chemical doping for use in high-performance optoelectronics," *ACS Nano*, vol. 8, no. 9, pp. 9332–9340, 2014.

[72] H.-M. Li, D. Lee, D. Qu, X. Liu, J. Ryu, A. Seabaugh, and W. J. Yoo, "Ultimate thin vertical p-n junction composed of two-dimensional layered molybdenum disulfide," *Nature Communications*, vol. 6, 2015.

[73] X. Liu, D. Qu, J. Ryu, F. Ahmed, Z. Yang, D. Lee, and W. J. Yoo, "P-type polar transition of chemically doped multilayer MoS_2 transistor," *Advanced Materials*, vol. 28, no. 12, pp. 2345–2351, 2016.

[74] S. Mouri, Y. Miyauchi, and K. Matsuda, "Tunable photoluminescence of monolayer MoS_2 via chemical doping," *Nano Letters*, vol. 13, no. 12, pp. 5944–5948, 2013.

[75] A. Tarasov, S. Zhang, M.-Y. Tsai, P. M. Campbell, S. Graham, S. Barlow, S. R. Marder, and E. M. Vogel, "Controlled doping of large-area trilayer MoS_2 with molecular reductants and oxidants," *Advanced Materials*, vol. 27, no. 7, pp. 1175–1181, 2015.

[76] J. Wang, A. Hewitt, R. Kumar, J. Boltersdorf, T. Guan, F. Hunte, P. Maggard, J. Brom, J. Redwing, and D. Dougherty, "Molecular doping control at a topological insulator surface: F4-TCNQ on Bi_2Se_3," *The Journal of Physical Chemistry C*, vol. 118, no. 27, pp. 14860–14865, 2014.

[77] D. Kim, S. Cho, N. P. Butch, P. Syers, K. Kirshenbaum, S. Adam, J. Paglione, and M. S. Fuhrer, "Surface conduction of topological dirac electrons in bulk insulating Bi_2Se_3," *Nature Physics*, vol. 8, no. 6, pp. 459–463, 2012.

[78] P. Sessi, T. Bathon, K. A. Kokh, O. E. Tereshchenko, and M. Bode, "Probing the electronic properties of individual MnPc molecules coupled to topological states," *Nano Letters*, vol. 14, no. 9, pp. 5092–5096, 2014.

[79] Y. Xia, D. Qian, D. Hsieh, L. Wray, A. Pal, H. Lin, A. Bansil, D. Grauer, Y. S. Hor, R. J. Cava, and M. Z. Hasan, "Observation of a large-gap topological-insulator class with a single dirac cone on the surface," *Nature Physics*, vol. 5, no. 6, pp. 398–402, 2009.

[80] H. Zhang, C.-X. Liu, X.-L. Qi, X. Dai, Z. Fang, and S.-C. Zhang, "Topological insulators in Bi_2Se_3, Bi_2Te_3 and Sb_2Te_3 with a single dirac cone on the surface," *Nature Physics*, vol. 5, no. 6, pp. 438–442, 2009.

[81] J. E. Moore, "The birth of topological insulators," *Nature*, vol. 464, no. 7286, pp. 194–198, 2010.

[82] D. O. Scanlon, P. D. C. King, R. P. Singh, A. De La Torre, S. M. Walker, G. Balakrishnan, F. Baumberger, and C. R. A. Catlow, "Controlling bulk conductivity in topological insulators: Key role of antisite defects," *Advanced Materials*, vol. 24, no. 16, pp. 2154–2158, 2012.

[83] L. Ren, X. Qi, Y. Liu, G. Hao, Z. Huang, X. Zou, L. Yang, J. Li, and J. Zhong, "Large-scale production of ultrathin topological insulator bismuth telluride

nanosheets by a hydrothermal intercalation and exfoliation route," *Journal of Materials Chemistry*, vol. 22, no. 11, pp. 4921–4926, 2012.

[84] Y. Min, J. W. Roh, H. Yang, M. Park, S. I. Kim, S. Hwang, S. M. Lee, K. H. Lee, and U. Jeong, "Surfactant free scalable synthesis of Bi_2Te_3 and Bi_2Se_3 nanoflakes and enhanced thermoelectric properties of their nanocomposites," *Advanced Materials*, vol. 25, no. 10, pp. 1425–1429, 2013.

[85] H. Peng, K. Lai, D. Kong, S. Meister, Y. Chen, X.-L. Qi, S.-C. Zhang, Z.-X. Shen, and Y. Cui, "Aharonov-bohm interference in topological insulator nanoribbons," *Nature Materials*, vol. 9, no. 3, pp. 225–229, 2010.

[86] X. Wang, Y. Du, S. Dou, and C. Zhang, "Room temperature giant and linear magnetoresistance in topological insulator Bi_2Te_3 nanosheets," *Physical Review Letters*, vol. 108, no. 26, p. 266806, 2012.

[87] X. Chen, X.-C. Ma, K. He, J.-F. Jia, and Q.-K. Xue, "Molecular beam epitaxial growth of topological insulators," *Advanced Materials*, vol. 23, no. 9, pp. 1162–1165, 2011.

[88] Z. Ren, A. A. Taskin, S. Sasaki, K. Segawa, and Y. Ando, "Large bulk resistivity and surface quantum oscillations in the topological insulator Bi_2Te_2Se," *Physical Review B*, vol. 82, no. 24, p. 241306, 2010.

[89] S. S. Hong, W. Kundhikanjana, J. J. Cha, K. Lai, D. Kong, S. Meister, M. A. Kelly, Z.-X. Shen, and Y. Cui, "Ultrathin topological insulator Bi_2Se_3 nanoribbons exfoliated by atomic force microscopy," *Nano Letters*, vol. 10, no. 8, pp. 3118–3122, 2010.

[90] Y. Ando, "Topological insulator materials," *Journal of the Physical Society of Japan*, vol. 82, no. 10, p. 102001, 2013.

[91] Z. Wang, R. L. J. Qiu, C. H. Lee, Z. Zhang, and X. P. A. Gao, "Ambipolar surface conduction in ternary topological insulator $Bi_2(Te_{1-x}Se_x)_3$ nanoribbons," *ACS Nano*, vol. 7, no. 3, pp. 2126–2131, 2013.

[92] K. C. Mills, *Thermodynamic Data for Inorganic Sulphides, Selenides and Tellurides*. Butterworths, 1974.

[93] J. W. G. Bos, H. W. Zandbergen, M. H. Lee, N. P. Ong, and R. J. Cava, "Structures and thermoelectric properties of the infinitely adaptive series $(Bi_2)_m(Bi_2Te_3)_n$," *Physical Review B*, vol. 75, no. 19, p. 195203, 2007.

[94] P. M. Imamov and S. Semiletov, "The crystal structure of the phases in the systems Bi-Se, Bi-Te, and Sb-Te," *Soviet Physics - Crystallography*, vol. 15, no. 5, p. 972, 1970.

[95] H. Lind, S. Lidin, and U. Haeussermann, "Structure and bonding properties of $(Bi_2Se_3)m(Bi_2)n$ stacks by first-principles density functional theory," *Physical Review B*, vol. 72, no. 18, p. 184101, 2005.

[96] D. Briggs, A. Brown, and J. C. Vickerman, *Handbook of Static Secondary Ion Mass Spectrometry*. Wiley Chichester etc, 1989.

[97] A. Benninghoven, "Chemical analysis of inorganic and organic surfaces and thin films by static time-of-flight secondary ion mass spectrometry (TOF-SIMS)," *Angewandte Chemie International Edition in English*, vol. 33, no. 10, pp. 1023–1043, 1994.

[98] E. D. Hanson, L. Lajaunie, S. Hao, B. D. Myers, F. Shi, A. A. Murthy, C. Wolverton, R. Arenal, and V. P. Dravid, "Systematic study of oxygen vacancy tunable transport properties of few-layer MoO_{3-x} enabled by vapor-based synthesis," *Advanced Functional Materials*, vol. 27, no. 17, p. 1605380, 2017.

[99] R. Naouel, H. Dhaouadi, F. Touati, and N. Gharbi, "Synthesis and electrical properties of well-ordered layered α-MoO_3 nanosheets," *Nano-Micro Letters*, vol. 3, no. 4, pp. 242–248, 2011.

[100] M. Vasilopoulou, A. M. Douvas, D. G. Georgiadou, L. C. Palilis, S. Kennou, L. Sygellou, A. Soultati, I. Kostis, G. Papadimitropoulos, and D. Davazoglou, "The influence of hydrogenation and oxygen vacancies on molybdenum oxides work function and gap states for application in organic optoelectronics," *Journal of the American Chemical Society*, vol. 134, no. 39, pp. 16178–16187, 2012.

[101] K. W. Harrison, C. D. Corolewski, M. D. McCluskey, J. Lindemuth, S. Ha, and M. G. Norton, "Electronic transport in molybdenum dioxide thin films," *Journal of Materials Science: Materials in Electronics*, vol. 26, no. 12, pp. 9717–9720, 2015.

[102] S. Cong, T. Sugahara, T. Wei, J. Jiu, Y. Hirose, S. Nagao, and K. Suganuma, "Diverse adsorption/desorption abilities originating from the nanostructural morphology of VOC gas sensing devices based on molybdenum trioxide nanorod arrays," *Advanced Materials Interfaces*, vol. 3, no. 14, 2016.

[103] L. Zhou, L. Yang, P. Yuan, J. Zou, Y. Wu, and C. Yu, "α-MoO_3 nanobelts: a high performance cathode material for lithium ion batteries," *The Journal of Physical Chemistry C*, vol. 114, no. 49, pp. 21868–21872, 2010.

[104] A. Guerfi, R. W. Paynter, and L. H. Dao, "Characterization and stability of electrochromic MoO_3 thin films prepared by electrodeposition," *Journal of The Electrochemical Society*, vol. 142, no. 10, pp. 3457–3464, 1995.

[105] C. Battaglia, X. Yin, M. Zheng, I. D. Sharp, T. Chen, S. McDonnell, A. Azcatl, C. Carraro, B. Ma, and R. Maboudian, "Hole selective MoO_x contact for silicon solar cells," *Nano Letters*, vol. 14, no. 2, pp. 967–971, 2014.

[106] M. T. Greiner, L. Chai, M. G. Helander, W.-M. Tang, and Z.-H. Lu, "Metal-metal oxide interfaces: how metal contacts affect the work function and band structure of MoO_3," *Advanced Functional Materials*, vol. 23, no. 2, pp. 215–226, 2013.

[107] S. Hofle, H. Do, E. Mankel, M. Pfaff, Z. Zhang, D. Bahro, T. Mayer, W. Jaegermann, D. Gerthsen, and C. Feldmann, "Molybdenum oxide anode buffer layers for solution processed, blue phosphorescent small molecule organic light emitting diodes," *Organic Electronics*, vol. 14, no. 7, pp. 1820–1824, 2013.

[108] M. M. Y. A. Alsaif, A. F. Chrimes, T. Daeneke, S. Balendhran, D. O. Bellisario, Y. Son, M. R. Field, W. Zhang, H. Nili, E. P. Nguyen, K. Latham, J. van Embden, M. S. Strano, J. Z. Ou, and K. Kalantar-zadeh, "High-performance field effect transistors using electronic inks of 2D molybdenum oxide nanoflakes," *Advanced Functional Materials*, vol. 26, no. 1, pp. 91–100, 2016.

[109] Z. Chen, I. Santoso, R. Wang, L. F. Xie, H. Y. Mao, H. Huang, Y. Z. Wang, X. Y. Gao, Z. K. Chen, and D. Ma, "Surface transfer hole doping of epitaxial graphene using MoO_3 thin film," *Applied Physics Letters*, vol. 96, no. 21, p. 213104, 2010.

[110] K. Kalantar-Zadeh, J. Tang, M. Wang, K. L. Wang, A. Shailos, K. Galatsis, R. Kojima, V. Strong, A. Lech, and W. Wlodarski, "Synthesis of nanometre-thick MoO_3 sheets," *Nanoscale*, vol. 2, no. 3, pp. 429–433, 2010.

[111] H. Bai, W. Yi, J. Li, G. Xi, Y. Li, H. Yang, and J. Liu, "Direct growth of defect-rich MoO_{3-x} ultrathin nanobelts for efficiently catalyzed conversion of isopropyl alcohol to propylene under visible light," *Journal of Materials Chemistry A*, vol. 4, no. 5, pp. 1566–1571, 2016.

[112] D. J. Late, B. Liu, H. Matte, C. Rao, and V. P. Dravid, "Rapid characterization of ultrathin layers of chalcogenides on SiO_2/Si substrates," *Advanced Functional Materials*, vol. 22, no. 9, pp. 1894–1905, 2012.

[113] D. E. Diaz-Droguett, A. Zuniga, G. Solorzano, and V. Fuenzalida, "Electron beam-induced structural transformations of MoO_3 and MoO_{3-x} crystalline nanostructures," *Journal of Nanoparticle Research*, vol. 14, no. 1, pp. 1–9, 2012.

[114] D. Wang, D. S. Su, and R. Schlogl, "Electron beam induced transformation of MoO_3 to MoO_2 and a new phase MoO," *Zeitschrift fur anorganische und allgemeine Chemie*, vol. 630, no. 7, pp. 1007–1014, 2004.

[115] F. Banhart, *In-situ electron microscopy at high resolution*. Singapore: World Scientific, 2008.

[116] A. Krasheninnikov and K. Nordlund, "Ion and electron irradiation-induced effects in nanostructured materials," *Journal of applied physics*, vol. 107, no. 7, p. 071301, 2010.

[117] J. W. Rabalais, R. J. Colton, and A. M. Guzman, "Trapped electrons in substoichiometric MoO_3 observed by x-ray electron spectroscopy," *Chemical Physics Letters*, vol. 29, no. 1, pp. 131–133, 1974.

[118] D. O. Scanlon, G. W. Watson, D. Payne, G. Atkinson, R. Egdell, and D. Law, "Theoretical and experimental study of the electronic structures of MoO_3 and MoO_2," *The Journal of Physical Chemistry C*, vol. 114, no. 10, pp. 4636–4645, 2010.

[119] K. Inzani, T. Grande, F. Vullum-Bruer, and S. M. Selbach, "A van der waals density functional study of MoO_3 and its oxygen vacancies," *The Journal of Physical Chemistry C*, vol. 120, no. 16, pp. 8959–8968, 2016.

[120] R. Coquet and D. J. Willock, "The (010) surface of α-MoO_3, a DFT + U study," *Physical Chemistry Chemical Physics*, vol. 7, no. 22, pp. 3819–3828, 2005.

[121] M. Cahay, "Quantum confinement vi: Nanostructured materials and devices: Proceedings of the international symposium," The Electrochemical Society.

[122] W. Xie, M. Su, Z. Zheng, Y. Wang, L. Gong, F. Xie, W. Zhang, Z. Luo, J. Y. Luo, and P. Liu, "Nanoscale insights into the hydrogenation process of layered α-MoO_3," *ACS Nano*, vol. 10, no. 1, pp. 1662–1670, 2016.

[123] M. Camacho-Lopez, L. Escobar-Alarcon, M. Picquart, R. Arroyo, G. Cordoba, and E. Haro-Poniatowski, "Micro-raman study of the m-MoO_2 to a-MoO_3 transformation induced by cw-laser irradiation," *Optical Materials*, vol. 33, no. 3, pp. 480–484, 2011.

[124] A. J. Molina-Mendoza, J. L. Lado, J. O. Island, M. A. Nino, L. Aballe, M. Foerster, F. Y. Bruno, A. Lopez-Moreno, L. Vaquero-Garzon, H. S. J. van der Zant, G. Rubio-Bollinger, N. Agrait, E. M. Prez, J. Fernandez-Rossier, and A. Castellanos-Gomez, "Centimeter-scale synthesis of ultrathin layered MoO_3 by van der waals epitaxy," *Chemistry of Materials*, vol. 28, no. 11, pp. 4042–4051,

2016.

[125] C. Julien and G. A. Nazri, "Transport properties of lithium-intercalated MoO_3," *Solid State Ionics*, vol. 68, no. 1-2, pp. 111–116, 1994.

[126] J. Z. Ou, J. L. Campbell, D. Yao, W. Wlodarski, and K. Kalantar-Zadeh, "In situ raman spectroscopy of H_2 gas interaction with layered MoO_3," *The Journal of Physical Chemistry C*, vol. 115, no. 21, pp. 10757–10763, 2011.

[127] L. Lajaunie, F. Boucher, R. Dessapt, and P. Moreau, "Strong anisotropic influence of local-field effects on the dielectric response of $\alpha - MoO_3$," *Physical Review B*, vol. 88, no. 11, p. 115141, 2013.

[128] G. A. Botton, C. C. Appel, A. Horsewell, and W. M. Stobbs, "Quantification of the EELS near-edge structures to study Mn doping in oxides," *Journal of Microscopy*, vol. 180, no. 3, pp. 211–216, 1995.

[129] L. Lajaunie, F. Boucher, R. Dessapt, and P. Moreau, "Quantitative use of electron energy-loss spectroscopy $Mo - M_{2,3}$ edges for the study of molybdenum oxides," *Ultramicroscopy*, vol. 149, pp. 1–8, 2015.

[130] R. F. Egerton, P. Li, and M. Malac, "Radiation damage in the tem and sem," *Micron*, vol. 35, no. 6, pp. 399–409, 2004.

[131] H. A. Tahini, X. Tan, S. N. Lou, J. Scott, R. Amal, Y. H. Ng, and S. C. Smith, "Mobile polaronic states in α-MoO_3: An ab initio investigation of the role of oxygen vacancies and alkali ions," *ACS Applied Materials and Interfaces*, vol. 8, no. 17, pp. 10911–10917, 2016.

[132] R. Arenal, F. De la Pena, O. Stephan, M. Walls, M. Tence, A. Loiseau, and C. Colliex, "Extending the analysis of EELS spectrum-imaging data, from elemental to bond mapping in complex nanostructures," *Ultramicroscopy*, vol. 109, no. 1, pp. 32–38, 2008.

[133] C. Jeanguillaume and C. Colliex, "Spectrum-image: the next step in EELS digital acquisition and processing," *Ultramicroscopy*, vol. 28, no. 1, pp. 252–257, 1989.

[134] F. De la Pena, P. Burdet, T. Ostasevicius, M. Sarahan, M. Nprd, V. Taillon, A. Eljarrat, S. Mazzucco, G. Donvail, L. F. Zagonel, M. Walls, and I. Iyengar, "Hyperspy: multidimensional data analysis toolbox," 2015.

[135] R. F. Egerton, *Electron energy-loss spectroscopy in the electron microscope*. Springer Science and Business Media, 2011.

[136] K. Iakoubovskii, K. Mitsuishi, Y. Nakayama, and K. Furuya, "Thickness measurements with electron energy loss spectroscopy," *Microscopy Research and Technique*, vol. 71, no. 8, pp. 626–631, 2008.

[137] J. Park, S. Heo, J.-G. Chung, H. Kim, H. Lee, K. Kim, and G.-S. Park, "Bandgap measurement of thin dielectric films using monochromated STEM-EELS," *Ultramicroscopy*, vol. 109, no. 9, pp. 1183–1188, 2009.

[138] R. Arenal, O. Stephan, M. Kociak, D. Taverna, A. Loiseau, and C. Colliex, "Electron energy loss spectroscopy measurement of the optical gaps on individual boron nitride single-walled and multiwalled nanotubes," *Physical Review Letters*, vol. 95, no. 12, p. 127601, 2005.

[139] P. Ewels, T. Sikora, V. Serin, C. P. Ewels, and L. Lajaunie, "A complete overhaul of the electron energy-loss spectroscopy and x-ray absorption spectroscopy database: eelsdb. eu," *Microscopy and Microanalysis*, vol. 22, p. 717, 2016.

[140] G. Kresse and J. Furthmuller, "Efficient iterative schemes for ab initio total-energy calculations using a plane-wave basis set," *Physical Review B*, vol. 54, no. 16, p. 11169, 1996.

[141] L. Kihlborg, "Least squares refinement of crystal structure of molybdenum trioxide," *Arkiv for Kemi*, vol. 21, no. 4, p. 357, 1963.

[142] S. Grimme, "Semiempirical GGA-type density functional constructed with a long-range dispersion correction," *Journal of Computational Chemistry*, vol. 27, no. 15, pp. 1787–1799, 2006.

[143] J. P. Perdew, K. Burke, and M. Ernzerhof, "Generalized gradient approximation made simple," *Physical Review Letters*, vol. 77, no. 18, p. 3865, 1996.

[144] S. Grindy, B. Meredig, S. Kirklin, J. E. Saal, and C. Wolverton, "Approaching chemical accuracy with density functional calculations: Diatomic energy corrections," *Physical Review B*, vol. 87, no. 7, p. 075150, 2013.

[145] G. K. Madsen and D. J. Singh, "Boltztrap. a code for calculating band-structure dependent quantities," *Computer Physics Communications*, vol. 175, no. 1, pp. 67–71, 2006.

[146] Z. Jin, J. Yao, C. Kittrell, and J. M. Tour, "Large-scale growth and characterizations of nitrogen-doped monolayer graphene sheets," *ACS Nano*, vol. 5, no. 5, pp. 4112–4117, 2011.

[147] G. H. Han, N. J. Kybert, C. H. Naylor, B. S. Lee, J. Ping, J. H. Park, J. Kang, S. Y. Lee, Y. H. Lee, and R. Agarwal, "Seeded growth of highly crystalline molybdenum disulphide monolayers at controlled locations," *Nature Communications*, vol. 6, p. 6128, 2015.

[148] Y. Li, J. D. Cain, E. D. Hanson, A. A. Murthy, S. Hao, F. Shi, Q. Li, C. Wolverton, X. Chen, and V. P. Dravid, "Au@MoS_2 core-shell heterostructures with strong light-matter interactions," *Nano Letters*, vol. 16, no. 12, pp. 7696–7702, 2016.

[149] D. Jariwala, V. K. Sangwan, L. J. Lauhon, T. J. Marks, and M. C. Hersam, "Emerging device applications for semiconducting two-dimensional transition metal dichalcogenides," *ACS Nano*, vol. 8, no. 2, pp. 1102–1120, 2014.

[150] W. Zhang, J.-K. Huang, C.-H. Chen, Y.-H. Chang, Y.-J. Cheng, and L.-J. Li, "High-gain phototransistors based on a cvd MoS_2 monolayer," *Advanced Materials*, vol. 25, no. 25, pp. 3456–3461, 2013.

[151] D. J. Late, Y.-K. Huang, B. Liu, J. Acharya, S. N. Shirodkar, J. Luo, A. Yan, D. Charles, U. V. Waghmare, and V. P. Dravid, "Sensing behavior of atomically thin-layered MoS_2 transistors," *ACS Nano*, vol. 7, no. 6, pp. 4879–4891, 2013.

[152] A. Splendiani, L. Sun, Y. Zhang, T. Li, J. Kim, C.-Y. Chim, G. Galli, and F. Wang, "Emerging photoluminescence in monolayer MoS_2," *Nano Letters*, vol. 10, no. 4, pp. 1271–1275, 2010.

[153] J. Heising and M. G. Kanatzidis, "Structure of restacked MoS_2 and WS_2 elucidated by electron crystallography," *Journal of the American Chemical Society*, vol. 121, no. 4, pp. 638–643, 1999.

[154] J. Heising and M. G. Kanatzidis, "Exfoliated and restacked MoS_2 and WS_2: Ionic or neutral species? encapsulation and ordering of hard electropositive cations," *Journal of the American Chemical Society*, vol. 121, no. 50, pp. 11720–11732, 1999.

[155] B. Ouyang, G. Lan, Y. Guo, Z. Mi, and J. Song, "Phase engineering of monolayer transition-metal dichalcogenide through coupled electron doping and lattice deformation," *Applied Physics Letters*, vol. 107, no. 19, p. 191903, 2015.

[156] B. Ouyang, Z. Mi, and J. Song, "Bandgap transition of 2H transition metal dichalcogenides: Predictive tuning via inherent interface coupling and strain," *The Journal of Physical Chemistry C*, vol. 120, no. 16, pp. 8927–8935, 2016.

[157] D. B. Putungan, S.-H. Lin, and J.-L. Kuo, "A first-principles examination of conducting monolayer 1T'-MX_2 (M = Mo, W; X = S, Se, Te): promising catalysts

for hydrogen evolution reaction and its enhancement by strain," *Physical Chemistry Chemical Physics*, vol. 17, no. 33, pp. 21702–21708, 2015.

[158] B. Evans and R. Hazelwood, "Optical and structural properties of $MoSe_2$," *physica status solidi (a)*, vol. 4, no. 1, pp. 181–192, 1971.

[159] R. Gordon, D. Yang, E. Crozier, D. Jiang, and R. Frindt, "Structures of exfoliated single layers of WS_2, MoS_2, and $MoSe_2$ in aqueous suspension," *Physical Review B*, vol. 65, no. 12, p. 125407, 2002.

[160] M. S. Whittingham and F. R. Gamble, "The lithium intercalates of the transition metal dichalcogenides," *Materials Research Bulletin*, vol. 10, no. 5, pp. 363–371, 1975.

[161] A. Ambrosi, Z. Sofer, and M. Pumera, "2H-1T phase transition and hydrogen evolution activity of MoS_2, $MoSe_2$, WS_2 and WSe_2 strongly depends on the MX_2 composition," *Chemical Communications*, vol. 51, no. 40, pp. 8450–8453, 2015.

[162] S. Larentis, B. Fallahazad, and E. Tutuc, "Field-effect transistors and intrinsic mobility in ultra-thin $MoSe_2$ layers," *Applied Physics Letters*, vol. 101, no. 22, p. 223104, 2012.

[163] D. Voiry, A. Mohite, and M. Chhowalla, "Phase engineering of transition metal dichalcogenides," *Chemical Society Reviews*, vol. 44, no. 9, pp. 2702–2712, 2015.

[164] R. Kappera, D. Voiry, S. E. Yalcin, W. Jen, M. Acerce, S. Torrel, B. Branch, S. Lei, W. Chen, and S. Najmaei, "Metallic 1T phase source/drain electrodes for field effect transistors from chemical vapor deposited MoS_2," *APL Materials*, vol. 2, no. 9, p. 092516, 2014.

[165] S. Cho, S. Kim, J. H. Kim, J. Zhao, J. Seok, D. H. Keum, J. Baik, D.-H. Choe, K. Chang, and K. Suenaga, "Phase patterning for ohmic homojunction contact in $MoTe_2$," *Science*, vol. 349, no. 6248, pp. 625–628, 2015.

[166] G. Eda, T. Fujita, H. Yamaguchi, D. Voiry, M. Chen, and M. Chhowalla, "Coherent atomic and electronic heterostructures of single-layer MoS_2," *ACS Nano*, vol. 6, no. 8, pp. 7311–7317, 2012.

[167] K.-A. N. Duerloo, Y. Li, and E. J. Reed, "Structural phase transitions in two-dimensional Mo- and W-dichalcogenide monolayers," *Nature Communications*, vol. 5, 2014.

[168] M. Naz, T. Hallam, N. C. Berner, N. McEvoy, R. Gatensby, J. B. McManus, Z. Akhter, and G. S. Duesberg, "A new 2H-2H'/1T cophase in polycrystalline

MoS_2 and $MoSe_2$ thin films," *ACS Applied Materials and Interfaces*, vol. 8, no. 45, pp. 31442–31448, 2016.

[169] J. S. Kim, J. Kim, J. Zhao, S. Kim, J. H. Lee, Y. Jin, H. Choi, B. H. Moon, J. J. Bae, Y. H. Lee, and S. C. Lim, "Electrical transport properties of polymorphic MoS_2," *ACS Nano*, vol. 10, no. 8, pp. 7500–7506, 2016.

[170] S. Jimnez Sandoval, D. Yang, R. F. Frindt, and J. C. Irwin, "Raman study and lattice dynamics of single molecular layers of MoS_2," *Physical Review B*, vol. 44, no. 8, pp. 3955–3962, 1991.

[171] M. Calandra, "Chemically exfoliated single-layer MoS_2: Stability, lattice dynamics, and catalytic adsorption from first principles," *Physical Review B*, vol. 88, no. 24, p. 245428, 2013.

[172] U. Gupta, B. S. Naidu, U. Maitra, A. Singh, S. N. Shirodkar, U. V. Waghmare, and C. N. R. Rao, "Characterization of few-layer 1T-$MoSe_2$ and its superior performance in the visible-light induced hydrogen evolution reaction," *APL Materials*, vol. 2, no. 9, p. 092802, 2014.

[173] X. Wang, Y. Gong, G. Shi, W. L. Chow, K. Keyshar, G. Ye, R. Vajtai, J. Lou, Z. Liu, E. Ringe, B. K. Tay, and P. M. Ajayan, "Chemical vapor deposition growth of crystalline monolayer $MoSe_2$," *ACS Nano*, vol. 8, no. 5, pp. 5125–5131, 2014.

[174] K. Wang, Y. Feng, C. Chang, J. Zhan, C. Wang, Q. Zhao, J. N. Coleman, L. Zhang, W. J. Blau, and J. Wang, "Broadband ultrafast nonlinear absorption and nonlinear refraction of layered molybdenum dichalcogenide semiconductors," *Nanoscale*, vol. 6, no. 18, pp. 10530–10535, 2014.

[175] A. Carvalho, R. M. Ribeiro, and A. H. Castro Neto, "Band nesting and the optical response of two-dimensional semiconducting transition metal dichalcogenides," *Physical Review B*, vol. 88, no. 11, p. 115205, 2013.

[176] Y. Zheng, Y. Huang, H. Shu, X. Zhou, J. Ding, X. Chen, and W. Lu, "The effect of lithium adsorption on the formation of 1T-MoS_2 phase based on first-principles calculation," *Physics Letters A*, vol. 380, no. 20, pp. 1767–1771, 2016.

[177] A. Singh, S. N. Shirodkar, and U. V. Waghmare, "1H and 1T polymorphs, structural transitions and anomalous properties of $(Mo, W)(S, Se)_2$ monolayers: first-principles analysis," *2D Materials*, vol. 2, no. 3, p. 035013, 2015.

[178] G. Gao, Y. Jiao, F. Ma, Y. Jiao, E. Waclawik, and A. Du, "Charge mediated semiconducting-to-metallic phase transition in molybdenum disulfide monolayer and hydrogen evolution reaction in new 1T' phase," *The Journal of Physical*

Chemistry C, vol. 119, no. 23, pp. 13124–13128, 2015.

[179] J. P. Perdew and Y. Wang, "Accurate and simple analytic representation of the electron-gas correlation energy," *Physical Review B*, vol. 45, no. 23, p. 13244, 1992.

[180] G. Kresse and J. Hafner, "Ab initio molecular dynamics for liquid metals," *Physical Review B*, vol. 47, no. 1, p. 558, 1993.

[181] G. Kresse and J. Furthmuller, "Efficiency of ab-initio total energy calculations for metals and semiconductors using a plane-wave basis set," *Computational Materials Science*, vol. 6, no. 1, pp. 15–50, 1996.

[182] P. E. Blochl, "Projector augmented-wave method," *Physical review B*, vol. 50, no. 24, p. 17953, 1994.

[183] G. Kresse and D. Joubert, "From ultrasoft pseudopotentials to the projector augmented-wave method," *Physical Review B*, vol. 59, no. 3, p. 1758, 1999.

[184] G. Henkelman, B. P. Uberuaga, and H. Jonsson, "A climbing image nudged elastic band method for finding saddle points and minimum energy paths," *The Journal of chemical physics*, vol. 113, no. 22, pp. 9901–9904, 2000.

[185] D. Liu, Y. Guo, L. Fang, and J. Robertson, "Sulfur vacancies in monolayer MoS_2 and its electrical contacts," *Applied Physics Letters*, vol. 103, no. 18, p. 183113, 2013.

[186] N. Kaushik, A. Nipane, F. Basheer, S. Dubey, S. Grover, M. M. Deshmukh, and S. Lodha, "Schottky barrier heights for Au and Pd contacts to MoS_2," *Applied Physics Letters*, vol. 105, no. 11, p. 113505, 2014.

[187] S. Das, H.-Y. Chen, A. V. Penumatcha, and J. Appenzeller, "High performance multilayer MoS_2 transistors with scandium contacts," *Nano Letters*, vol. 13, no. 1, pp. 100–105, 2013.

[188] C. Gong, L. Colombo, R. M. Wallace, and K. Cho, "The unusual mechanism of partial fermi level pinning at metal-MoS_2 interfaces," *Nano Letters*, vol. 14, no. 4, pp. 1714–1720, 2014.

[189] C. R. Ryder, J. D. Wood, S. A. Wells, and M. C. Hersam, "Chemically tailoring semiconducting two-dimensional transition metal dichalcogenides and black phosphorus," *ACS Nano*, vol. 10, no. 4, pp. 3900–3917, 2016.

[190] Y. Zhao, K. Xu, F. Pan, C. Zhou, F. Zhou, and Y. Chai, "Doping, contact and interface engineering of two-dimensional layered transition metal dichalcogenides transistors," *Advanced Functional Materials*, vol. 27, no. 19, p. 1603484, 2017.

[191] H. L. Zou, B. L. Li, H. Q. Luo, and N. B. Li, "0D-2D heterostructures of Au nanoparticles and layered MoS_2 for simultaneous detections of dopamine, ascorbic acid, uric acid, and nitrite," *Sensors and Actuators B: Chemical*, vol. 253, pp. 352–360, 2017.

[192] J. Kim, S. Byun, A. J. Smith, J. Yu, and J. Huang, "Enhanced electrocatalytic properties of transition-metal dichalcogenides sheets by spontaneous gold nanoparticle decoration," *The Journal of Physical Chemistry Letters*, vol. 4, no. 8, pp. 1227–1232, 2013.

[193] S. Su, C. Zhang, L. Yuwen, J. Chao, X. Zuo, X. Liu, C. Song, C. Fan, and L. Wang, "Creating SERS hot spots on MoS_2 nanosheets with in situ grown gold nanoparticles," *ACS Applied Materials and Interfaces*, vol. 6, no. 21, pp. 18735–18741, 2014.

[194] F. Huo, Z. Zheng, G. Zheng, L. R. Giam, H. Zhang, and C. A. Mirkin, "Polymer pen lithography," *Science*, vol. 321, no. 5896, pp. 1658–1660, 2008.

[195] A. J. Bard, R. Parsons, and J. Jordan, *Standard potentials in aqueous solution*, vol. 6. CRC press, 1985.

[196] J.-S. Park and S.-H. Moon, "Use of cascade reduction potential for selective precipitation of Au, Cu, and Pb in hydrochloric acid solution," *Korean Journal of Chemical Engineering*, vol. 19, no. 5, pp. 797–802, 2002.

[197] I. Popov, G. Seifert, and D. Tomanek, "Designing electrical contacts to MoS_2 monolayers: a computational study," *Physical Review Letters*, vol. 108, no. 15, p. 156802, 2012.

[198] M. S. Abdou and S. Holdcroft, "Gold-decorated poly(3-alkylthiophenes)," *Chemistry of Materials*, vol. 8, no. 1, pp. 26–31, 1996.

[199] E. Pensa, E. Corts, G. Corthey, P. Carro, C. Vericat, M. H. Fonticelli, G. Bentez, A. A. Rubert, and R. C. Salvarezza, "The chemistry of the sulfur-gold interface: In search of a unified model," *Accounts of Chemical Research*, vol. 45, no. 8, pp. 1183–1192, 2012.

[200] M. L. Williams, "Core chemistry of gold and its complexes," *Inflammopharmacology*, vol. 16, no. 3, pp. 110–111, 2008.

[201] J. Berglund and L. Elding, "Kinetics and mechanism for reduction of tetrachloroaurate(iii), trans-dicyanodichloroaurate(iii),and trans-dicyanodibromoaurate(iii) by sulfite and hydrogen sulfite," *Inorganic Chemistry*, vol. 34, no. 2, pp. 513–519, 1995.

[202] S. McDonnell, R. Addou, C. Buie, R. M. Wallace, and C. L. Hinkle, "Defect-dominated doping and contact resistance in MoS_2," *ACS Nano*, vol. 8, no. 3, pp. 2880–2888, 2014.

[203] Y. Liu, B. Liu, Q. Wang, Y. Liu, C. Li, W. Hu, P. Jing, W. Zhao, and J. Zhang, "Three dimensionally ordered macroporous Au/CeO_2 catalysts synthesized via different methods for enhanced CO preferential oxidation in H_2-rich gases," *RSC Advances*, vol. 4, no. 12, pp. 5975–5985, 2014.

[204] T. Korn, S. Heydrich, M. Hirmer, J. Schmutzler, and C. Schuller, "Low-temperature photocarrier dynamics in monolayer MoS_2," *Applied Physics Letters*, vol. 99, no. 10, p. 102109, 2011.

[205] S. Tongay, J. Zhou, C. Ataca, J. Liu, J. S. Kang, T. S. Matthews, L. You, J. Li, J. C. Grossman, and J. Wu, "Broad-range modulation of light emission in two-dimensional semiconductors by molecular physisorption gating," *Nano Letters*, vol. 13, no. 6, pp. 2831–2836, 2013.

[206] D. H. Kim and D. Lim, "Effects of defects and impurities on the optical properties and the valley polarization in monolayer MoS_2," *Journal of the Korean Physical Society*, vol. 66, no. 10, pp. 1564–1568, 2015.

[207] K. F. Mak, K. He, C. Lee, G. H. Lee, J. Hone, T. F. Heinz, and J. Shan, "Tightly bound trions in monolayer MoS_2," *Nature Materials*, vol. 12, no. 3, pp. 207–211, 2013.

[208] Y.-H. Lee, X.-Q. Zhang, W. Zhang, M.-T. Chang, C.-T. Lin, K.-D. Chang, Y.-C. Yu, J. T.-W. Wang, C.-S. Chang, and L.-J. Li, "Synthesis of large-area MoS_2 atomic layers with chemical vapor deposition," *Advanced Materials*, vol. 24, no. 17, pp. 2320–2325, 2012.

[209] X. Ling, Y.-H. Lee, Y. Lin, W. Fang, L. Yu, M. S. Dresselhaus, and J. Kong, "Role of the seeding promoter in MoS_2 growth by chemical vapor deposition," *Nano Letters*, vol. 14, no. 2, pp. 464–472, 2014.

[210] D. J. Eichelsdoerfer, X. Liao, M. D. Cabezas, W. Morris, B. Radha, K. A. Brown, L. R. Giam, A. B. Braunschweig, and C. A. Mirkin, "Large-area molecular patterning with polymer pen lithography," *Nature Protocols*, vol. 8, p. 2548, 2013.

[211] A. Splendiani, L. Sun, Y. Zhang, T. Li, J. Kim, C.-Y. Chim, G. Galli, and F. Wang, "Emerging photoluminescence in monolayer MoS_2," *Nano Letters*, vol. 10, no. 4, pp. 1271–1275, 2010.

[212] Y. Li, J. G. DiStefano, A. A. Murthy, J. D. Cain, E. D. Hanson, Q. Li, F. C. Castro, X. Chen, and V. P. Dravid, "Superior plasmonic photodetectors based on Au@MoS_2 core-shell heterostructures," *ACS Nano*, vol. 11, no. 10, pp. 10321–10329, 2017.

[213] S. Najmaei, A. Mlayah, A. Arbouet, C. Girard, J. Lotin, and J. Lou, "Plasmonic pumping of excitonic photoluminescence in hybrid MoS_2-Au nanostructures," *ACS Nano*, vol. 8, no. 12, pp. 12682–12689, 2014.

[214] M.-G. Lee, S. Yoo, T. Kim, and Q.-H. Park, "Large-area plasmon enhanced two-dimensional MoS_2," *Nanoscale*, vol. 9, no. 42, pp. 16244–16248, 2017.

[215] G. M. Akselrod, T. Ming, C. Argyropoulos, T. B. Hoang, Y. Lin, X. Ling, D. R. Smith, J. Kong, and M. H. Mikkelsen, "Leveraging nanocavity harmonics for control of optical processes in 2D semiconductors," *Nano Letters*, vol. 15, no. 5, pp. 3578–3584, 2015.

[216] A. U. Borwankar, B. W. Willsey, A. Twu, J. J. Hung, R. J. Stover, T. W. Wang, M. D. Feldman, T. E. Milner, T. M. Truskett, and K. P. Johnston, "Gold nanoparticles with high densities of small protuberances on nanocluster cores with strong NIR extinction," *RSC Advances*, vol. 5, no. 127, pp. 104674–104687, 2015.

[217] W. Luo, R. Yang, J. Liu, Y. Zhao, W. Zhu, and G. Xia, "Thermal sublimation: a scalable and controllable thinning method for the fabrication of few-layer black phosphorus," *Nanotechnology*, 2017.

[218] X. Lu, M. I. B. Utama, J. Zhang, Y. Zhao, and Q. Xiong, "Layer-by-layer thinning of MoS_2 by thermal annealing," *Nanoscale*, vol. 5, no. 19, pp. 8904–8908, 2013.

[219] H.-P. Komsa, J. Kotakoski, S. Kurasch, O. Lehtinen, U. Kaiser, and A. V. Krasheninnikov, "Two-dimensional transition metal dichalcogenides under electron irradiation: Defect production and doping," *Physical Review Letters*, vol. 109, no. 3, p. 035503, 2012.

[220] K. C. Kwon, K. S. Choi, and S. Y. Kim, "Increased work function in few-layer graphene sheets via metal chloride doping," *Advanced Functional Materials*, vol. 22, no. 22, pp. 4724–4731, 2012.

[221] Z. Zheng, W. Daniel, L. Giam, F. Huo, A. Senesi, G. Zheng, and C. Mirkin, "Multiplexed protein arrays enabled by polymer pen lithography: Addressing the inking challenge," *Angewandte Chemie*, vol. 121, no. 41, pp. 7762–7765, 2009.

[222] S. Bian, J. He, K. B. Schesing, and A. B. Braunschweig, "Polymer pen lithography (PPL)-induced site-specific click chemistry for the formation of functional glycan

arrays," *Small*, vol. 8, no. 13, pp. 2000–2005, 2012.

[223] L. Huang, A. B. Braunschweig, W. Shim, L. Qin, J. K. Lim, S. J. Hurst, F. Huo, C. Xue, J.-W. Jang, and C. A. Mirkin, "Matrix-assisted dip-pen nanolithography and polymer pen lithography," *Small*, vol. 6, no. 10, pp. 1077–1081, 2010.

[224] C. E. Hoyle and C. N. Bowman, "Thiol-ene click chemistry," *Angewandte Chemie International Edition*, vol. 49, no. 9, pp. 1540–1573, 2010.

[225] X. Chen, N. C. Berner, C. Backes, G. S. Duesberg, and A. R. McDonald, "Functionalization of two-dimensional MoS_2: On the reaction between MoS_2 and organic thiols," *Angewandte Chemie International Edition*, vol. 55, no. 19, pp. 5803–5808, 2016.

[226] P. K. Chow, E. Singh, B. C. Viana, J. Gao, J. Luo, J. Li, Z. Lin, A. L. Elias, Y. Shi, and Z. Wang, "Wetting of mono and few-layered WS_2 and MoS_2 films supported on Si/SiO_2 substrates," *ACS Nano*, vol. 9, no. 3, pp. 3023–3031, 2015.

[227] D. J. Eichelsdoerfer, K. A. Brown, M. X. Wang, and C. A. Mirkin, "Role of absorbed solvent in polymer pen lithography," *The Journal of Physical Chemistry B*, vol. 117, no. 50, pp. 16363–16368, 2013.

[228] P. K. Sahoo, S. Memaran, Y. Xin, L. Balicas, and H. R. Gutirrez, "One-pot growth of two-dimensional lateral heterostructures via sequential edge-epitaxy," *Nature*, vol. 553, p. 63, 2018.

[229] Z. Zhang, P. Chen, X. Duan, K. Zang, J. Luo, and X. Duan, "Robust epitaxial growth of two-dimensional heterostructures, multiheterostructures, and superlattices," *Science*, vol. 357, no. 6353, pp. 788–792, 2017.

[230] E. D. Hanson, S. Mayekar, and V. P. Dravid, "Applying insights from the pharma innovation model to battery commercialization-pros, cons, and pitfalls," *MRS Energy and Sustainability*, vol. 4, 2017.

[231] "EV everywhere grand challenge blueprint," 2013.

[232] L. L. Gaines and R. M. Cuenca, "Costs of lithium-ion batteries for vehicles," report, Argonne National Laboratory, 2000.

[233] "Inventory of US greenhouse gas emissions and sinks: 1990-2014," 2016.

[234] D. Elliott, "A balancing act for renewables," *Nature Energy*, vol. 1, p. 15003, 2016.

[235] van Schalkwijk Walter and B. Scrosati, *Advances in lithium-ion batteries*. Springer Science and Business Media, 2007.

[236] J. Voelcker, "Electric-car battery costs: Tesla $190 per kwh for pack, gm $145 for cell." Available at `http://www.greencarreports.com/news/1103667_electric-car-battery-costs-tesla-190-per-kwh-for-pack-gm-145-for-cells`, 2016.

[237] C. Pillot, "The worldwide rechargeable battery market 2012-2025," report, Avicenne Energy, 2013.

[238] S. Mayekar, "Bringing new battery technology to market: Crossing the chasm," 2015.

[239] G. Crabtree, E. Kocs, and L. Trahey, "The energy-storage frontier: Lithium-ion batteries and beyond," *MRS Bulletin*, vol. 40, no. 12, pp. 1067–1078, 2015.

[240] A. Arora, R. Buckland, W. Buiter, P. D'Antonio, S. Ding, R. Edwards, R. Elliot, T. Fordham, I. Goldin, J. Hale, K. Horowitz, N. Iizuka, E. Lee, W. Lee, T. Levkovich, H. Lorenzen, D. Lubin, G. Menuet, E. Morse, R. Morse, K. Murashima, D. Peterson, A. Pitt, E. Rahbari, T. Sasaki, M. Saunders, S. Savvantidou, M. Schofield, M. Shen, J. Shoup, M. Spittle, and A. Yuen, "Investment themes in 2015: Dealing with divergence," report, Citi GPS, 2015.

[241] C. Pillot, "The rechargeable battery market and main trends 2015-2025," in *Lithium Battery International Summit*, Avicenne Energy.

[242] B. Nykvist and M. Nilsson, "Rapidly falling costs of battery packs for electric vehicles," *Nature Climate Change*, vol. 5, no. 4, pp. 329–332, 2015.

[243] G. G. Franco, "Advanced and post lithium-ion batteries 2016-2026: Technologies," *Markets, Forecasts-Silicon anode, solid-state, sulphur, lithium-air, sodium-ion and magnesium batteries, and lithium capacitors, IDTechEx*, 2015.

[244] "10 hot consumer trends 2016," report, Erricsson Consumer Lab, 2015.

[245] A. Stephan, T. S. Schmidt, C. R. Bening, and V. H. Hoffmann, "The sectoral configuration of technological innovation systems: Patterns of knowledge development and diffusion in the lithium-ion battery technology in japan," *Research Policy*, vol. 46, no. 4, pp. 709–723, 2017.

[246] M. A. Kirchberger and L. Pohl, "Technology commercialization: a literature review of success factors and antecedents across different contexts," *The Journal of Technology Transfer*, vol. 41, no. 5, pp. 1077–1112, 2016.

[247] A. Giniatullina, M. Boorsma, G.-J. Mulder, and S. van Deventer, "Building for big pharma," *Nature biotechnology*, vol. 31, no. 4, pp. 284–287, 2013.

[248] "CB insights venture capital database," 2016.

[249] B. E. Gaddy, V. Sivaram, T. B. Jones, and L. Wayman, "Venture capital and cleantech: The wrong model for energy innovation," *Energy Policy*, vol. 102, pp. 385–395, 2017.

[250] C. Laslau, "What it really costs to commercialize new battery technology: Lessons from more than a decade of investment data," report, luxresearch, 2016.

[251] R. E. Ciez and J. F. Whitacre, "The cost of lithium is unlikely to upend the price of Li-ion storage systems," *Journal of Power Sources*, vol. 320, pp. 310–313, 2016.

[252] S. Lacey, "Stem cto: Lithium-ion battery prices fell 70% in the last 18 months." Available at https://www.greentechmedia.com/articles/read/stem-cto-weve-seen-battery-prices-fall-70-in-the-last-18-months.

[253] "Best practices: Intellectual property protection in china." Available at https://www.uschina.org/reports/best-practices-intellectual-property-protection-china,
2016.

[254] N. Research, "Materials for advanced batteries." Available at https://www.navigantresearch.com/research/materials-for-advanced-batteries.

[255] D. Chung, E. Elgqvist, and S. Santhanagopalan, "Automotive lithium-ion cell manufacturing: Regional cost structures and supply chain considerations," *Contract*, vol. 303, pp. 275–3000, 2016.

[256] "Cobalt." Available at `https://en.wikipedia.org/wiki/Cobalt#/media/File:Kobalt_electrolytic_and_1cm3_cube.jpg`, 2017.

[257] "Black powder." Available at `https://commons.wikimedia.org/wiki/File:Black_Powder-1.JPG`, 2017.

[258] "Prototype of 75 watt-hour lithium-ion polymer battery." Available at `https://en.wikipedia.org/wiki/Electric_car/media/File:NASA_Lithium_Ion_Polymer_Battery.jpg`, 2017.

[259] "Chevy volt first battery." Available at `https://commons.wikimedia.org/w/index.php?curid=36091953`, 2017.

[260] "Tesla roadster 2.5." Available at `https://commons.wikimedia.org/wiki/Category:Tesla_Roadster/media/File:Roadster_2.5_windmills.jpg`, 2017.

[261] "Samsung SDI research and development." Available at http://www.samsungsdi.com/about-sdi/research-development.html, 2016.

[262] S. LeVine, "The story of the invention that could revolutionize batteries-and maybe american manufacturing as well." Available at http://qz.com/433131/the-story-of-the-invention-that-could-revolutionize-batteries-and-maybe-american-manufacturing-as-well/, 2015.

[263] M. Parrish, "How the dow-dupont merger will impact the chemicals industry." Available at http://www.chem.info/article/2016/03/how-dow-dupont-merger-will-impact-chemicals-industry, 2016.

[264] S. Hogg, "Why so many vc firms invest in the same companies." Available at https://www.entrepreneur.com/article/227144, 2013.

[265] N. V. C. Association, *NVCA yearbook*. Thomson Financial Venture Economics, 2015.

[266] "Gilead sciences announces first quarter 2016 financial results." Available at http://www.gilead.com/news/press-releases/2016/4/gilead-sciences-announces-first-quarter-2016-financial-results, 2016.

[267] "Biopharm america." Available at https://ebdgroup.knect365.com/biopharm-america, 2016.

[268] K. E. Eheman Jr, "Planning for the exit," *Nature Biotechnology*, vol. 30, no. 2, pp. 132–134, 2012.

[269] Z. Brennan, "Final rule on clinical trial transparency: Will it be enough to encourage more compliance?." Available at http://raps.org/Regulatory-Focus/News/2016/09/16/25867/Final-Rule-on-Clinical-Trial-Transparency-Will-it-be-Enough-to-Encourage-More-Compliance, 2016.

[270] "Clinicaltrials.gov." Available at https://clinicaltrials.gov/, 2016.

[271] M. Martino and C. Myers, "Top venture capital firms." Available at http://www.fiercebiotech.com/special-report/top-venture-capital-firms.

[272] "Samsung invests in xg sciences, to co-develop graphene-based batteries." http://www.graphene-info.com/samsung-invests-xg-sciences-co-develop-graphene-based-batteries,
2014.

[273] "24M delivers initial quantity of production-size semisolid lithium-ion cells to NEC energy solutions for testing and validation." Available at http://24-m.com/pressrelease, 2016.

[274] W. Pentland, "Canadian battery startup is succeeding where u.s. startups have mostly failed." Available at http://www.forbes.com/sites/williampentland/2015/11/16/canadian-battery-startup-is-succeeding-where-u-s-startups-have-mostly-failed/,
2015.

[275] "Key dates in a123 systems history." Available at https://www.bostonglobe.com/business/2012/10/16/ key-dates-systems-history,
2012.

[276] G. Gereffi, T. Trigg, and M. Lowe, "Case study: A123 systems local markets and competitiveness a value chain analysis," report, Duke University, 2010.

[277] "Chain reaction innovation is DOE's newest investment in the clean energy innovation ecosystem." Available at https://energy.gov/eere/amo/articles/chain-reaction-innovation-doe-s-newest-investment-clean-energy-innovation,
2016.

[278] A. Damodaran, "Margins by sector (US)." Available at `http://pages.stern.nyu.edu/~adamodar/New_Home_Page/datafile/margin.html`,
2016.

[279] "Spending of U.S. pharmaceutical industry for research and development as a percentage of total revenues from 1990 to 2015." Available at https://www.statista.com/statistics/265100/us-pharmaceutical-industry-spending-on-research-and-development-since-1990,
2016.

[280] "Expected global market share of lithium battery makers in 2016." Available at https://www.statista.com/statistics/235323/lithium-batteries-top-manufacturers,
2016.

[281] "Panasonic annual report 2014," report, Panasonic Corporation, 2014.

[282] "LG chem annual report 2015," report, LG Chem, 2015.

[283] "Fact sheet: New drug development process," report, California Biomedical Research Association.

[284] M. J. Waring, J. Arrowsmith, A. R. Leach, P. Leeson, S. D.Mandrell, R. M. Owen, G. Pairaudeau, W. D. Pennie, S. D. Pickett, J. Wang, O. Wallace, and A. Weir, "An analysis of the attrition of drug candidates from four major pharmaceutical companies," *Nature Reviews Drug Discovery*, vol. 14, no. 7, pp. 475–486, 2015.

APPENDIX A

Broader impacts: applying insights from the pharma innovation model to battery materials commercialization

Adapted with permission from Eve D. Hanson, Samir Mayekar, Vinayak P. Dravid, Applying Insights from the Pharma Innovation Model to Battery Commercialization - Pros, Cons, and Pitfalls, MRS - Energy and Sustainability, 4, 2017.[230]

With the decline of large corporate research institutions such as Bell Labs, there is an increasing onus on universities to translate their fundamental discoveries into commercializable products. This applied research and development (R&D) process is particularly challenging for advanced materials. With this broader mandate in mind, I examine the challenges to commercializing advanced materials, with a focus on battery materials. I also propose strategies that technologists and entrepreneurs can use to improve their odds at success.

A.1. Introduction

Better batteries are critical to the world's clean energy future. Achieving more economical and efficient rechargeable energy storage ($< \$125$ kilowatt-hour[231]) would enable long range electric vehicles (EVs) to economically compete with gasoline cars,[232] a key step in electrifying transportation and reducing the transportation sector's 25% share of US CO_2 emissions.[233] Improved energy storage can help balance an intermittent electricity load, allowing more intermittent renewable energy generation sources to

come online.[234] Improving battery technology is instrumental to achieving these goals. Rechargeable, energy-dense batteries were made possible in 1991, with the introduction of lithium-ion batteries by Sony.[235] The lithium-ion battery's rechargeable nature and eventual higher energy density allowed for the design, manufacture, and sale of entirely new classes of devices. Based on this energy density, lithium-ion batteries are the current battery technology of choice for electric vehicles (EVs) and most consumer electronics.[236] Further improving lithium-ion battery performance is a crucial enabler to achieve the outlined sustainability goals.

A.1.1. Introduction to lithium-ion batteries

Since this commercial introduction 25 years ago, both industrial and academic researchers have conducted an impressive amount of work on lithium-ion battery chemistries. Encouragingly, lithium-ion battery energy storage has steadily increased, while costs have steadily decreased over the last 25 years. These benefits stem from consistent improvements in manufacturing, design, safety, and chemistry. Figure A.1 shows this trend, with gravimetric energy density on the y-axis and volumetric energy density on the x-axis.[237, 238] The figure shows steady but incremental progress over the last 20+ years, with an average gravimetric energy density increase of 4% per year. The concurrent decrease of cost per kilowatt-hour is shown on the right of figure A.1.[239–241] Lithium-ion batteries for electric vehicles have recently shown an even faster reduction in cost, as they have moved from a niche application to a mass-manufactured commodity product.[242]

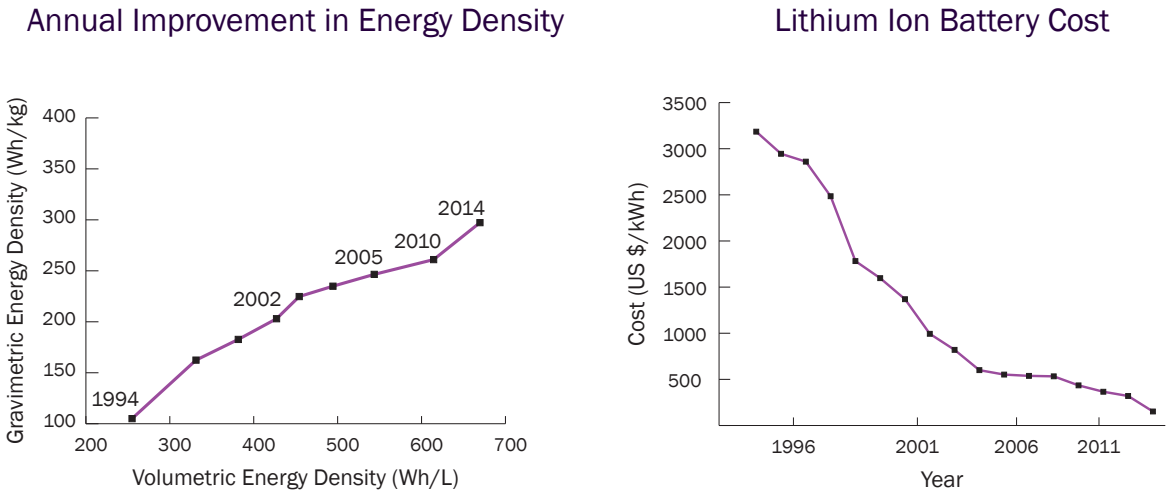

Figure A.1. Over the last 20+ years, lithium-ion battery gravimetric and volumetric energy density have gradually improved, while over the last 20+ years, consumer electronics lithium-ion battery cost per kilowatt-hour has steadily decreased.[240, 241] Reproduced with permission from [230].

A.1.2. Limitations of current battery commercialization model

Large chemical companies and battery manufacturers have historically led lithium-ion battery commercialization, yet this state of affairs has significant limitations. The incremental enhancements in lithium-ion cell capacity delivered by multinational chemical companies fall dramatically short of consumer demands.[243, 244] One reason for these shortcomings is that Original Equipment Manufacturers (OEMs) tend to put significant price pressure on battery suppliers, with little regard for innovation. Second, in the age of activist investors and market consolidation (see: Dow/DuPont merger), Wall Street pressures on earnings result in R&D budgets being squeezed so that only the most market-ready (incremental) approaches are explored, limiting the likelihood of step-change improvements. The traditional commercialization model also hinders US competitiveness. Because most battery manufacturers are in Asia, the economic benefit of US battery research advances

tends to be absorbed by these foreign manufacturers. Conversely, small US companies and startups are challenged by the tight-margin, commoditized, large volume battery business. This situation leads to a US battery commercialization gap, with a dearth of US companies commercializing US battery research gains. The technology transfer literature has established that both policy and market drivers impact innovation pathways.[245, 246] As such, we examine both the policy and market factors that hinder US competitiveness.

A.1.3. Comparisons to pharmaceutical industry

The pharmaceutical industry has many characteristics similar to the battery industry, such as high technology risk, long timelines to success, and large capital requirements. Wall Street pressures have also squeezed big pharmaceutical R&D programs.[247] However, unlike the battery industry, the pharmaceutical industry has a vibrant commercialization ecosystem, with a healthy pipeline of startup companies developing new drugs and a variety of different sized industry players enhancing market competition.[247] This enables more drugs to be explored, come to market, and ultimately help more patients, all while producing economic growth. This paper examines the particulars of both the pharmaceutical and battery industries to inform proposals for the latter via the success of the former. We provide tailored proposals to the battery industry's key stakeholders (startups, large manufacturers, investors, and policy makers) to improve commercialization outcomes. By fostering a more successful commercialization pathway for startups and small companies, we hope to encourage more entrepreneurial activity that can lead to critically important improvements in battery technology.

A.2. Materials innovation is notoriously difficult

Commercializing new materials, both inside and outside the battery space, is notoriously challenging. This is true both for big companies and startups, but we will focus on startups in this report given the authors' focus and expertise. We analyzed a sample of 36 representative startups from the battery technology space that have received greater than $500k in funding and were founded after 1995, as shown in Figure A.2.[248] Of these, only two have had positive exits, with returned capital that was greater than the invested capital (greater than 1x return). Only 17 of the others reached early commercialization, as indicated by pilot-scale manufacturing or key corporate partnership deals; they required an average of 8 years to do so.

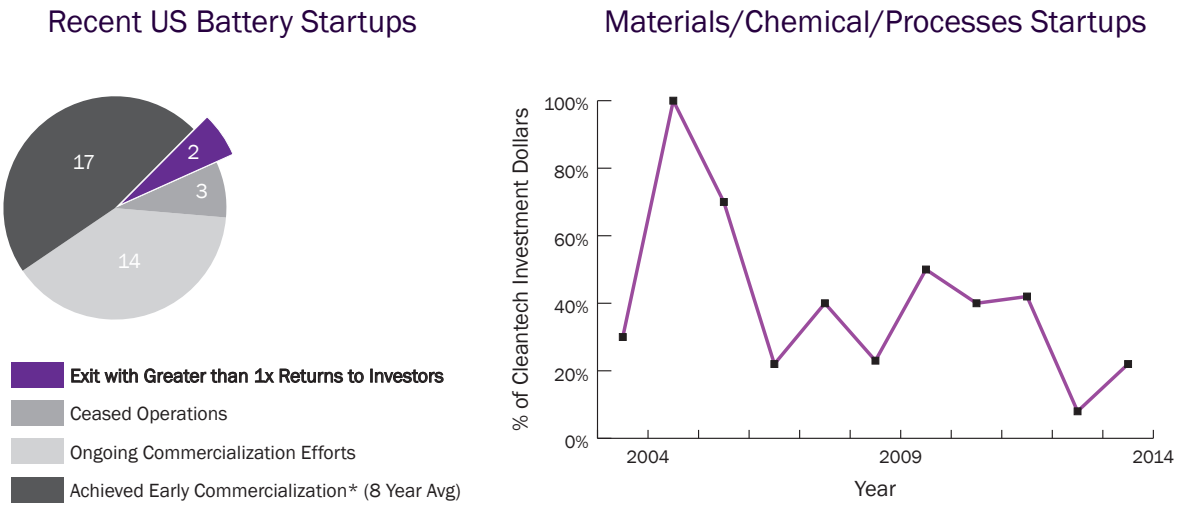

Figure A.2. US battery and energy materials companies have underperformed venture expectations over the last ten years. The CB Insights venture capital database lists only 36 battery technology startups with 500K+ of investment founded since 2000. Of these, only 2 have returned the invested capital to investors.[248] As a result, cleantech investment in Energy Materials/Chemical/Processes has declined, representing $< 30\%$ of cleantech investment dollars in 2014.[249] Reproduced with permission from [230].

The challenges to battery commercialization that lead to these high failure rates include high upfront capital requirements, intellectual property barriers and long timelines to success. These challenges derive from entrepreneurs needing to close the R&D gap from a university lab-scale technology to a technology that is compatible with battery manufacturing techniques, while simultaneously exceeding multiple industry benchmarks. The R&D pathway to pilot-scale battery manufacturing requires expensive labs, specialized workers, and 4-8 years of work.[250] Further, to be considered meaningful by battery manufacturers and potential customers, cycle life data must be taken for months at a time. With such long iteration cycles, there are few opportunities to de-risk the technology in a meaningful way, and progress takes longer to achieve. In addition, for a new material to be attractive to the market, it must match or exceed industry benchmarks across several key metrics (cycle life, energy density, electrode loading, etc.) simultaneously. These technical challenges remain formidable. Characteristics specific to the battery market also make starting a US-based small company daunting. Most importantly, the biggest target battery applications (consumer electronics, electric cars) have highly competitive, commoditized markets with only 5% operating margins over the last two years.[251] OEMs put tremendous pressure on battery suppliers to reduce prices. Additionally, there are a limited number of battery redox materials found to date that have properties suitable for battery operation. As a result, the permutations of battery materials available in the near future are limited, adding to the commoditization of the industry. With such slim margins, scale is critical to make the economics work profitably, and reaching scale is both time and capital-intensive. Another challenge to US startups is that major battery manufacturers are predominately located in Asia with cheaper manufacturing capabilities.[252]

Since protecting intellectual property (IP) is more challenging in many parts of Asia, trade secrets and opacity characterize the industry.[253] With such secrecy about the metrics and challenges of the industry, it is difficult for startups to address pain points with appropriate specificity for battery manufacturers. Due to the low expected profitability created by these challenges, venture investment in the battery sector is commensurately low. Recent underperformance of energy materials companies indicates that this hesitancy is appropriate. Figure A.2 shows the low returns for energy materials companies and resultant venture investment declines over the last 10 years.[249] Energy companies focused on Materials/Chemicals/Processes (a parent category of battery startups) have returned only $123M for $764M (16%) invested over the 2004-2014 period (in other words, investors lost 84% of their invested capital).[249] As a result of this poor performance, in 2013 and 2014, Chemical/Materials/Processes energy startups received less than 30% of the cleantech investment dollars and represent only ~30% of cleantech companies receiving investment at all.[249] Given such discouraging outcomes, we look to characterize the status quo and provide some suggestions to improve investment returns in the future.

A.3. Traditional battery commercialization model

There are three main techniques for improving upon current lithium-ion battery specifications. 1) Processing and design, or designing the end product to utilize the battery power most efficiently. Battery manufacturers have limited control over this, given existing infrastructure investments. 2) Mechanical improvements, like packing more active material into a given battery specification. The runway on this approach has run out and is limited by safety standards. 3) Chemistry/materials improvements: Since battery

manufacturers have the most room for improvement on the chemistry side, this is where they currently focus.

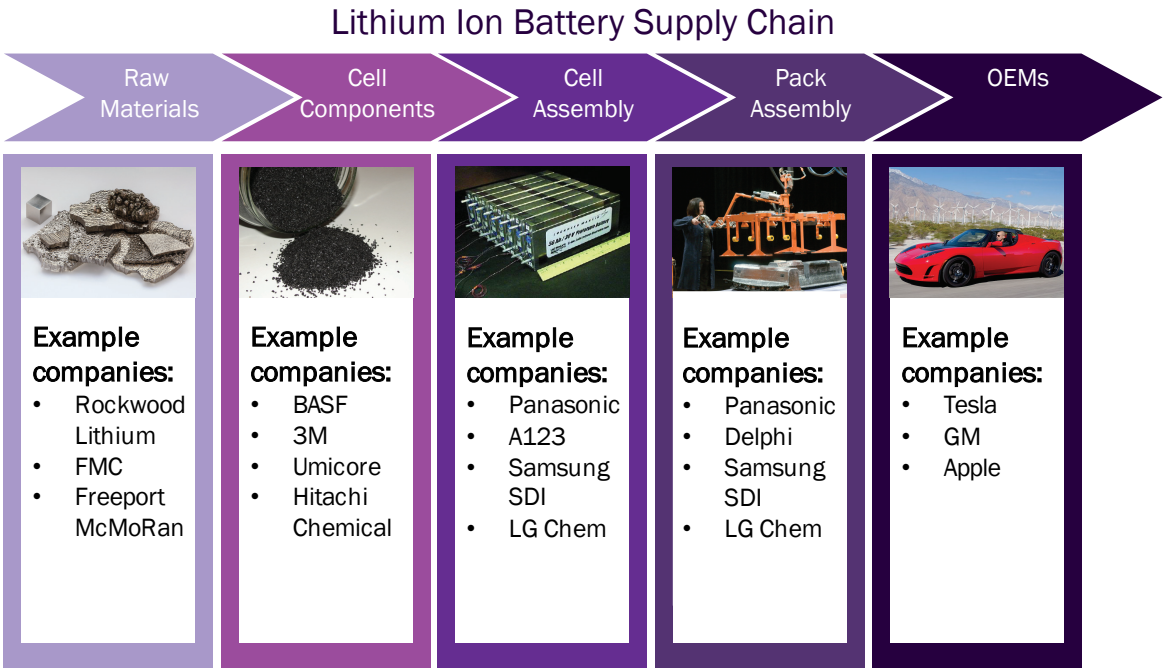

Figure A.3. Typical lithium-ion battery supply chain. In the lithium-ion battery supply chain, cell components and cell assembly manufacturers typically pioneer the battery chemistry innovation.[241, 254–260] Images from references [256–260] Reproduced with permission from [230].

The lithium-ion battery supply chain structure informs which companies focus on battery commercialization. Figure A.3 shows a typical lithium-ion battery supply chain. Along the supply chain, cell component and cell assembly manufacturers typically lead the battery chemistry R&D. Cell component manufacturers, such as Johnson Matthey, can provide a new anode or cathode material with higher performance standards to the cell assembly manufacturers. Cell assembly manufacturers, such as Samsung SDI or LG Chem, also have internal R&D departments tasked with improving the materials and manufacturing processes. For example, Samsung SDI spent $500M+ on R&D in 2015,

accounting for ~7% of total sales.[261] The current model, which is dominated by large companies, has benefits and drawbacks. On the upside, it has brought steady improvements in lithium-ion battery energy density and performance while costs have fallen. However, these incremental improvements have not been sufficient to satisfy the more rapid growth in consumer demands for better battery performance.[244] With entrenched science and manufacturing methods, innovation can fall by the wayside. A classic example is the manufacturing technique used to coat electrode materials: slot die coating. Slot die coating was previously used for making cassette tapes. When Sony started to scale up the first lithium-ion battery production, they decided to use flat die coaters, because the manufacturing equipment was already available and underutilized as consumers turned to CDs over cassette tapes.[262] Slot die coating is not necessarily the optimal technique to coat electrode materials, yet it is still widely adopted by the battery industry due to switching costs: it is not financially attractive for large companies to change techniques, given their invested assets. A startup, in contrast, is much less tied to existing techniques and can more economically provide the manufacturing foundation for larger performance improvements.[262] The supply chain structure can also limit innovation. Since battery manufacturers generally do not have direct access to the end consumer, they cannot raise prices for a premium product. The battery manufacturers must sell to the OEMs. For the OEMs, the battery is only one component in a complex product, and price, reliability, and safety are the top concerns. There are also financial challenges to large battery company innovation. As the industry sees more consolidation, such as the recent Dow and DuPont merger, the industry has valued the economic value of production scale more than innovation.[263] Wall Street activism pushes for consistent quarterly earnings, which

can result in sacrificed long-term innovation for short-term financial benefit, a pressure not felt by private startup companies. This Wall Street focus has hurt internal R&D budgets.[263] Finally, the current model tends to benefit Asian manufacturers at the expense of US competitiveness. Battery research breakthroughs made by US universities and national labs tend to be absorbed and commercialized by the "Big Three" battery manufacturers in Asia (LG Chem, Samsung SDI, and Panasonic). We believe that the US should be better set up to commercialize new battery technologies via US startups, and reap the economic and social benefits within the US.

A.4. US battery startup commercialization model

Many US startup companies have attempted to commercialize new battery materials, yet few have succeeded. Some examples include A123, 24M, Ambri, Leyden Energy, Quantumscape, and Envia Systems. The clear majority have failed to bring new technology to market in a financially sustainable (i.e., profitable) way. While a case study could be built on each of these companies and its unique challenges, there are some commonalities across these companies within the traditional venture-backed commercialization model that they shared. A few key features:

- Finance primarily via venture capital
- Focus go-to-market plan on attacking large-scale markets ($1B+)
- Seek to capture value alone (as opposed to with corporate partners)
- Attempt to speed scientific progress via increased spending
- Raise large amounts of capital upfront ($50+M)

Venture capital's demands for 5-10x returns drive this approach. While this model may work for other industries such as software, we believe there are several reasons why this model does not work for the battery industry. First, the multiples that venture capital seeks are extraordinarily difficult to achieve in a low-margin, commoditized market.[264] Second, it is exceedingly expensive to build up the manufacturing capabilities and know-how to compete with large volume incumbents. Third, there are challenges with attempting to rapidly expedite R&D efforts with large amounts of capital. In the world of software companies with a functional business model, "money in" typically yields user growth and more "money out." This principle does not apply to battery companies; more capital will not necessarily yield hastened scientific progress. For example, to improve cycle life in a given material, iteration cycles will be long because cycle life data requires months to collect, despite abundant capital. Greater capital does not necessarily speed cycle life improvements. Fourth, tales of battery technology companies raising $50-$100M without fully de-risking fundamental chemistry barriers are abundant. By the time the companies mature, they lack a viable exit pathway to grant investors and employees liquidity. Accordingly, we believe the US startup commercialization model should change.

A.5. Pharmaceutical commercialization model

The pharmaceutical startup commercialization model is well-developed, robust, and supports a large startup innovation ecosystem. Over $10B venture capital dollars were invested in the medical/health/life sciences space in just 2015, across 830 deals.[265] A variety of drivers lead the big pharmaceutical companies to support this innovation ecosystem. First, the high margins inherent in the pharma industry support a vibrant ecosystem.

Once launched, new drugs can have gross margins of up to ~90%.[266] Strict patent protection creates a built-in monopoly for novel drugs serving an unmet need/disease area, protecting these high margins. This creates demand for potential new drugs. Second, based on Wall Street pressures, big pharmaceutical companies have shrunk their internal R&D departments.[247] In-house R&D is often used for tweaks or new indication testing on existing products, as opposed to exploring fundamentally new drugs in new disease areas. Thus, access to startup-developed drugs (via acquisitions or partnerships) is key to maintaining the company's growth and launching new products. Third, acquisitions allow big pharmaceutical companies to obtain technology, diverse experience, and relevant skills relatively cheaply, versus trying to build up those capabilities on their own. Figure A.4 shows pharma acquisition values by FDA phase between 2005 and 2012.[247] Based on the large margins and potential profit values, the acquisition deal values are substantial: often, in the hundreds of millions. The FDA clinical development phases serve as benchmarks for the company's technical progress. Each clinical development phase requires meeting or exceeding increasingly complex clinical endpoints to continue in the process towards market approval. This system implies that a company has increasingly de-risked its technology, and its value often improves accordingly. It is important to note that all the acquisitions shown in the figure are pre-revenue and that acquisitions occur at each stage along the R&D development pathway.

Within the pharmaceutical market, a robust ecosystem of mergers and acquisitions (M&A) activity has developed. Conferences hold formal meet and greet events for startups and big pharmaceutical companies.[267] Pharmaceutical companies market their target partnering and acquisition areas via dedicated websites and business development

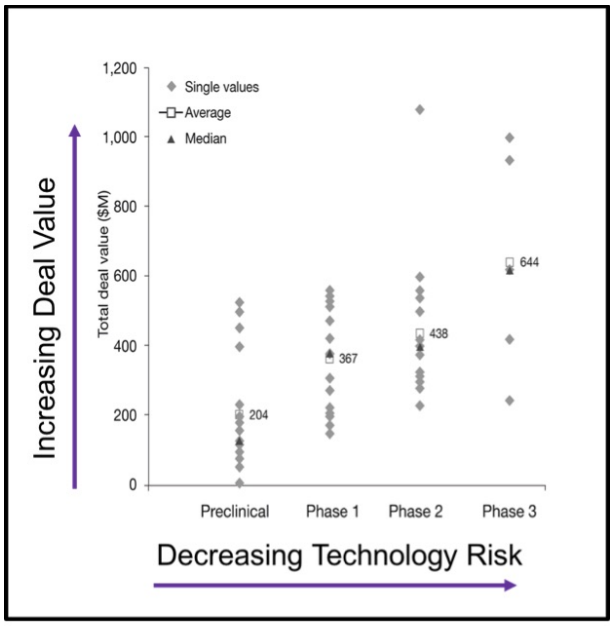

Figure A.4. Deal sizes of pharmaceutical startup acquisitions between 2005 and 2012. Adapted by permission from Macmillan Publishers Ltd: Nature Biotechnology (17), copyright (2013).

brochures.[247] Acquisitions and strategic investments are widespread enough to have developed a variety of complex deal terms.[268] FDA-forced transparency in the marketplace further benefits the M&A ecosystem. The FDA now requires that clinical trial data be published publicly.[269, 270] This allows investors or potential acquirers to have broad access to relevant data. That access enables them to examine the most critical scientific data, and ultimately further de-risk a potential investment. Many venture capital funds focus on life sciences/pharmaceutical investments, with scientific experts performing detailed diligence on candidate companies' fundamental science.[271] Together, these industry characteristics make pharma an attractive industry for startup innovation.

A.6. Applying lessons from the pharma model to battery innovation

In this section, we propose changes to the battery startup commercialization model based on the pharma innovation model. We will then address the potential pitfalls of the proposed approach and arrive at final recommendations

A.6.1. Proposals for entrepreneurs

A.6.1.1. R&D strategy. Inspired by the pharmaceutical model, we recommend that entrepreneurs focus on customer-led performance metrics as early as possible. A frequent mistake in battery startups is to confuse academic figures of merit for industry-set figures of merit. For example, academic research tends to focus on initial figures of merit such as energy density, novelty, or mechanism rather than accelerated testing or commercial compatibility. In contrast, industry requires high energy density concurrent with long cycle life, high electrode loading and other factors. At the minimum, sending samples to customers to receive early testing and feedback is highly advantageous and helps ensure that startup R&D efforts are working against a market-driven goal. Joint development agreements can also help ensure that entrepreneurs focus on the appropriate industry metrics. In the pharmaceutical industry, joint development agreements are common, complementing the startup's technology with large company resources and ensuring industry validation. For better chances of success, we recommend battery startups look for corporate partnerships and joint development agreements to leverage the resources and market know-how of large company partners. There are a few early examples of US startups leveraging large company resources; XG Sciences has a partnership with Samsung

SDI to develop anode materials,[272] while 24M and NEC have partnered to commercialize grid-scale storage systems. As part of the agreement, NEC is testing 24M products. This provides crucial industry validation, which raises 24M's credibility with customers and potential acquirers.[273]

A.6.1.2. Fundraising. Due to misalignment between venture capital expectations and battery market realities, we recommend entrepreneurs look for non-traditional sources of capital. This could include government grants (ARPA-E research grants, SBIR grants), corporate partnership research dollars, or philanthropic capital. Venture capital may be sought, but entrepreneurs should recognize that venture capital expectations may not be well aligned with the battery market's realities. Successful entrepreneurs are realistic about exit opportunities and fundraise strategically to make exits meaningful. In the pharmaceutical industry, acquisitions happen all along the commercialization chain, with more developed drugs receiving higher acquisition values. There are similar opportunities in the battery space: a battery startup does not need to hit full manufacturing production to be valuable. However, exits in the battery space tend to fall into two categories: IP-driven exits that are less than $10M, and manufacturing/asset-driven exits that are greater than $50M. In the past, these exits have not been particularly lucrative. Many IP-focused companies will raise over $20M, overcapitalizing potential exits (e.g. Leyden Energy). To be prudent, entrepreneurs should take on modest amounts of capital and apply it very strategically to the most critical, market-driven R&D and sales efforts. In the pharmaceutical industry, entrepreneurs generally fundraise according to their FDA phase of development. Similarly, battery entrepreneurs should recognize their end goal; if they do not plan to go into large-scale manufacturing, then capitalization must remain modest

(< $20M) if they are to generate incremental value from technology sale or licensing. We recognize that building complex battery technology requires significant effort and funding, so the challenge for entrepreneurs will be attracting non-dilutive sources of funding to keep the capital profile of the company attractive for potential licensors, partners, and buyers.

A.6.1.3. Application selection. We recommend that battery entrepreneurs attack higher margin, niche applications first. Such beachhead or small target markets are critical to gathering customer revenue and feedback faster for new battery technologies. The biggest emerging battery markets, such as automotive EVs, have prohibitively long timelines to success. Even after hitting full battery production scale (10+ year process), there is a 7-10 year process of becoming a new technology supplier in the auto industry.[243] These timelines will kill any startup looking for revenue. Accordingly, we recommend that new battery startups look for initial niche applications that take advantage of unique performance capabilities of their technology. This will bring in revenue sooner and help prove out the technology. One good example of this strategy is the Canadian battery startup Corvus Energy. Corvus Energy focuses on large-format batteries for marine applications and has shown strong revenue growth over the past five years.[274] Another example lies in A123, which successfully commercialized new cathode materials for the power tool market within seven years of leaving the academic lab benchtop. A123 also proves an informative example in the converse case, as management decided to immediately move on to the automotive market without a middle-term market, and plunged into bankruptcy when demand for EVs slowed and their batteries were part of a recall.[275, 276] We believe attacking a beachhead market first and growing conservatively increases a startup's chances of building a profitable business.

A.6.2. Proposals for venture capital investors

We recommend that venture capitalists approach the battery industry with caution. We recommend developing scientific benches of industry and academic researchers, similar to pharmaceutical investors, to vet the science of prospective companies. Venture capital funds should also incorporate long time horizons into investment models to more realistically price battery startup companies. We believe interested investors will benefit from using common metrics to evaluate new battery companies. To provide a preliminary framework for evaluating early-stage battery companies, we propose the following benchmarks in Figure A.5. These metrics can help benchmark a new company's progress and valuation.

A.6.3. Proposals for component and cell assembly manufacturers

It is in large battery manufacturing companies' interest to foster a healthier startup ecosystem. This allows for more R&D ideas to be vetted and tested outside of corporate R&D. With that in mind, we recommend that large companies leverage joint development agreements and startup partnerships more widely. This allows large companies to gain a window into cutting-edge research with relatively low risk. It also helps build the pipeline for future performance improvements by tapping into startups' R&D potential; these performance improvements are critical in such a competitive industry. As seen in the pharmaceutical industry, transparency (e.g. via publishing trial data and setting endpoint requirements) can help the innovation ecosystem work more efficiently to both large and small companies' benefit. To help the startup ecosystem be more efficient and targeted toward manufacturers' R&D goals, battery manufacturers should widely release

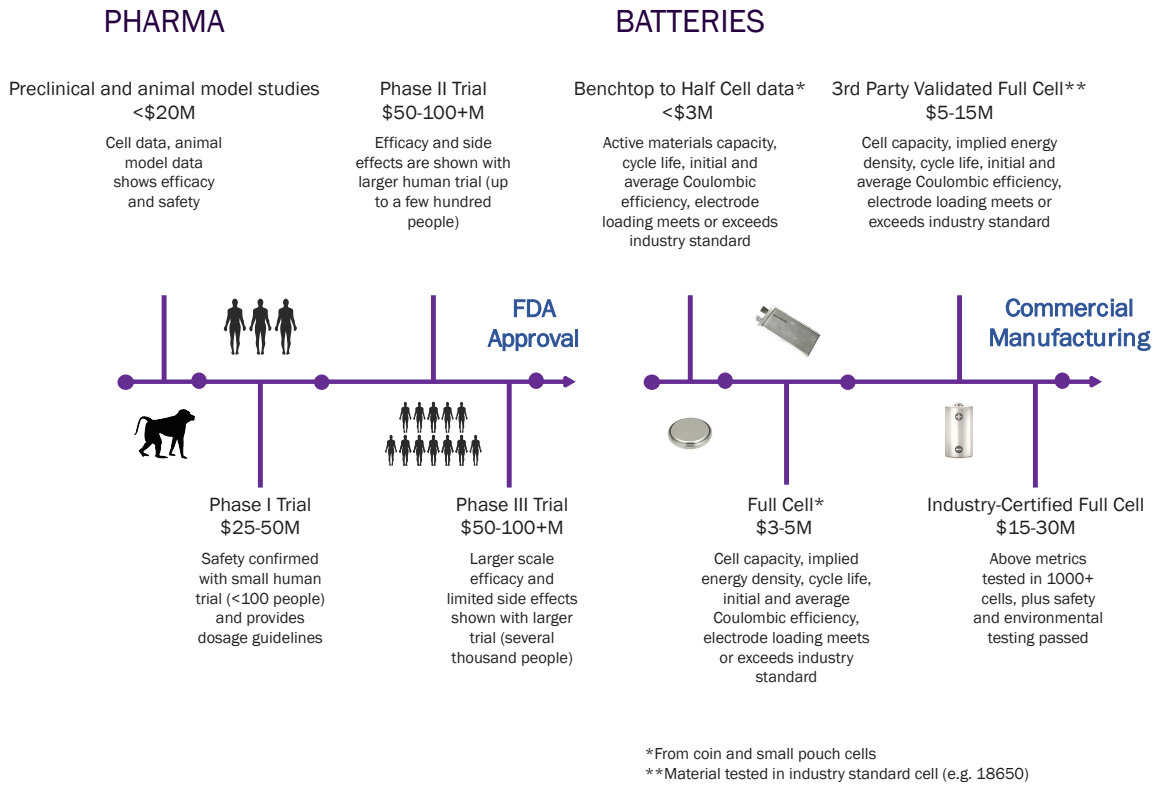

Figure A.5. Proposed battery technology phases and metrics for investor evaluation of startup company progress. Reproduced with permission from [230].

their key performance testing metrics. Battery companies should also present grand technical challenges for innovators, both in university and startup settings. Together, these initiatives would allow current academic and startup R&D efforts be more efficiently focused towards solving today's critical battery challenges.

A.6.4. Proposals for OEMs

Building off our proposals for battery manufacturers, we recommend that OEMs also support commercialization joint development agreements and partnerships. OEM products,

particularly battery-dependent products such as EVs, will be limited if battery innovation falters. However, battery innovation is not always a supply chain focus. Joint development agreements that bring together the innovative startup, battery manufacturer, and OEM will be most successful at commercializing new battery technologies to full market adoption. Policy makers can help foster these partnerships via consortia that bring together the relevant stakeholders, such as the U.S. Advanced Battery Consortium (USABC).

A.6.5. Proposals for policy makers

Given the social good brought about by improved battery performance but current market shortcomings, we believe the battery startup ecosystem is a prime target for intelligent government support. We have segmented out the potential policy support by battery startup development milestone.

A.6.5.1. Benchtop to half-cell stage. The government should build additional support for early-stage startup technical development due to the dearth of private investment. This could take place as financial support, perhaps via larger SBIR budgets with larger grants. It also could take the form of in-kind services, such as accelerator programs within national labs, to provide lab space, expertise and instruments to allow new companies to build their technical know-how. The DOE is currently piloting several programs of this kind, including Cyclotron Road and Chain Reaction Innovation.[277] We encourage these efforts.

A.6.5.2. Full cell stage. Downstream grants, such as applied research SBIR grants, would be most beneficial at this stage to accelerate market-targeted technical development. The new DOE Small Business Voucher Program is a good example of a policy initiative that can accelerate full cell battery testing and should be expanded. Additionally, prototyping centers across the country should be the target of new government funding mechanisms to support early stage technologies. Examples of such centers include the Battery Innovation Center in Indiana and Polaris Battery Labs in Oregon. Such targeted government support can accelerate startups' technical progress.

A.6.5.3. 3rd party validated full cell. The government currently certifies battery results, at institutions such as Crane or Argonne National Laboratory. Subsidized fees for startups and small companies would be an easy way for the government to help US startups achieve certified research results. Government battery testing helps startups certify their performance data, de-risking their technology.

A.6.5.4. Industry-certified full cell. By this point, government support could be limited. We recommend that government support be focused during early stages of development to help de-risk the technology. As the startup is de-risked, private and strategic dollars should be easier to attract. We hope that implementation of these ideas can aid startup success rates in the battery industry, resulting in more innovative technical development.

A.6.6. Potential pitfalls

While we believe these recommendations are sound, it is important to note the pitfalls of this analogical reasoning. The most important difference between the pharmaceutical

and the battery markets are the differences in margins for new products (~90% compared to $< 5\%$). Big pharmaceutical companies' continued success results in larger venture investment, more partnerships, and greater acquisition dollars for pharmaceutical startups as compared to battery startups. Pharmaceutical venture investment is currently 10x+ larger than energy materials/chemical/processes investment.

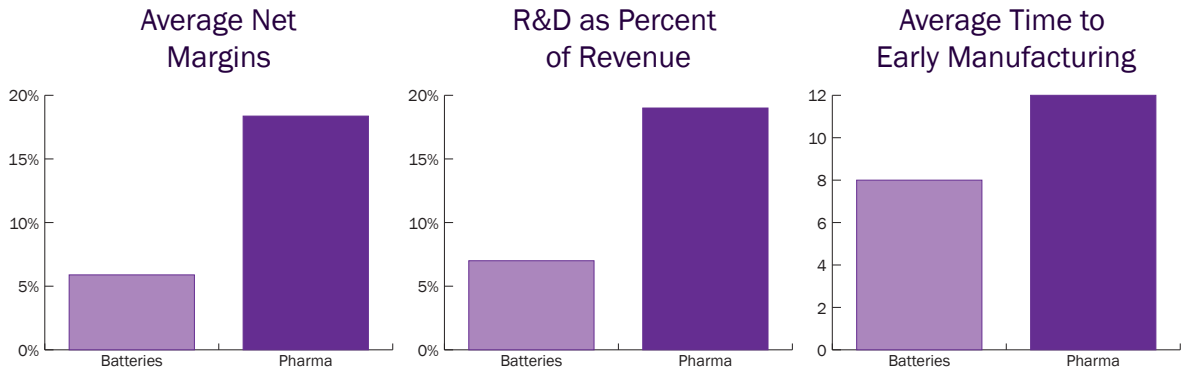

Figure A.6. F500 Pharmaceutical companies have significantly higher margins than F500 battery companies, which allows them to spend more on research and development. However, the scientific challenges of bringing a battery or a new drug to market, represented by time to manufacturing, are similar.[237, 248, 261, 278–283] Reproduced with permission from [230].

Figure A.6 shows the 2015 average operating margins, 2015 R&D as a percent of revenue, and average time to early manufacturing/commercialization (not profitability) between the battery and pharmaceutical markets. The pharmaceutical industry's high margins can lead to higher R&D budgets as a % of revenue and greater investment in the innovation ecosystem. However, the battery and pharmaceutical industry both experience long timelines to success driven by scientific challenges; it takes 12 years on average to move a new drug from discovery through final FDA approval and market launch.[283] The pharmaceutical industry also experiences high clinical trial failure rates (less than

1% of phase one candidates make it to market) with higher risk consequences (drug complications, death).[284] Based on our analysis, it takes battery startups an average of 8 years to achieve early commercialization/pilot manufacturing. Other sources have estimated the timeline of integrating a new material into the battery market as between 10-20 years.[241] The key challenge of the battery industry, especially as compared to the pharmaceutical industry, lies in overcoming the large scientific barriers with lower economic rewards for success.

A.6.7. Recommendations in practice: SiNode Systems case study

SiNode Systems is an early stage battery materials venture that recognizes the parallels between technology development in life and physical sciences. SiNode is commercializing a novel silicon anode technology based on research from Northwestern University, and the company has maintained a lean capital profile (raising only a seed financing round) since incorporating in 2013. SiNode has secured pilot customers in niche consumer electronics markets, and it has launched strategic partnerships with top-tier materials companies, battery manufacturers, and device OEMs. SiNode's partnerships with multiple OEMs (both in short-term niche markets and longer-term markets such as automotive) has accelerated commercialization of the company's anode technology. By working directly with OEMs, SiNode has gained leverage over its supply chain and formed partnerships with battery manufacturers recommended by the OEMs. The OEM relationships have opened the door to new sources of funding and supply chain partnerships that have significantly reduced SiNode's technical and scale-up risk. In addition, the company has received non-dilutive funding from the US Government's SBIR program and other public

sources, including the US Advanced Battery Consortium. The SiNode experience offers a case study in building value from strong technology partnerships, lean capitalization, and non-dilutive funding.

A.7. Conclusions

Higher energy density and lower cost lithium-ion batteries are critical to a carbon-neutral future. Yet there are daunting technical and market hurdles to bringing the advanced materials required for better battery performance to market. As a result, despite the US' world-leading academic battery research, most battery commercialization over the last 25 years has come from incremental advances implemented by large international battery companies. To address this US battery commercialization gap, we examine the status quo of battery commercialization. Interestingly, the pharmaceutical industry has many similar technical hurdles to the battery industry but has a robust startup innovation ecosystem. We take inspiration from the pharma model's successes to inform suggestions to improve the battery innovation ecosystem. We identify elements of the pharma model's success that apply to the battery industry and provide tailored proposals to entrepreneurs, investors, large battery companies, and policy makers. Together, we hope these ideas spur the battery ecosystem to more successfully commercialize transformative battery technologies.